Single-molecule Characterisation of DNA Hybridization via Fluorescence Microscopy and Optoplasmonic Sensing Approaches

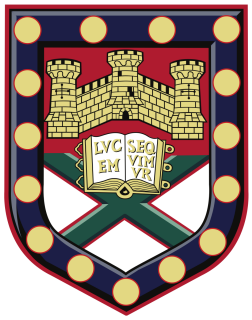

Submitted by Narima Eerqing to the **University of Exeter** as a thesis for the degree of Doctor of Philosophy, October 2022.

Acknowledgements

Looking back on the past four years, I feel incredibly lucky to have encountered many brilliant people, I appreciate all the support I received during this journey.

Firstly I would like to thank my first supervisor, Frank Vollmer, for all the kind support and countless insightful discussion. I still remember the first time I came to Exeter for the interview, he kindly offered me a lab tour and introduced everything with patience. By that time I was already deeply impressed by his enthusiasm towards science and positive attitude towards difficulties. Thanks a lot for providing an environment where I can freely explore my own ideas, and for the support in attending conferences/field-works. All these experiences have shaped me into a better researcher. A special thanks to Sivaraman Subramanian and Serge Vincent, for all the selfless help, from experimental training to Matlab program guidance, along with scientific writing and so much more. Both of them have shown me how to be a good experimental physicist. I thank all colleagues from our group: Hsin-Yu Wu, Simona Frustaci (of course Simone as well), Callum Jones, Aneeth Kakkanattu Arunkumar, Katya Zossimova, Rithvik Gutha, Gema Cabello, Deshui Yu, Monika Pietrzyk, Nikita Toropov, Samir Vartabi Kashanian, Keisuke Watanabe, Arturo Bianchetti, Mariana Serrano, Matias Rafti, Shahin Ghamari, Mattew Houghton, Kalani Perera, Alice Attenborough, Thomas Derrien, Sam, Srikanth Pedireddy. It is my pleasure to work with you all.

I would like to thank my second supervisor Janet Anders for her supervision and kind help with manuscript writing. I thank Jesus Rubio who showed me how to analyse data properly and taught me many writing and Matlab skills. I thank Ziqi Liu, Haitong Lin, Zheng Huang, Huanling Zou, Chengting Zhang, Qiuwu and Yizheng

Zhou, for their accompany and all the laughter we shared. I thank Viktoria Wedler, although the academic collaboration did not work well, the friendship did! I would also like to thank all fellows from CDT Metamaterials, especially Connor Sait, Euan Humphreys, Kavya Sadanandan, Cheng Shi, Konstantinos-Andreas Anastasiou, Karl Jonas Riisnaes, and Wai Jue Tan for all the unforgettable amazing times together. I am so fortunate to be part of this lovely community and I cherish all the happy memories we had.

Last but not least, I wish to thank my mom, Amei Wu, for always being there and encouraging me to explore my interest. I love you so much.

Abstract

The single-molecule study provides an unprecedented deep view into the biological process, unveiling the hidden heterogeneity that is hard to observe in ensemble methods. Recently, various techniques have shown the detection of biomolecules with single-molecule level sensitivity. However, each technique has its unique advantages and drawbacks. Single-molecule techniques can influence the molecular systems that they intend to detect in different ways. For example, fluorescence labels may affect the kinetics and dynamics of biomolecular interactions, while plasmonic-based approaches use local field enhancements that are not uniform across the involved plasmonic nanostructures, both of which can play a significant role in the observed statistics. Before one can combine the information obtained from fluorescence and optoplasmonic techniques, single-molecule experiments must be compared and cross-validated.

Here we first compare the detection of DNA hybridization on fluorescence-based imaging technique and optoplasmionic sensors. We investigate the impact of (i) the presence of labels, and (ii) the potential influence of the plasmonic nanoparticle surface. Our measurements reveal that the dissociation rates of hybridized DNA strands are approximately the same for both techniques. Our study establishes the equivalence of both techniques for this DNA molecular test system and can serve as the basis for combining these techniques in other single-molecule studies. With optoplasmonic sensing, our results indicate that one may benefit from the larger binding efficiency of fluorescence imaging while the impact of the label is checked with the optoplasmonic sensing platform.

To further combine the two single-molecule characterisation systems, we de-

veloped the first optical setup that integrates optoplasmonic and fluorescence-based detection. These sub-platforms provide complementary insights into single-molecule processes. We record the fluorescence and optoplasmonic sensor signals for individual, transient DNA hybridisation events. The hybridisation events are observed in the same sample cell and over a prolonged time (i.e. towards high binding site occupancies). A decrease in the association rate over the measurement duration is reported. Our dual optoplasmonic sensing and imaging platform offers insight into the observed phenomenon, revealing that irreversible hybridisation events accumulate over detected step signals in optoplasmonic sensing. Our results point to novel physicochemical mechanisms that result in the stabilisation of DNA hybridisation on optically-excited plasmonic nanoparticles.

Contents

List of Figures

List of Tables

Acronyms

WGM Whispering gallery mode

SPR Surface plasmon resonance

AFM Atomic force microscope

SMLM Single molecule localization microscopy

SERS Surface-enhanced Raman spectroscopy

DNA Deoxyribonucleic acid

PAINT Points accumulation for imaging in nanoscale topography

SIMOPS Single-molecule imaging microscopy and optoplasmonic sensing instrument

EM Electron microscope

TEM Transmission electron microscope

cryo-EM cryogenic electron microscopy

NMR Nuclear magnetic resonance

NSOM Near-field scanning microscopes

STED Stimulated emission-depletion microscopy

PSF Point spread function

PALM Photo-activated localization microscopy

STORM Stochastic optical reconstruction microscopy

TERS Tip-enhanced Raman spectroscopy

ATP Adenosine triphosphate

ADP Adenosine diphosphate

OT Optical tweezers

FRET Forster resonance energy transfer

TIR Total internal reflection

POI Point of interest

RU response units

ATR Attenuated total reflection

LSPR Localized surface plasmon resonance

Q Quality factor

F Finesse

GNRs Gold nanorods

FWHM Full-width-at-half-maximum

PDMS Polydimethylsiloxane

SDS Sodiumdodecylsulfate

TE Tris-EDTA

TCEP Tris(carboxyethyl)phosphine hydrochloride

HEPES 4-(2-hydroxyethyl)-1-piperazineethanesulfonic acid

Chapter 1

Introduction

1.1 Single molecule biophysics

The processes and components of life have been studied for decades. From a physicist's perspective, we can say that the processes involved are generally far from thermodynamic equilibrium. This makes it extremely hard to predict the behaviour of biomolecules since they live in a complicated and inhomogeneous microbiological system. Many ensemble average techniques in biophysics provide information on the mean average state of a biological system.

The environment could be significantly distinct even when a small volume of the biological component is considered. If one only uses bulk measurements to estimate an average state, a difference in the actual state of any individual molecule in the system is expected. On the other hand, single-molecule studies provide an unprecedently deep and accurate view of the biology and physics of life. One key feature of it is that it helps to review the multiple metastable free energy states of biomolecules, where these energy states are separated by levels of several thermal energy scale k_BT (k_B =Boltzmann constant, T = temperature). This is far beyond the detection limits of traditional bulk measurements [1, 2]. On the other hand, single-molecule techniques enable the observation of single molecular biological features of interest, and thus build up a library of molecular heterogeneity in the system. Ultimately, single-molecule studies not only offer an average value but also a distribution of probabilities[2, 3]. A distribution with separate clusters may

indicate the existence of discrete energetic or conformational states, and the location of the average compared to two distinct clusters might indicate a preference for one state over the other[4]. By analyzing the deviation from the mean average behaviour, along with some biological and physical background information, one can deduce the potential mechanism behind the behaviours.

Although single-molecule techniques have great advantages in acquiring information compared with ensemble techniques, there still are many challenges along the way. For instance, when we try to extract data from single-molecule experiments with high temporal or spatial resolution, the background noise must be minimized to ensure a signal-to-noise larger than 1[5]. In many cases Brownian fluctuations and thermal forces are the main sources of noise and variability for single-molecule experiments; it is always difficult to discriminate molecular heterogeneity from stochastic noise due to thermal forces. So, new single-molecule techniques which have higher collection efficiency and signal-to-noise are required to further investigate the nanoworld.

In the recent few decades, the rapid development of single-molecule approaches has stimulated the study of previously unsolved questions. The advances in experimental techniques can be analyzed into two main methods, wherein one involves direct visualisation of single molecules[6], and the other employs surface plasmon resonances and other techniques to conduct indirect sensing[7]. Here for the former techniques, the progress of super-resolution microscopy techniques is discussed. For the latter, label-free detection methods that address many longstanding questions in the life sciences are introduced. The features, limitations and applications of different approaches are listed, meanwhile, we discuss the exciting new directions in the future.

1.2 Energy, time, force and length scale of single molecules

Speaking of energy, time, force, and length scale, the environment a single molecule stays in is very different from the environment experienced by humans. For reference, some typical magnitudes of these quantities are shown in Figure 1.1 [2]. The

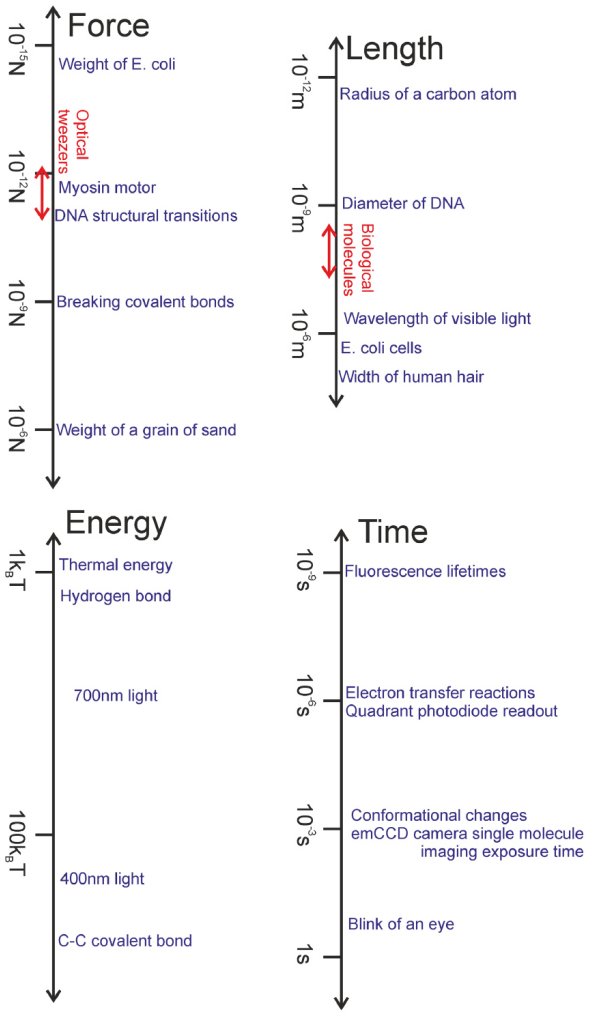

Figure 1.1: Magnitudes of typical lengths, times, forces and energies encountered in single-molecule biophysics. Image adapted with permission from [2].

.

length scale of biomolecules is usually smaller than the wavelength of visible light, and due to the existence of diffraction limits, it cannot be directly imaged using conventional light microscopy techniques[6]. The development of super-resolution fluorescence microscopes gives rise to precise localization with tens of nanometer accuracy. Meanwhile, atomic force microscopes (AFM) can achieve an atomic level of spatial accuracy[8]. The time scale of biological processes covers multiple orders of magnitude at least from the nanosecond fluorescence lifetime to years[2], covering the entire life of animals. However, the localisation of single-molecule super-resolution imaging is dependent on the collected photon number, therefore the time range of detection capability is then limited to the millisecond level[9]. Thus, it

can only image molecular conformation changes on the millisecond level at most. Biomolecular forces often lie in the pN range[3], and molecular displacements are normally on the order of nanometers. Thus, the energy scale is about 10^{-21} J to move a biomolecule 1 nm with a force of 1 pN. More specifically, the energy scale results from thermal fluctuations, which is k_BT, as biomolecules are immersed in the heat storage of water molecules. This energy level is generally the energy transferred in a thermal collision, which is approximately 4.1×10^{-21} J at room temperature, or equivalently 4.1 pN $\cdot$ nm[3]. The biological environment is aqueous, but for micron-sized objects (such as microbeads), the environmental Reynolds number is low. For particles in optical or magnetic traps and *in vivo* studies, the inertial force is much smaller than the viscous resistance. Under this condition, when the external force stops, the particles will stop moving[10]. The energy, length, time, and force experienced by biomolecules are very small, which indicates that trade-offs need to be made in the design of single-molecule experiments. For spatial localization, it may be necessary to sacrifice temporal resolution and vice versa, depending on the biological problem and the method used to solve it.

1.3 Scope of this thesis

This thesis focuses on techniques that characterise biomolecules down to the single-molecule level. With the rapid development in surface plasmon studies, enormous near-field enhancement induced by surface plasmon resonances has boosted the sensitivity of many characterisation tools. Among these, two have shown great potential in detecting single biomolecules. These are plasmonic-enhanced biosensors and single molecule localization microscopy (SMLM). Single-molecule detection with plasmonic enhancement has been studied in great detail. Nevertheless, few studies have compared the experimental results of both techniques for single-molecule studies. Here we address this concern in this thesis, with the outline as follows:

Chapter 2: In this introductory chapter we provide a brief overview of some of the most interesting approaches in single-molecule biophysics, with a focus on imaging techniques such as electron microscopes and fluorescence-based stochastic super-

resolution microscopy. On the other hand, surface-enhanced Raman spectroscopy (SERS) has proven its ability to detect a single-molecule deposited on colloidal metal or a substrate surface and offers high specificity. We briefly introduce this technique and share some exciting single-molecule experiments. Then we discuss some single-molecule manipulation tools that build up single-molecule force spectroscopy.

Chapter 3 lays out the schemes for DNA points accumulation for imaging in nanoscale topography (PAINT) single molecule localization microscopy. Recent advances in multiplexing and attempts to optimise acquisition speed are introduced. We also summarise the current limitation, the outlook and the future direction of this technique.

Chapter 4: In this technical chapter we explore surface plasmon resonance (SPR) enhanced biosensing in detail. We review traditional SPR sensing and single particle-based ensemble measurement. New developments in optoplasmonic sensing are introduced.

Chapter 5 shows the results for comparing transient DNA interactions using DNA-PAINT and optoplasmonic sensing. We report a comparison of two photonic techniques for single-molecule sensing: fluorescence nanoscopy and optoplasmonic sensing. Comparing the measured single-molecule kinetics helps to examine the influence of fluorescent labels as well as factors arising from different sensing geometries. Our results demonstrate that DNA dissociation is not significantly altered by the fluorescent label, while DNA association is affected by geometric factors in the two techniques.

Chapter 6: We investigate and reveal the cause of an unexpected DNA hybridization anomaly discovered using a state-of-the-art single-molecule sensing technique pioneered in our lab. Recently, a striking anomaly has been reported in single-molecule studies that use the most sensitive plasmonic nanoparticles to observe the DNA hybridization process. These single-molecule studies revealed an anomalous decrease in the DNA interaction kinetics when observed over a prolonged time. This observation is anomalous and unexpected as it was concealed in the previous bulk DNA experiments. The investigation of the anomaly in sufficient detail requires the applica-

tion of complementary single-molecule techniques, in addition to fluorescence-based methods, to obtain sufficient information about the anomaly. To do this we have built the first dual, single-molecule imaging microscopy and optoplasmonic sensing instrument (SIMOPS). Using the SIMOPS platform we observe DNA hybridization with two single-molecule techniques in parallel, and we found that permanent DNA hybridization events are the cause for the decrease in DNA interaction kinetics, and the stochastic permanent hybridization events accumulate over time.

Chapter 7 concludes the results of this thesis and summarises key aspects of the thesis, and an outlook for future work is provided.

Chapter 2

Characterisation of biomolecules beyond the diffraction limit

Probing light–matter interactions at the nanometer scale is one of the most fascinating topics of modern optics. Its significance is underlined by the large span of fields in which such accurate knowledge of light–matter interactions are needed, for example, nanophotonics, quantum electrodynamics, atomic physics, biosensing, quantum computing and many others. Increasing innovations in the field of microscopy in the last decade have pushed the ability to visualize across multiple length magnitudes, from micrometers to nanometers. One of the most straightforward approaches to studying a biological substance is by a light microscope. A light microscope uses visible light (wavelength approximately 400-700nm), which makes the technique minimally invasive to biological specimens and thus suitable for the observation of living organisms. However, it remains difficult to observe single molecules due to the fundamental diffraction limit caused by the wave nature of visible light. This limit was first described by Ernst Abbe in 1873[11]. He discovered a mathematical formula that describes the theoretical limits of resolution for a light microscope:

$$d = \frac{\lambda}{2NA} \tag{2.1}$$

that calculates the least distance to distinguish between two nearby objects. Here d refers to the minimum distance of objects that have to be separated in order to image

the specimen[12], λ is the wavelength of light and *NA* is the numerical aperture, that characterizes the range of angles over which the system can accept or emit light. In the case of visible light, the minimum distance required to distinguish close objects is around 250nm to 300nm. Normal biomolecules such as viruses (100 nm), proteins (10 nm) and less complex molecules (1 nm) are much smaller than this size and therefore unable to be observed by traditional optical microscopes[13]. Therefore new techniques are required to help with the understanding of the nanoworld.

Technologies that enable us to observe individual molecules in their natural state can potentially illuminate molecular interactions and complex dynamic behaviour. These techniques include optical microscopy methods[14], structural research tools[15] and label-free detection approaches[16, 17]. Since the 1950s, many experiments have made progress which contributes to performing single-molecule experiments on biologically relevant molecules in cells. The overall study contains experiments of non-biological specimens and cryogenic studies. Some historical studies that are particularly relevant to current research in the aspect of single-molecule biophysics of proteins and DNA are outlined below.

2.1 Electron microscope imaging of single molecules

By replacing the illumination source with a much shorter wavelength beam such as an electron beam, one can improve the imaging resolution according to equation (2.1). Imaging of a single biomolecule was achieved with the development of the electron microscope (EM). An image of the single filamentous molecule was taken by Hall[18] with a transmission electron microscope (TEM). In his work clear pictures of DNA were captured (see Figure 2.1a). Despite this, extensive destruction is always caused due to strong electron-organic interactions. Electron irradiation leads to the breaking of chemical bonds and the generation of free radicals, leading to secondary damage[21]. In general, small biomolecules are difficult to image directly under an electron microscope, because their constituent atoms are mainly composed of atoms with a low atomic number (such as carbon) and usually do not have a sufficiently high electron density to strongly scatter electrons[22]. To visualize

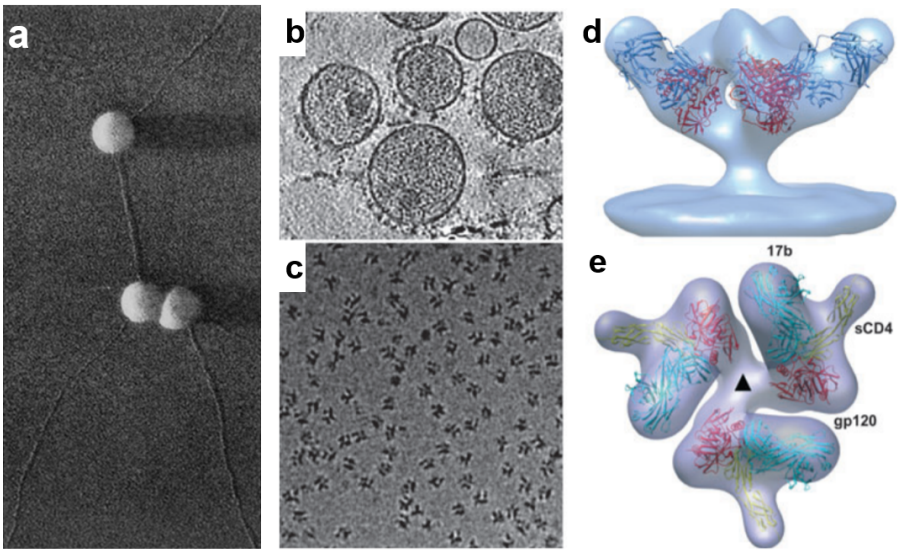

Figure 2.1: (a) DNA from calf thymus deposited from a water suspension. The admixed polystyrene spheres in this figure have an average diameter of 88nm. (b)Tomographic slice through a field of HIV virions recorded from a specimen grid that was plunge-frozen and stored at liquid nitrogen temperatures. (c) Density map at approximately 20Å resolution of the trimeric envelope glycoproteins complexed with the neutralizing antibody VRC01. (d) Projection image of individual molecular complexes of soluble trimeric envelope glycoproteins from HIV strain KNH1144. (e) Density map at approximately 20Å resolution of the complex of HIV envelope glycoproteins. Image adapted from [18, 19, 20].

.

biological samples, a process called shadow casting is often used, where a thin gold coating is deposited on the sample from an oblique angle. Uncoated areas in the shadows are easily visible in the EM image.

In EM, the sample is prepared on a mica substrate; this means that the image may not be a molecule in its original state because mica has a net positive charge on its surface, and many biological molecules, including DNA, also have a net charge. In addition, most biological samples are usually dissolved in water, and drying of the samples in EM since then has been shown to cause unnatural conformations. The common shadow casting or staining materials are normally composed of heavy metal or even radioactive nuclear materials. These unnatural conformations do not provide complicated structural or functional information[23]. Therefore, it is not preferred to directly utilise EM to image a single biomolecule.

The 2017 Chemistry Nobel prize was awarded to Jacques Dubochet, Joachim Frank and Richard Henderson for their pioneering work in the field of cryogenic electron

microscopy (cryo-EM)[24]. The breakthrough in cryo-EM has overcome the problem mentioned above and it is becoming a mainstream technology for studying the structure of cells, viruses, and protein assemblies with molecular resolution. The core of this technique is based on the principle of imaging radiation-sensitive specimens in a transmission electron microscope at low temperatures. The first step is to rapidly freeze (vitrifying) biological samples into glass-like ice, and then image at liquid nitrogen and/or helium temperatures[25]. Compared with ambient temperature, imaging at liquid nitrogen temperature can reduce radiation damage by up to six times. This means that for images recorded at low temperatures, higher electron doses can be used to increase the signal-to-noise ratio because the amount of radiation damage per unit electron dose is reduced. The approach used for obtaining 3D structures of macromolecules from electron microscopy components is tomography, where a series of images are collected, each image relative to the direction of the incident electron beam. These images can then be computationally combined to generate a ”tomogram”, essentially a 3D image of the specimen[26, 27].

Recent advances in microscope design and imaging hardware, as well as enhanced image processing and automation capabilities, are expected to further increase the effectiveness of the cryo-EM method[28]and nuclear magnetic resonance (NMR) spectroscopy has been routinely integrated with frozen EM density maps to achieve atomic resolution models of complex dynamic molecular components[29].

In biological research, cryo-EM shows a great capability to image individual bacteria, viruses and protein molecules in a relatively high resolution. By reconstructing the images, it has been successfully used in the analysis of biological structures in various environments. Nevertheless, this technique is only suitable to observe big molecules (normally larger than 100kDa) since the resolution is still not high enough to observe small single molecules[30]. In addition, samples must be frozen and stay inactive, which prohibits a direct observation of biological processes in their natural states[31]. For these reasons, cryo-EM remains very popular for structural assays and in material science. Meanwhile, light microscopes are still a firmly established tool for biology and especially for study of living cells.

2.2 Stochastic Super-resolution microscopy

In 2014, Eric Betzig, Stefan Hell, and William Moerner were awarded Nobel Prize in Chemistry for their key roles in establishing the field of super-resolution imaging[32, 33]. This type of technique shows a resolution within a hundred nanometers, and it has been the latest trend in high-resolution optical microscopy after about 300 years of history[34]. In less than 20 years, microscopy imaging in the field of life sciences has shifted from diffraction limits to resolutions in the tens of nanometers. The issue of imaging single molecules with electron microscopy has been discussed above, but for life sciences, detection in solid and aqueous natural environments is the key to imaging living cells because all proteins look almost the same electronically.

Light microscopy enables us to add unique markers to molecules of interest. Moerner was the first researcher to detect single molecules in the solid phase at low temperatures [35], while Orrit *etal*. used fluorescence to improve the signal-to-noise ratio of the measurement[36, 37]. Betzig is dedicated to the development of near-field scanning microscopes (NSOM) [38]and pioneered the implementation of super-resolution imaging in cells[39], and then realized single fluorescent molecules as a single layer at room temperature[40]. However, in a cell, fluorophores are too densely packed for single-molecule imaging. In 1994 and 1995, Hell and Betzig independently published the idea that what was needed was a method of "opening" one molecule at a time only at the diffraction limit point[41, 42, 43]. Hell proposed another method that operates by scanning the sample with an excitation pulse laser followed by a doughnut-shaped beam, which is named Stimulated emission-depletion microscopy (STED).[44]. The experimental procedure is as below: First, the excitation beam excites the fluorophores which are then stimulated by the STED beam to return to the ground state. As result, only the fluorophores located in the centre of the STED beam emit fluorescence. This effectively narrows the point spread function (PSF), thus increasing lateral resolution up to $\approx$ 20 nm[45, 46]. On the other hand, Betzig solved this problem by using a technique called Photo-activated localization microscopy (PALM)[42]. This technique employs a modified version of the photo-switchable fluorescent protein and activates only one of a random subset for each

imaging acquisition frame [47]. Well-isolated molecules can be located by fitting the fluorescence intensity centre with a PSF, and then effectively turning them off and exciting different subsets until a complete image is formed. Positions of all molecules in the sample can be recovered with precision which is only limited only by the number of collected photons. More photons mean more accurate localization and consequently higher resolution. Therefore, the resolution is no longer limited by diffraction. This very principle is the main idea of single-molecule localization microscopy (SMLM). Using the same principle, stochastic optical reconstruction microscopy (STORM) has changed photoswitchable fluorescent proteins to organic dyes[48]. DNA points accumulation for imaging in nanoscale topography (DNA-PAINT) technique offers an easy-to-implement approach owing to the use of DNA probes. Figure 2.2 shows super-resolved image examples of microtubules with PALM, STORM and DNA-PAINT respectively.

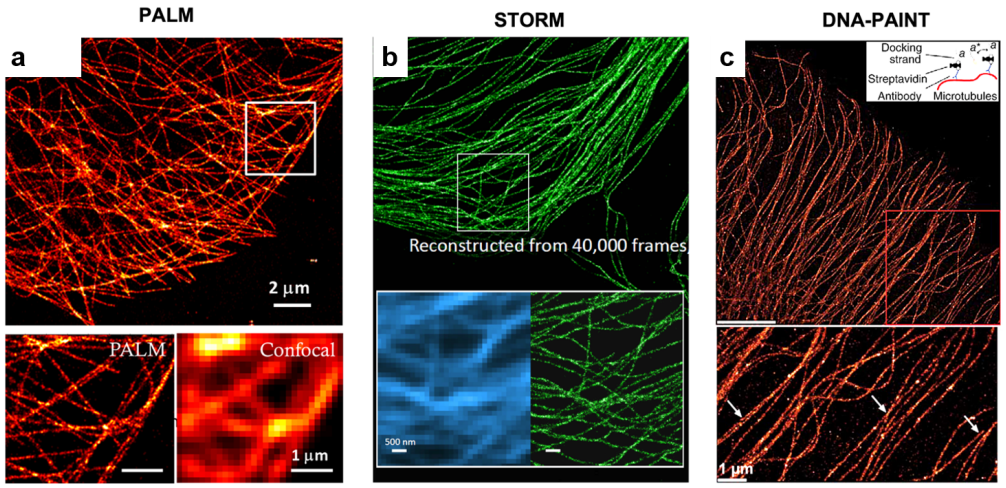

Figure 2.2: Super-resolution imaging of microtubules in cultured cells with PALM (a), STORM (b), and DNA-PAINT (c). Image adapted with permission from [49, 50].

.

2.3 Plasmonics enhanced Raman spectroscopy

Raman microscopy uses inelastic photon scattering to determine the chemical bonds existing in a molecule, so it can be used to identify specific types of molecules. Monochromatic photons undergo inelastic scattering through energy shifts in molecular energy states. Since photons are scattered rather than absorbed, displacement

can be seen over a wider range of input wavelengths, therefore infrared lasers are often used in this scenario[51]. The energy of the incident photon is usually decreased, which is the so-called Stokes shift; if the energy increases, then it is the anti-Stokes shift. Many incident photons are elastically scattered (Rayleigh scattering), so notch or edge filters are often required to implement this technique. The Stokes Peak is too small to detect a single molecule without enhancement[52]. There are many technologies for this purpose, such as surface-enhanced Raman scattering (SERS)[53], where the molecules of interest are adsorbed onto rough metal surfaces such as gold or silver, and tip-enhanced Raman spectroscopy (TERS) where the metal tip used in the atomic force microscope is placed above the sample[54]. Single-molecule detection by SERS at room temperature has been studied for at least 20 years[55], but research on biological samples is relatively new, large single mitochondria have been studied by TERS[56], along with detection of single dye-labelled Phospholipids in lipid membranes[57]. Various single molecule SERS (SM-SERS) techniques have been developed in recent years, examples can be found in Figure 2.3

Recently, Li-Jia *etal*. showed the detection of DNA with single-molecule sensitivity[62]. They addressed the irreproducibility of the SERS analysis problem that hampers reliable DNA detection, they were able to use iodide-modified Ag nanoparticles to obtain highly reproducible SERS signals of single- and double-strand DNA in aqueous solutions close to physiological conditions. Figure 2.3(i) and (j) show their SERS signals, clear identification of DNA with single-base sensitivity and the observation of a hybridization event has been demonstrated[63]. So far SERS has shown great potential in single-molecule analyses by providing intrinsic chemical information with high sensitivity.

2.4 Single molecule manipulation techniques

Force, torque, and conformational changes are the basis of most cellular processes: myosin resists actin to achieve muscle contraction; kinesin transport cellular cargo along microtubule orbits. In the process of DNA replication and transcription, the positive supercoil of DNA is formed due to the translocation of DNA or RNA

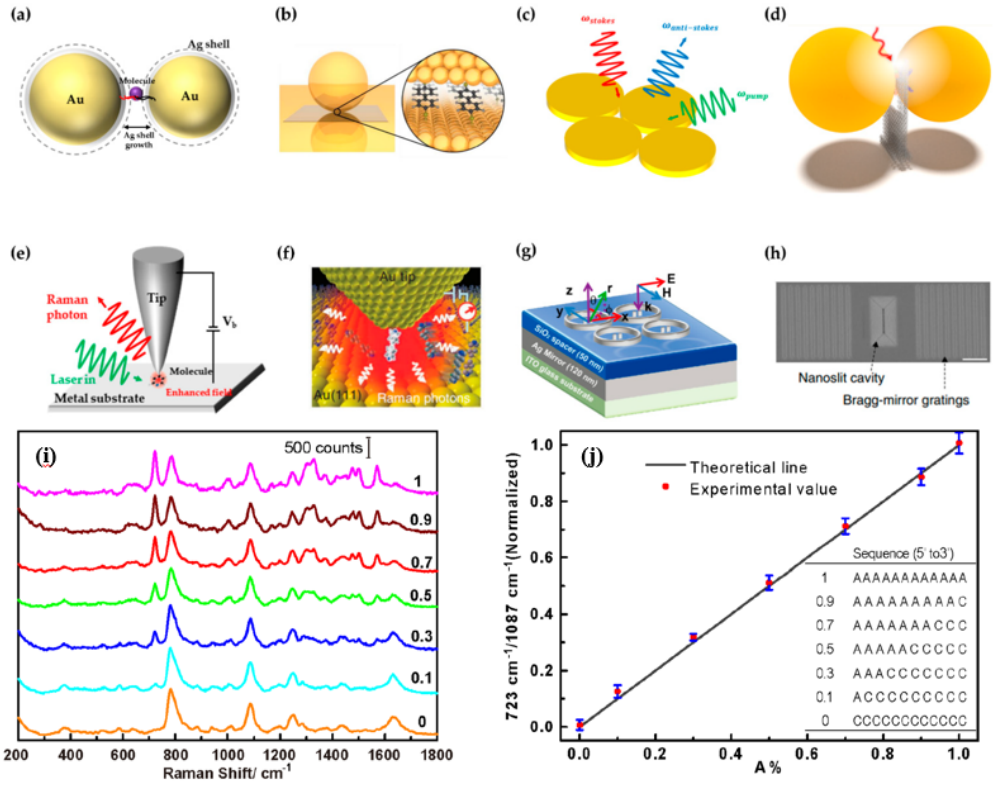

Figure 2.3: High-reproducibility substrates for SM-SERS. (a) Nanogap-engineered SERS-active gold–silver core–shell nanodumbbell. (b) NPoM configuration. (c) The enhancement map of the quadrumer substrate. (d) Nanoparticle dimer assembled on the DNA origami nanofork. (e) Tunnelling-controlled TERS. (f) Schematic diagram of FM-TERS. (g) Nanoantenna chip for SM-SERS. (h) The SEM image of the nanoslit device. Scale bar, 1 μm. Scanning electron microscopy, SEM. (i) SER spectra of a set of oligonucleotides composed of different numbers of adenine (A) and cytosine (C). (j) A plot of the relative peak intensity of 723 $cm^{-1}/1087cm^{-1}$ with the real ratio value of A in these oligonucleotides. Image adapted with permission from [58, 59, 60, 61].

.

polymerase, respectively[64]. It needs to be relaxed to a less stressed conformation by an enzyme called topoisomerase, and then continue replication/transcription; Adenosine triphosphate (ATP) synthase generates ATP from adenosine diphosphate (ADP) by rotating its gamma subunit[65]. Force manipulation techniques have been used to study such molecular machines, as well as a range of biological processes, including complex DNA topological manipulations, phase changes and even single-molecule DNA knotting[66, 66, 67]. Force spectroscopy tools, especially optical tweezers, magnetic tweezers, atomic force microscopes (AFM) and the new developing plasmonic techniques could measure forces and torques on individual

molecules[68, 69, 70, 71, 72, 73]. They can also apply biologically relevant values of force and/or torque to disturb innate systems. Among these, one of the most representative experiments is studying molecular motor dynamics.

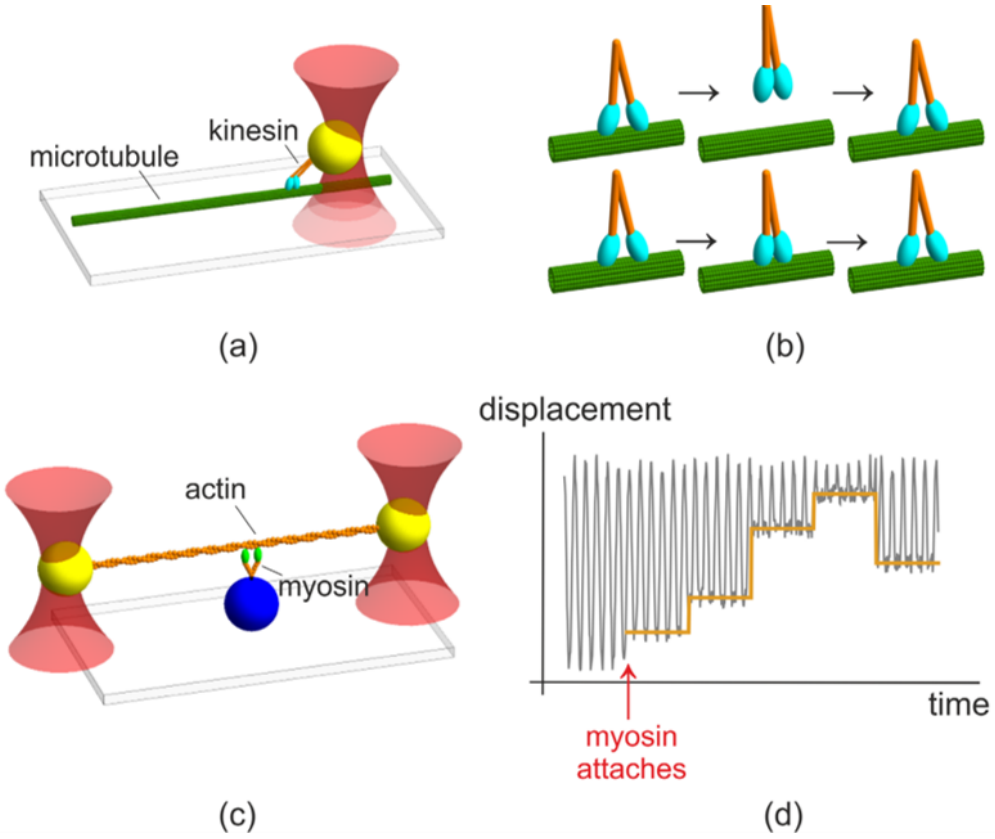

Figure 2.4: Schematics of a general assay for molecular motor type single-molecule force spectroscopy experiments and illustrations of results and conclusions. (a) Optical tweezers can position the kinesin-coated bead onto the microtubule. (b) General schematic showing two possible models of kinesin motion. Top panel: stroke-release model, in which the molecule briefly detaches from the fibre and diffuses back to carry on the movement; bottom panel: the hand-over-hand model where the molecule stays attached to the fibre for multiple cycles. (c) Dumbbell optical tweezers setup used to determine myosin-V stepping on actin. The blue bead is functionalised with myosin and is immobilised on the coverslip. While the myosin moves along the actin the optical traps can pick up the step size. The trap can also apply controlled forces to monitor myosin stepping behaviours at various force levels. (d) Schematic showing representative idealized displacement of the bead relative to the trap centre. Initially, the trap is set to oscillate triangularly. At the red arrow, myosin attaches to the actin and starts pulling, and the amplitude of the oscillation is reduced. This allows the determination of the myosin displacement along the actin (yellow trace). Image adapted with permission from [2, 74].

.

Block *etal*. [75] used optical tweezers (OT) to hold a kinesin-coated bead and position it onto a microtubule. OT use a focused laser beam to create a potential

energy well in the vicinity of refractile particles, such as a latex or glass bead of diameter around a micron, which results in an optical trapping force field of effective diameter close to the wavelength of the laser, due to combination of scattering and refraction effects from the laser on the particle. These result in a net force directed approximately towards the centre of the laser focus, the example can be found in Figure 2.4(a). This OT approach increases the effective experimental efficiency compared to waiting for kinesin to attach to the microtubule by diffusion alone since we can physically move a trapped bead coated in kinesin to its points of action at a microtubule. Once attached, the OT can cancel the Brownian motion of the bead in the surrounding aqueous media (a 'pH buffer' which can chemically stabilise the pH of the solution to within reasonably narrow limits) and apply a controllable manipulation of the bead's position to allow the force dependence of the bead motion to be interrogated. Figure 2.4a shows a general schematic diagram of an OT trapping a kinesin-coated bead, which translocates along a microtubule track. Two models are proposed for the movement: the stroke-release model (shortly detached) and the hand-over-hand (always attached) model, the difference being in the continuous or brief attachment to the microtubule (see Figure 2.4b for a general schematic of this). Block *etal*. determined that the latter model better explains the data from kinesin experiments. With 1 kinesin molecule per bead, the bead moves on average 1.4 μm before detachment takes place.

In a later paper, Svoboda and Block [76] used an improved OT with differential interference contrast optics and dual quadrant photodiodes (QPDs) to increase tracking precision to sub-nanometer levels. This precision facilitated measurement of the kinesin movement, indicating that its velocity decreases linearly with load up to forces of 5 to 6 pN. They also compared the force-velocity curves at high and low ATP concentrations to deduce that the movement per catalysed ATP decreases at a higher load. Myosins are a family of molecular motors that transport organelles along actin filaments, as well as being a vital component of muscle tissue. Biochemical studies suggested that myosin-V is a processive motor in the sense that it undergoes multiple catalytic cycles, or walks multiple steps, before detaching from the actin

(the alternative theory is that myosin walks one step before detachment). Mehta *etal*. [74] used optical tweezers to confirm the processive motor hypothesis and to determine that the step size is 36nm. Figure 2.4c shows a general schematic of a 'dumbbell' optical tweezers configuration used in the experiment. One trap is set to oscillate with a triangular displacement-time curve. When the myosin moves along the actin, it pulls the actin taught so the detected bead oscillation would have part of its oscillatory peaks removed. The lowered amplitude indicates the amount by which the myosin has moved. This method reveals step size, translocation speed and direction of motion of an individual myosin-V in real-time. The application of forces at physiological levels and simultaneous measurement of bead movement is currently possible with single-molecule force transduction devices, the most important of which are optical tweezers and magnetic tweezers. Most high-resolution optical tracking techniques use dual traps where instrumental drift is strongly suppressed for dumbbells suspended in water [77, 78, 79, 80].

Due to the diffraction limits and highly focused nature, OT can not be used to directly manipulate biomolecules. To apply forces to biomolecules without attaching microbeads, researchers have developed many plasmonic-enhanced single-molecule manipulation tools. The mechanism relies on the fact that the near-field electromagnetic field can be greatly enhanced at the tips of plasmonic nanoparticles. When the plasmon resonance condition is met, the plasmonic oscillation would induce a sharp decaying light field, and this high gradient will result in a strong force.

In 2011, Reuven Gordon's team demonstrated the capture of a single bovine serum albumin (BSA) protein molecule in a double nanohole structure[81]. They were able to observe the transition between the folding structures of two proteins, and different BSA folding configurations appear at different light transmission levels. Using the same technique, Gordon's team also showed that the double nanopore optical trap can distinguish between bound and unbound forms of a single protein Kinetic human serum albumin (HSA)[82]. Tsuboi's group reported permanent fixing and POT capture of λ-DNA molecules stained with YOYO-1 fluorescent dye using continuous wave and femtosecond lasers[83]. They employed the nanopyramid-shaped dimer

arrays on glass substrates that are fabricated using nanosphere lithography.

Plasmonic optical tweezers can overcome the diffraction limit of conventional optical tweezers and are able to capture nanoscale objects. They expand the capture and manipulation of nano-scale objects with nano-position accuracy, which also offers promising opportunities for applications in the fields of biology, chemistry, statistics, and atomic physics. Potential applications include direct molecular manipulation, lab-on-a-chip applications for viruses and nanoscale transportation.

However, the single-molecule manipulation tools mentioned above rely on the external force exerted on the biomolecules, which could drive the molecule out of its actual state *in vivo*, and, force-induced damage is expected. Therefore, fluorescence-based super-resolution microscopy is more desired to do less invasive characterisation.

Chapter 3

Single molecule imaging with DNA-PAINT

3.1 Introduction

For biomedical research, super-resolution microscopy is a promising tool that opened up a new perspective for the study and understanding of molecular mechanisms, with unprecedented resolution. The field of SMLM has been continuously improving, changing from an initial drive for pushing technological limitations to the acquisition of new knowledge. Among these, most implementations 'switch' molecules between fluorescence on- and off-states to obtain sub-diffraction image resolution. This switching is traditionally obtained in two ways as introduced previously: targeted switching actively confines the fluorescence excitation to an area smaller than the diffraction limit of light, for instance, in stimulated emission depletion (STED), [46], whereas stochastic switching uses photoswitchable proteins or photoswitchable organic dyes, i.e. PALM[84] and STORM [85]. Although these methods offer an outstanding spatial resolution, they are normally expensive and hard to implement. As a newborn member of the SMLM family, PAINT has shown an alternative approach of switching fluorescence on and off[86, 49]. Here, instead of labelling the target molecule with a fixed fluorophore, the target molecule of interest is either permanently or transiently bound to a free-diffusion dye or a dye-labelled ligand, which is the concept of universal PAINT (uPAINT)[87]. Figure 3.1a shows the

protocol of DNA-PAINT super-resolution imaging. Another labelling strategy is shown in Figure 3.1b. Figure 3.1c shows the comparison between a diffraction-limited image and a DNA-PAINT image.

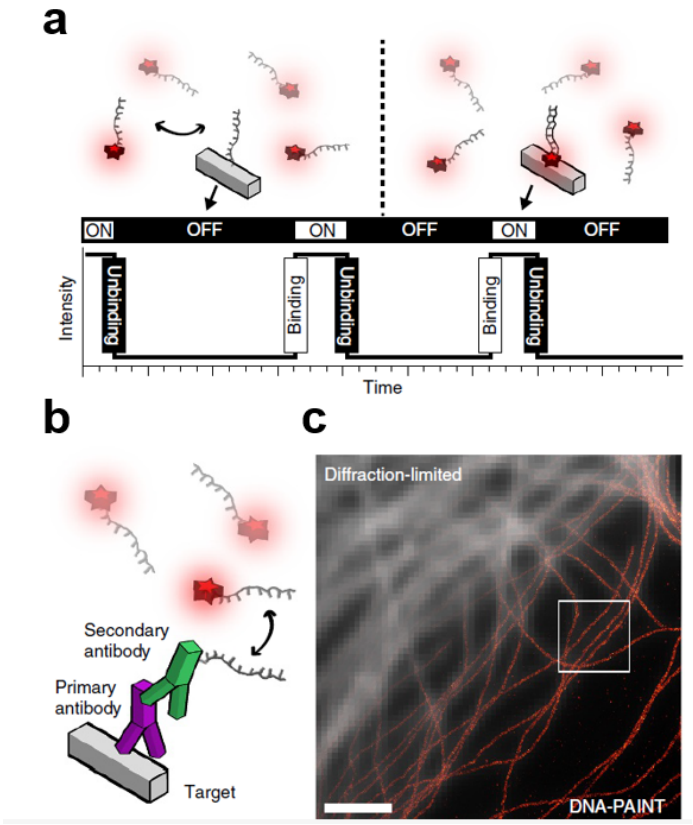

Figure 3.1: (a) DNA-PAINT concept. Transient binding of dye-labelled DNA strands (imagers) to their complementary target sequence (docking site) attached to a molecule of interest. The transient binding of imager strands is detected as 'blinking', illustrated by the intensity versus time trace. (b) In situ protein-labelling strategy for DNA-PAINT using primary and DNA-conjugated secondary antibodies. (c) Overlay of a diffraction-limited α-tubulin image (top left) with a super-resolved DNA-PAINT image (bottom right). Scale bar is 2 µm. Image adapted with permission from [49, 88].

.

PAINT can be implemented easily as long as the probes can diffuse and stay at the target molecule. Therefore optical switches can be obtained without complicated experimental conditions. However, the original implementation of PAINT made it difficult to specifically label more kinds of biomolecules, as interactions were mainly limited to hydrophobic interactions or electrostatic coupling, making programming difficult[89]. Meanwhile, DNA hybridization represents an approach that can take advantage of the PAINT concept and is therefore suitable for a pro-

grammable target-probe interaction system. In DNA-PAINT, the transient binding of short dye-modified (imager) oligonucleotides to their complementary target (docking) strands will produce the necessary ”blinking” to enable random super-resolution microscopy[90, 86, 49]. Due to the programmability and specificity of DNA molecules, they are employed as imaging and labelling probes, thereby alleviating the limitations of current super-resolution technology and making it compatible with many single-molecule dye[91, 92]. The latest development of DNA-PAINT has achieved infinite multiplexing on the spectrum, accurate molecular counting and ultra-high molecular-level (less than 5nm) spatial resolution, achieving positioning accuracy of about 1nm. By connecting the docking chain to the antibody, DNA-PAINT can be used in a variety of in vitro and cellular applications[49].

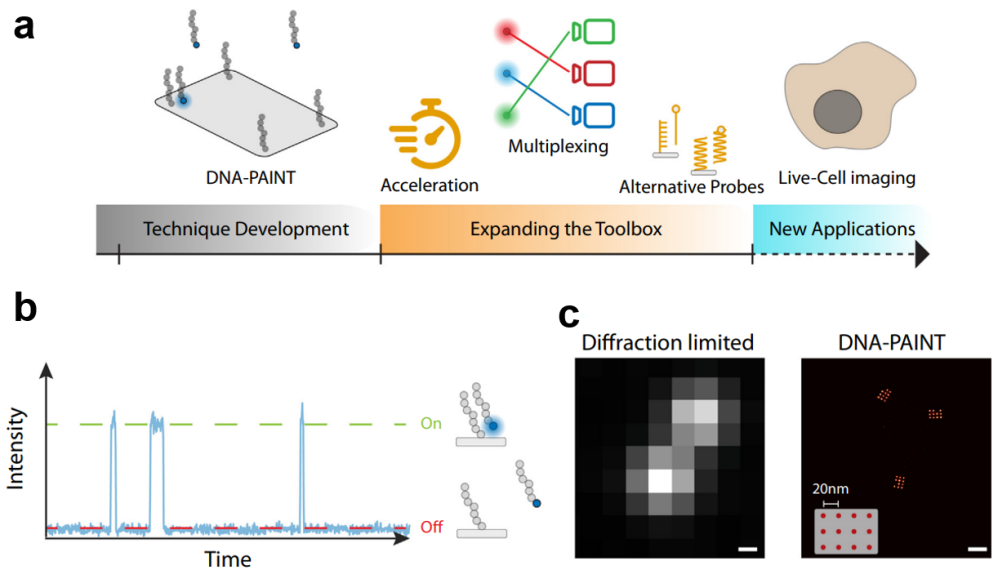

Figure 3.2: The concept of DNA-PAINT. (a) Timeline indicating the three main phases of the DNA-PAINT field: the development and improvement of the technique, recent advances that optimize and functionalize DNA-PAINT, and future progress for novel applications and live-cell imaging. (b) Transient binding of short dye-labelled DNA oligonucleotides (imager strands) to the complementary target sequence (docking strands) causes an increase in fluorescent signal (ON) and is detected as a localization event. (c) Computational simulation comparing diffraction-limited imaging (left) and DNA-PAINT super-resolved imaging (right) of DNA origami nanostructures. The DNA origami was designed to have 12 docking sites arranged in a 20 nm grid pattern (inset in the DNA-PAINT image). The simulation was performed with Picasso Software[86]. Scale bars are 100 nm. Image adapted with permission from [49, 93].

3.2 Recent advances in DNA-PAINT multiplexing

The properties of DNA-PAINT result in several improvements over more traditional super-resolution approaches. First, the use of DNA-based imaging probes enables high multiplexing by Exchange-PAINT [49] that is restricted only by the number of orthogonal DNA sequences, as compared with the spectrally distinct dyes used in classic multiplexing experiments. Specifically, after one DNA-PAINT image has been acquired, the buffer can be exchanged to introduce a different imager strand species. Repeated imaging, washing and reintroduction of new imager strand species then enable researchers to create a multiplexed image of many biological targets. Although they have thus far demonstrated nine-target super-resolution imaging, multiplexing could reach thousands of species, as the only limitation is the orthogonality of DNA-PAINT sequences.

Novel advances have focused on multiplexing which is the visualization of multiple distinct molecular species within a single sample [94, 49, 95, 96, 97]. The number of dimensions through which multiplexing is achieved has recently expanded to include sequence, kinetic, and spectral barcoding.

In sequence-based multiplexing, orthogonal sequences are employed to label distinct targets, and this strategy is the working principle of Exchange-PAINT[98]. With sequence multiplexing, the level of multiplexing is only limited by the number of orthogonal sequences that can be designed. However, because only a single type of fluorophore is used, and pseudocolours are assigned to each orthogonal DNA sequence, imaging must take place in sequential imaging cycles (Figure 3.3a). The acquisition time thus scales with the number of structures, making the imaging of a large number of structures in a single sample a long process. To reduce the time between sequential imaging cycles, the washing step can be eliminated by adding 'quencher' strands before each new imaging round. These quencher strands are complementary to the imager strands from the previous round, and, upon hybridization, the quencher strands prevent binding to the target and eliminate background fluorescence[97].

Efforts have been made to develop alternative multiplex approaches that can detect

multiple species in a single round of imaging. One such approach is kinetic fingerprinting, which can probe different species simultaneously. Multiplexing is achieved by varying both the binding time and binding frequency for different species (Figure 3.3b). Whereas the former is tuned by the number of base pairs that are formed between the docking and imager strand, the latter is modulated by the number of binding sites repeats on a docking strand. The two approaches can thus be varied combinatorially. The concept was demonstrated with fourfold multiplexing; however, to achieve higher levels of multiplexing, different dyes had to be integrated. This allowed 124-fold multiplexing on DNA origami constructs[96], but reaching this level of multiplexing requires up to 44 sequence repeats, and this might not be possible in more complex systems where the labelling efficiency is lower and the number of labelling sites is limited.

The third dimension of multiplexing exploits the spectral properties of dyes. Multiplexing by using different dyes is the most easily implemented approach (Figure 3.3c, top panel), but it is inherently limited by the number of distinguishable dyes. To minimize colour crosstalk, the dyes are typically excited sequentially at different wavelengths. The number of excitation lasers required for spectral multiplexing was recently reduced by frequency modulation, allowing the detection of five different dyes[99].

To circumvent this constraint and still allow spectral multiplexing, Förster resonance energy transfer (FRET) between a donor and a receptor fluorophore has been used in correlative FRET multiplexing. By varying the position of the donor fluorophore on the imager strand, the separation between the dye pair will alter, and different FRET efficiencies (E) will be obtained (Figure 3.3c, bottom panel). However, since FRET efficiency is bounded between 0 and 1, so far only 3-FRET efficiencies could be distinguished[95, 96]. The kinetic and spectral multiplexing strategies have enabled the detection of several targets of interest in a single imaging round, thereby increasing the imaging speed compared to conventional Exchange-PAINT. For these approaches, however, the overall low binding frequency is still an intrinsic limitation.

3.3 Optimising the DNA-PAINT acquisition speed

A long acquisition time, rooted in the requirement to collect many photons to pinpoint the centre location of a fluorophore, is a fundamental limitation of all SMLM techniques[100, 101]. Because distinct targets within a diffraction-limited region should not blink simultaneously to be resolvable, each individual docking position is unoccupied most of the time, causing an acquisition time of up to several hours[102]. The acquisition time of DNA-PAINT is affected by the number of required localizations, the number of docking positions within a diffraction-limited area, and the binding frequency.

DNA-PAINT uses imager strands $\sim$ 8 mer in length which have an association rate of $\sim 2 \times 10^6 M^{-1} s^{-1}$ under standard DNA-PAINT experimental conditions[102], but this parameter has a wide range depending on buffer composition, strand length, and sequence. The freely diffusing imager strands contribute to background intensity, thus their concentration (c) is limited by the minimal required SNR and their concentration typically varies between 0.5 and 10 nM[90]. Recent advances have focused on accelerating image acquisition by increasing the binding frequency (f_b) of a target molecule either by enhancing the permissive strand concentration or by increasing the association rate of individual imager strands (f_b = concentration $\times k_{on}$).

3.4 Limitations of the DNA-PAINT technique

Although DNA-PAINT offers several advantages over traditional super-resolution techniques, as discussed above, we also note that there are some limitations. One drawback is the fact that 'imager' strands are non-fluorogenic, with the following two implications: first, DNA-PAINT is limited to optical sectioning techniques such as total internal reflection (TIR), oblique[103] or light-sheet[104] illumination due to the elevated background fluorescence originating from unbound imager strands. Second, the freely diffusing nature of imager strands furthermore sets an upper limit to the achievable acquisition speed compared with those of STED, PALM, and STORM. Furthermore, DNA-PAINT applications are currently limited to selected specimens. It is difficult to do Live-cell imaging because of the complexity of

infusing dye-modified DNA single strands into living cells and the unforeseen results of introducing them.

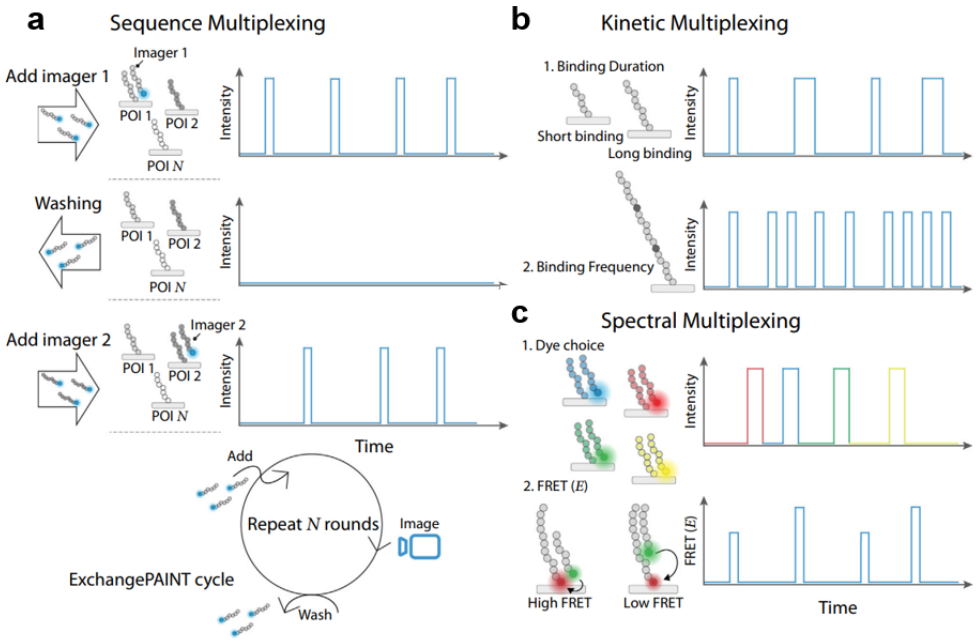

Figure 3.3: Multiplexing with DNA-PAINT. (a) In sequence-based multiplexing, each point of interest (POI) in a target sample is labelled with a unique docking sequence (1, 2, . . . , N). After obtaining sufficient localizations, the imager strand for POI 1 is washed away and the next imager strand can be introduced. (b) Kinetic multiplexing can achieve its discernibility by varying the length of the hybridized duplex and the subsequent difference in the dissociation rates and thereby binding times of the imager strands (top). (c) Spectral multiplexing requires either orthogonal imager strands that are each labelled with a unique fluorophore to probe various targets in parallel (top) or a varying distance between a donor and acceptor Förster resonance energy transfer (FRET) pair that results in a different FRET efficiency (bottom). Image adapted with permission from [49, 93].

.

Chapter 4

Surface plasmon resonance enhanced biosensing

The detection of single-molecules has relied on fluorescent labelling with high quantum-yield fluorophores. Recently, near-field optical engineering with plasmon nanostructures has proven to be a promising way to boost weak signals from molecules with low quantum yields. Plasmon-enhanced detection enables direct optical detection of weakly emitting and completely nonfluorescent species, it is a research area that studies the interaction between electromagnetic waves and metal nanostructures[105]. In metal nanostructures that exhibit plasmon resonance, the resonance frequency depends on the restoring force, the effective electron mass, and the dielectric constant of the metal. Nanoplasmonics provides light confinement well below the optical wavelength since there are optical modes for positioning based on dimensions much smaller than the optical wavelength. These modes are called surface plasmons, and they are the intrinsic modes of collective electron oscillation. The surface plasmon resonance (SPR) on these nanostructures is a condition for the electromagnetic coupling of the electromagnetic waves with the free electron motion of the nanostructures. The electric field associated with the SPR rapidly decays into the surrounding medium and acts as a transducer that converts local refractive index changes into SPR frequency shifts. These shifts can be easily monitored in the optical far field without the need for near-field optics or electrical contacts[106].

4.1 General principle of SPR sensing

Figure 4.1a shows the mechanism for SPR sensors. In SPR biosensors, probe molecules are firstly immobilized on the sensor surface. When the solution of target molecules is added into contact with the surface, a specific binding between probe-target occurs, which consequently induces an increase in the refractive index at the SPR sensor surface (Figure 4.1c, d). In SPR experiments, resonance or response units (RU) are used to describe the signal change, where 1 RU is equivalent to a critical angle shift of 10^{-4} degree. At the start of the experiment when probe-target interactions have not yet occurred, the initial RU value corresponds to the starting critical angle. The change in refractive index Δn_d arising within a layer of thickness h can be calculated as:

$$\Delta n_d = (\frac{dn}{dc})_{vol} \cdot \frac{\Delta\Gamma}{h} \tag{4.1}$$

where $(dn/dc)_{vol}$ is the increase of refractive index n with the volume concentration of analyte c, and $\Delta\Gamma$ is the concentration of the bound target on the surface[107]. The refractive index change is tracked by the coupling of incident light into a propagating surface plasmon (PSP) on a gold surface in real-time. Accordingly, the rate of association (k_{on}) during the association phase, the rate of disassociation (k_{off}) when target molecules are removed by washing with buffer, and the association rate constant (k_a) and dissociation rate constant (k_d) can be determined by SPR evaluation of binding kinetics. The parameter related to the refractive index can also be used to detect and quantify the target molecules bound to a known probe immobilized on the sensor surface. The limit of detection (LOD) in the SPR experiment depends on several factors including the molecular weight, optical properties and binding affinity of target-probe molecules as well as the surface coverage of the probe molecule.

For the commercial SPR biosensor configuration, the incident light is applied using a high-refractive-index glass prism in the Kretschmann geometry, (See Figure 4.1). The SPR angle, which is the angle of minimum reflectivity, can be determined by varying the incidence angle and recording the reflected light intensity during the biological binding reactions. It is dependent on the refractive index of the

material near the metal surface. As a result, when there is a small change in the refractive index of the sensing regime through biomolecule attachment, detection is thus achieved by measuring the frequency changes in the reflected light obtained from the photo-detector. In addition, the concentration of target molecules can be quantified by monitoring the reflected light intensity or tracking the resonance angle shifts. Generally, the SPR biosensors have a detection limit on the order of 10 pg/mL, which is around 100kDa per mL. However, biomolecules like single DNA are much smaller than that, for example, 270 base pair DNA is around 10kDa. Hence, small single molecules are far beyond the SPR detection range. To address this issue, new techniques are required to boost the sensor sensitivity.

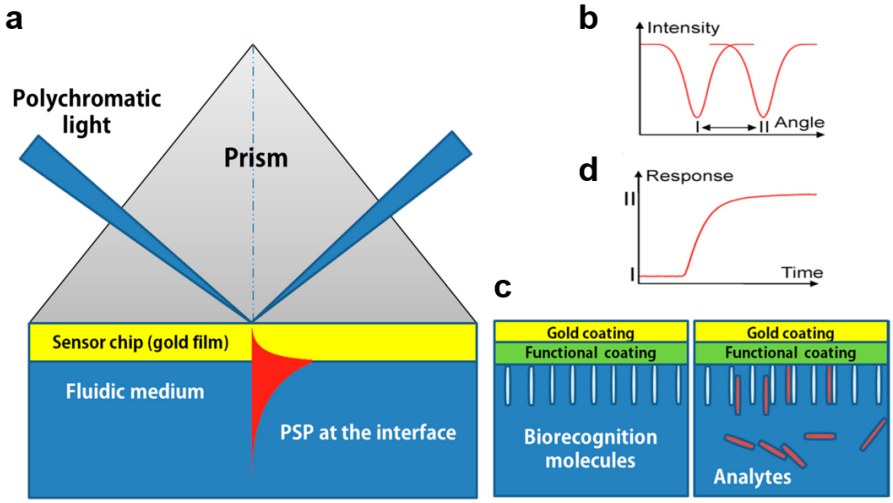

Figure 4.1: Concept of a surface plasmon resonance (SPR) biosensor: (a) Kretschmann geometry of the ATR method; (b) spectrum of reflected light before and after refractive index change; (c) analyte-biorecognition elements binding on SPR sensor surface and (d) refractive index changes caused by the molecular interactions in the reaction medium. Image adapted with permission from [108, 109].

.

4.2 Localized surface plasmon resonance based sensor

A logical approach to overcome these limitations mentioned above is the use of plasmonic nanoparticles, which exhibit a strongly reduced surface area compared to a metallic film.

Plasmonic nanoparticles exhibit localized plasmon resonances due to the collective oscillation modes of the conduction electrons in the particle, which have to meet boundary conditions at the particle's surface. The frequency of the plasmon resonance then depends on the shape, size, material, and environment of the particle. Localized plasmons in gold and silver particles occur at visible-NIR wavelengths (400-1000 nm) and are therefore compatible with standard optical microscopes (see Figure 4.2a). Readout with far-field optics enables low invasive sensing, which is particularly favourable in biological media like cells. The ability to detect and study

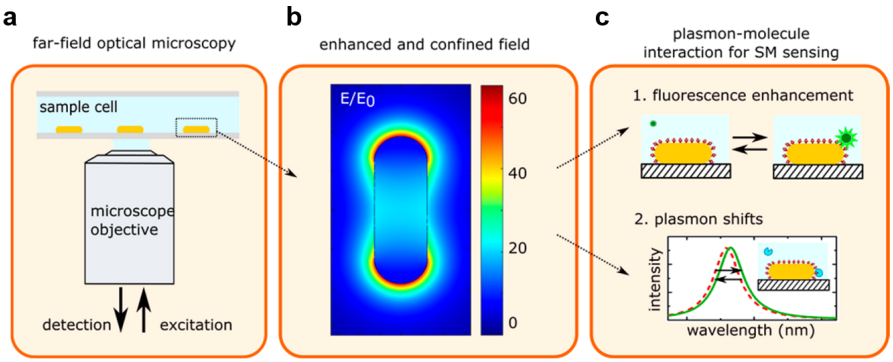

Figure 4.2: Principle of plasmon-enhanced single-molecule sensing using nanoparticles. (a) The sensor is typically probed in a far-field optical microscope, where single particles are interrogated. (b) The plasmon resonance induces a strongly enhanced and tightly confined local field around the particles. The field shown here is for a gold nanorod that is excited on resonance (calculated using the boundary element method). (c) This local field mediates plasmon-molecule interactions, enabling enhanced single-molecule detection by monitoring plasmon-induced changes of the molecule (resulting in, e.g., fluorescence enhancement) or by monitoring molecule-induced changes of the plasmon (resulting in frequency-shifts of the plasmon). Image adapted with permission from[110].

.

biomolecules using particle plasmons is accelerated by the electric field associated with the plasmon resonance (Figure 4.2b). This field penetrates the medium around the particle and enhances the interaction between a molecule and the particle's plasmon. This plasmon-molecule interaction provides two sensing mechanisms (Figure 4.2c): First, by utilising the plasmonic enhancement of the molecule's fluorescence; Secondly by exploiting the effect of the plasmon resonance's frequency shifts.

4.2.1 Single molecule sensing by plasmon shifts

The first reports on label-free plasmon sensing using single metallic particles originates from the early 2000s. Single gold and silver particles were used to detect the adsorption kinetics of thiols to bare particles[111] and the interactions between avidin and a biotin-functionalized particle[112]. Time-dependent measurements of the plasmon spectrum of the individual particles revealed the kinetics of binding. The particles employed were normally spherical with diameters of 40 nm or more to enable detection in a dark-field microscope. It was later that researchers started to realize, other structures such as nanoshells[113], triangular particles[114], nanorods[115] and nanocubes[116], exhibit higher sensitivities to molecular binding than spherical particles. Of these shapes, gold nanorods are now mostly employed as plasmon sensors[117, 118] due to their ease of synthesis, single-crystalline nature, and narrow plasmon resonance. Nusz *etal*.[119] employed individual gold nanorods to monitor streptavidin binding to biotin-functionalized particles. They recorded single-particle scattering spectra with a dark-field microscope and detected plasmon shifts, concentration-dependent shifts of several nanometers were discovered. Sub-second time resolution kinetics can be monitored by recording spectra over time. Multiplexed detection with single gold nanorods was demonstrated by Rosman *etal*. [120]. They employed aptamer functionalized particles that were added into a flow cell leading to deposition in the sample chamber. By imaging the location of deposition in an optical microscope, they obtained a map of particle locations. This process was repeated for four different populations of nanorods, each functionalized with an aptamer against a different target. This allowed them to perform multiplexed detection of four different analytes: fibronectin, streptavidin, IgE, and thrombin[121].

Sensing with a single particle shows superior sensitivity over ensembles of particles since inhomogeneous broadening of the plasmon resonance is eliminated. However, it is still considered as an ensemble measurement, because essentially it is averaging the binding of many molecules to a single nanoparticle, and transducing it into an optical signal. As stated before, molecular bulk measurements are not capable of

resolving events such as the binding of rare molecular species or anomalous binding behaviours, which would get averaged out in bulk measurements[122]. To resolve these hidden heterogeneities among molecular populations, and to examine stochastic processes governing molecular interactions, label-free sensing with sensitivity down to the single-molecule level is essential.

4.2.2 Theory and experiments utilising plasmon resonance shift

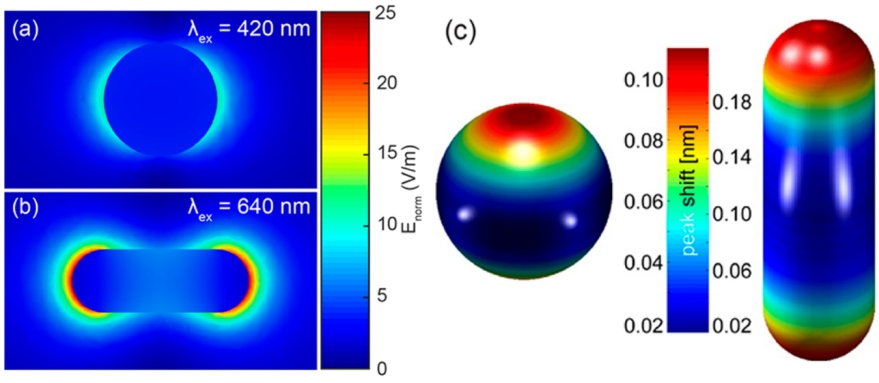

Figure 4.3: Local electric field intensity around a silver sphere (a) and a silver nanorod (b) immersed in water, simulated using the boundary element method. (c) Position-dependent plasmon peak shifts for a dielectric nanosphere (radius 3 nm) binding to the surface of the particle in water. Image adapted with permission from[110].

.

It would be informative to estimate the plasmon shift induced by the binding of an individual molecule. Previously, the sensitivity of a plasmon sensor was expressed by $d\lambda/dn$ which describes the shift of the resonance per refractive index unit[123]. Though it is appropriate for bulk index sensing, for events with single-molecule sensitivity it is far more complicated. The plasmon shift caused by the binding of a single molecule is proportional to the local field intensity integrated over the volume of the molecule[124, 125]. The local field around a metallic particle is generally greatly enhanced around tips and humps. It decays away from the particle surface rapidly (see simulations in Figure 4.3a). It means that the resulting plasmon shift is a function of the particle and the molecule size, the position of the molecule, and the distance between the molecule and the nanoparticle surface.

Theoretical estimations of the plasmon shift have been acquired using the electrostatic

approximation[124], perturbation theory[125], and numerical simulations[124, 126]. Davis *etal*. modelled the shifts for gold nanorods employing electrostatic coupling theory, modelling the molecule as a dipole contained within a dielectric sphere[127]. In close proximity, the polarizable dielectric screens part of the charge on the nanoparticle leads to a red-shift of the plasmon[127]. When the molecule arrived on the nanorod surface with the maximum electric field strength, the largest plasmon shifts occurred. Antosiewicz and Kall [128] used numerical models to estimate the plasmon shift induced by the binding of a 3-nm-radius dielectric sphere to silver nanoparticles of different dimensions. They reported plasmon shifts that strongly varied with both nanoparticle geometry and binding position, as depicted in Figure 4.4. Typical plasmon shifts induced by single proteins are smaller than 0.5 nm ($\approx 1\%$ of the line width), and therefore require sensitive optical microscopy to be detectable. Experimentally, Mayer *etal*.[130] demonstrated label-free detection of the unbinding of single IgG antibodies from gold bipyramids in 2010. Nevertheless, the noise of measurement required averaging over tens of events to reveal one detectable binding signal. In 2012, discrete molecular binding and unbinding of single proteins without statistical averaging was demonstrated by Zijlstra *etal*. [129]. They reported that the photothermal signal scales with the volume of the particle, therefore enabling the detection of smaller particles with a high signal-to-noise ratio. When protein is attached, by tracking the plasmon peak wavelength, red shifts yield discrete changes in the absorption cross section at the photothermal probe wavelength (see Figure 4.4). With knowledge of the nanorod's plasmon line width, peak shifts could be deduced from detected discrete changes in nanorod absorption at the pump wavelength. Wavelength shifts of 0.5 nm for streptavidin (53 kDa), 1.2 nm for antibiotin (150 kDa), and 1.6 nm for streptavidin-RPE (300 kDa) were observed. Interestingly, the plasmon shifts did not scale linearly with molecular weight, the authors attributed this to a reduced overlap between the molecule and nearfields for larger molecules.

4.2.3 Challenges along the way

Despite the rapid progress in the last decade, several challenges remain and prohibit plasmon-enhanced sensing from being incorporated into real-life applications. Here

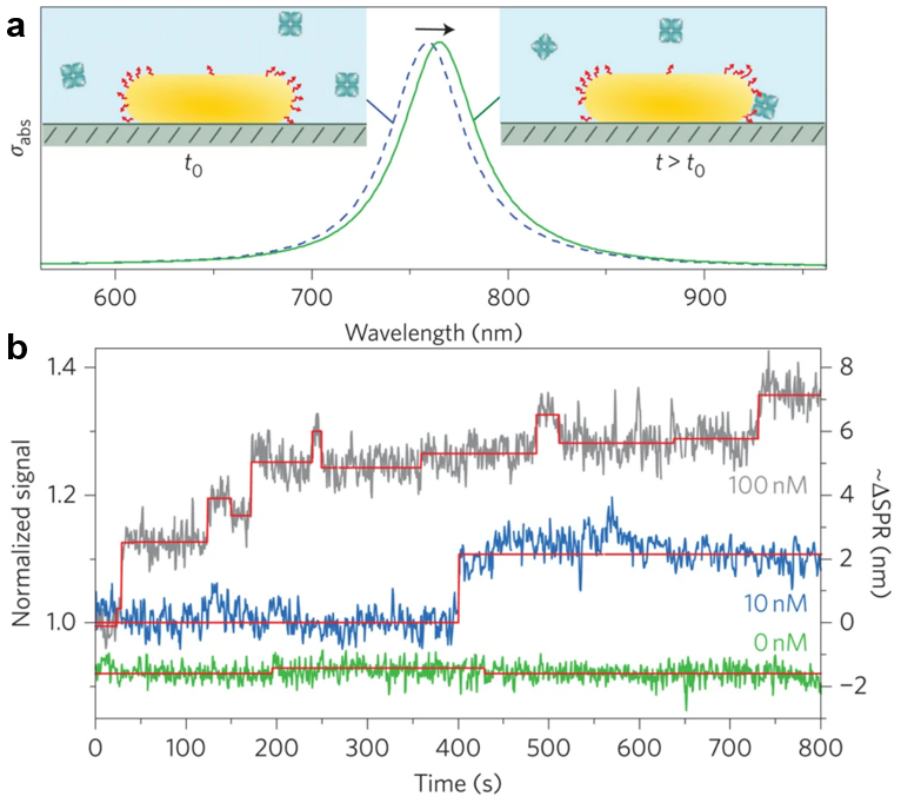

Figure 4.4: Principle of the method. (a) A single gold nanorod functionalized with biotin is introduced into an environment with the protein of interest. Binding of the analyte molecules to the receptors induces a redshift of the longitudinal SPR (exaggerated in the illustration). This shift is monitored at a single frequency using photothermal microscopy. (b) The normalized photothermal signal as a function of time for biotin-functionalized gold nanorods in the presence of a streptavidin–R-phycoerythrin conjugate. The photothermal signal was recorded on three different nanorods in the presence of different concentrations of the protein. Image adapted with permission from[129].

.

we discuss two of those challenges:

Statistics and waiting time

The main reason for developing single-molecule sensors lies in the ability to reveal populations of molecular interaction parameters and identify rare species in a sample volume. The reliability with which these properties can be assessed is determined by the amount of gathered statistics in a reasonable time. Single-molecule waiting-time distributions show Poisson statistics, and the error in determining the mean of distribution thus scales as $1/\sqrt{N}$ (N is the number of detected events.), which implies the ability to distinguish separate populations relies on the amount of statistics gath-

ered. For the single and very small sensors described here, the number of molecular interactions detected per unit of time depends on the sensor size and the diffusion coefficient of the analytes[128]. For analytes present at high concentrations (>nM), the frequency of detection is typically more than several Hz for a hemispherical sensor with a radius of 50 nm[131]. This means that a distribution can generally be clearly resolved within minutes. However, with low concentrations such as at 1 fM, it takes nearly a day for the first molecule to diffuse to the single-particle sensor[131]. In a single-molecule sensor, these transportation limitations lead to a long waiting time between events and therefore a slow response and limited accuracy in determining concentrations and populations are expected.

Low signals from small molecules

Although sensing by plasmon-enhanced fluorescence enables the detection of small molecules, labelling is not always practical. In the meantime, a drawback of the label-free techniques discussed above is that they depend on subtle changes in the local refractive index induced by molecular binding. These refractive index changes lead to a plasmon shift which can currently be detected with a sensitivity of $\approx 0.5nm$ (equivalent to $\approx 1\%$ of the line width) on a single nanoparticle.

Nevertheless, simply applying LSPR sensing with single nanoparticles, it is hard to detect single-molecule activities, the reported smallest single molecule detected with single nanoparticles is streptavidin[129]. The size of a single streptavidin is around 53kDa, while biomolecules like DNA oligonucleotides are much smaller than that (27 base pair $\approx$ 10kDa), therefore fluorescence based imaging is still needed in single-molecule detection. However, one could use nanoantennas or nanostructures to get an improved LSPR and fluorescence signal. Anastasiya *etal*. have reported single-molecule detection applying DNA Origami Nanoantennas[132], with a fluorescence concentration at 25uM. To realise label-free single molecule detection, new techniques that display high sensitivity along with a high signal-to-noise ratio are thus required.

4.3 Whispering gallery mode based optoplasmonic sensors

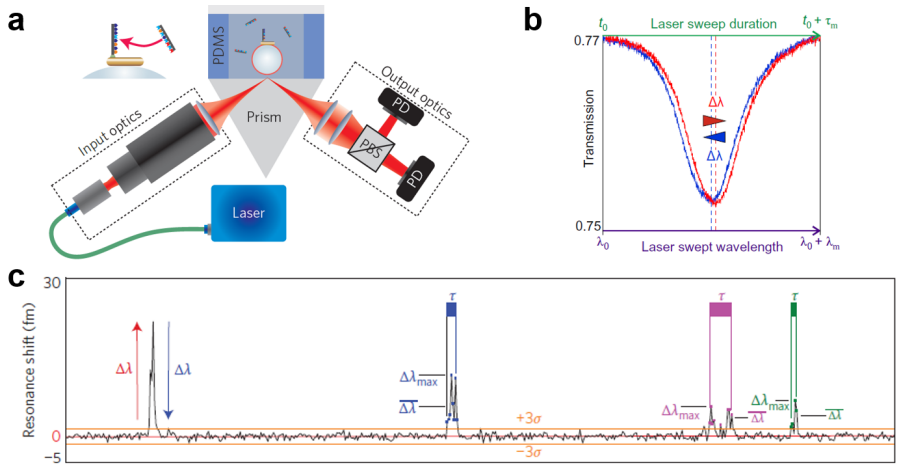

Figure 4.5: WGM based optoplasmonic sensing. (a) schematic graph of the optoplasmonic sensor. (b) The wavelength shift is caused by the interaction between molecules with plasmonic nanoparticles. (c) Normalised $\Delta\lambda$ time trace, the spike signal is caused by transient interactions. Image adapted with permission from[133].

.

To overcome the issues stated above, new techniques with exceptional sensitivity are required. In 2014, Baaske *etal*.[17] displayed a Whispering gallery mode (WGM) based single-molecular biosensor, a detection capability down to 8-mer single oligonucleotides was reported. This technique combines the localized surface plasmon resonance (LSPR) and whispering gallery mode (WGM) approaches, and the design of the experimental setup is shown in Figure 4.5a. For most single-channel optical devices, such as waveguides and optical interferometers, light interacts with analyte molecules or proteins only once. Therefore, to enhance the interaction between light and the sensing target, it is often necessary to increase the physical length of the sensor. However, in resonator-based sensors, light is confined to micron-level sensor elements, and light waves interfere constructively. One can increase the effective interaction length by increasing the optical quality factor (Q) of the resonant system. The binding of biomolecules will shift the WGM resonance frequency by a small amount. And this shift could be greatly enhanced by plasmonics since we can see that on the hotspot of gold nanorods the electromagnetic field is enhanced at least

thousands of times[17] (As shown in Figure 4.5b). The reason for the shift to longer resonance wavelengths is that the bound biomolecules will effectively ”pull” part of the field of view to the outside of the microsphere, thereby increasing the length of the round-trip path by $2\pi\Delta l$. This increase in path length results in a shift to lower frequencies ($\Delta\omega$)[134]. As a result, the optoplasmonic hybridized system can detect single molecules in parallel without labels, significantly increasing the sensing ability. Two years later, using the same technique, Baaske *etal*. have demonstrated the observation of single atomic ions interacting with plasmonic nanorods in an aqueous solution[134]. In 2017, the authors from the same group showed the detection of single enzyme-reactant reactions and associated conformational changes with the optoplasmonic sensing platform[135]. This technique has shown great potential in studying small single molecules. In Chapter 5 and 6 we show more results acquired with this technique.

4.3.1 Optical detection with whispering gallery modes

Optical microcavities confine light waves within a microscale volume by the reflection of light. An example of this is the Fabry–Pérot resonator, which is composed of two opposing mirrors. The constructive interference of the light propagating back and forth between two mirrors builds up the intensity at certain optical wavelengths, leading to optical resonance. The optical resonance is observed as a Lorentzian-shaped spectral feature, for instance, in the transmission or reflection spectrum of the microcavity. In the case of WGM microcavities, the light is confined within dielectric microstructures, such as glass microspheres with a diameter of about 80 μm, by means of total internal reflections that occur at the interface between the microcavity and its surroundings[136]. Using an appropriate optical coupler, only the evanescent field extends into the surrounding medium, from where the microcavity is excited. Owing to this unique light-confinement mechanism, WGM microcavities have small effective mode volumes V_{eff} while still preserving ultrahigh quality (Q) factors[137].

The prolonged time of the light circulating inside a WGM microcavity on resonance also results in a large number of round trips measured by the finesse (F) of the

microcavity (with F over 10^6 for a glass microsphere[138], for example). When a biomolecule diffuses to the microcavity surface and stays, the circulating light interacts with this entity F times, therefore boosting the sensing signal. In addition, WGM microcavities sensing is relatively easy to implement at a low cost. All these features contribute to an extensive application of WGM microcavities in biochemical, temperature and mechanical sensing[139]. The environmental perturbations that influence the spectral properties of WGMs can be monitored in real-time. Most common sensing mechanisms include mode splitting[140], resonance wavelength shift[141] and broadening[142]. Although WGM sensors show the capabilities of detecting single large protein[143] and virus[144], it remains difficult for small molecule detection, due to the limited sensitivity. In the next section, we address this issue by implementing LSPR nanoparticles to enhance sensitivity.

4.3.2 Nanoparticle enhanced optoplasmonic sensing

The simplest optoplasmonic sensing structure is composed of a WGM microcavity and a single nanoparticle located close to the microcavity surface. There are 3 main steps to assemble an optoplasmonic sensor in a typical single-molecule sensing experiment: (i) Glass microsphere fabrication. The glass microsphere is made by melting an optical fibre with a high-power laser. (ii) Binding of plasmonic nanoparticles. (iii) Change the buffer and introduce the molecules for sensing. The detailed protocol can be found in[17].

Around a microcavity, there may exist molecules of more than one species. Different molecules located at different positions may cause the same perturbation to the microcavity despite their different relative permittivities. Thus, it is not possible to distinguish the spectral shift caused by the molecules of a specific species. Addressing this issue requires extra preparation measures before the sensing operation. Let us focus on biosensing, where a microsphere is immersed in a sample solution containing the analyte molecules to be detected. A WGM transduces the binding of the biomolecules to the microsphere's surface into a resonance wavelength/frequency shift signal. To achieve a shift signal that is specific for the biomolecules of a certain species, it is necessary to modify the microsphere's surface with receptors (e.g.,

antibodies/DNAs), which bind selectively to the analyte and reject (or minimize) the interaction with the molecules of other species that may be present in the sample. In addition, it is necessary to prevent any unspecific binding of biomolecules to the microsphere sensor itself.

Chapter 5

Comparing transient DNA interactions using DNA-PAINT and optoplasmonic sensing

Narima Eerqing[1,2,+,*], *Subramanian Sivaraman*[1,2], *Jesus Rubio*[2], *Tobias Lutz*[1,2], *Hsin – Yu Wu*[1,2,], *Janet Anders*[2], *Christian Soeller*[1,2], *Frank Vollmer*[1,2]

[1]Living Systems Institute, University of Exeter, EX4 4QD, United Kingdom

[2] Department of Physics and Astronomy, University of Exeter, EX4 4QL, United Kingdom

*Email: ne276@exeter.ac.uk

This chapter present original research that was published as follows:

Eerqing, N., Subramanian, S., Rubio, J., Lutz, T., Wu, H.Y., Anders, J., Soeller, C. and Vollmer, F., 2021. Comparing transient oligonucleotide hybridization kinetics using DNA-PAINT and optoplasmonic single-molecule sensing on gold nanorods. ACS Photonics, 8(10), pp.2882-2888.

Abstract

We report a comparison of two photonic techniques for single-molecule sensing: fluorescence nanoscopy and optoplasmonic sensing. As the test system, oligonucleotides with and without fluorescent labels are transiently hybridized to complementary 'docking' strands attached to gold nanorods. Comparing the measured single-molecule kinetics helps to examine the influence of fluorescent labels as well as factors arising from different sensing geometries. Our results demonstrate that DNA dissociation is not significantly altered by the fluorescent label, while DNA association is affected by geometric factors in the two techniques. These findings open the door to exploiting plasmonic sensing and fluorescence nanoscopy in a complementary fashion, which will aid in building more powerful sensors and uncovering the intricate effects that influence the behavior of single molecules.

5.1 Background information

Biomolecules inhabit a microbiological environment sufficiently complex for their state to vary such that biological processes operate far from thermodynamic equilibrium. As a result, information extracted with ensemble measurements can be insufficient to predict the behavior of biomolecules, since ensemble averages may be far from the state of any single molecule in the system.[145, 146] The alternative is to probe biomolecular activity directly by using single-molecule techniques,[121, 147, 148, 149] which do not only provide mean values of physical observables but also more detailed statistics in the form of probability distributions. A plethora of photonics-based techniques for single-molecule detection has emerged in the past decade. For example, single-molecule localization microscopy

(SMLM)[85, 150, 151] has overcome the diffraction limit, enabling the reconstruction of images with great precision via temporal modulation and the accumulation of single-molecule detection events. Examples include photo-activated localization microscopy (PALM),[150] stochastic optical reconstruction microscopy (STORM),[85] and DNA-based point accumulation for imaging in nanoscale topography (DNA-PAINT).[152, 153, 154] On the other hand, single-molecule detection that makes use of noble metal nanostructures has attracted great attention owing to the exceptional sensitivity arising from localized surface plasmon resonance (LSPR).[155, 156] The local enhancements of optical near-fields around gold nanorods (GNRs) have enabled particularly high detection sensitivities for biomolecules without the need for fluorescent labels.[157, 158, 159] Among the family of LSPR-based techniques, the combination of whispering-gallery-mode (WGM) sensing with plasmonic nanorods (optoplasmonic sensing) has shown a very high detection sensitivity even down to small biomolecules such as short DNA oligonucleotides.[133, 134, 160]

Despite this steady progress, single-molecule techniques suffer from different drawbacks that limit the information one can extract. For example, it is well-known that fluorescent labels may affect the kinetics and dynamics of biomolecular systems,[161, 162, 163] while LSPR-based approaches use local field enhancements that are not uniform across a plasmonic nanostructure, and the local surface geometry and heterogeneity of plasmonic nanoparticles can play a significant role in the observed statistics.[164, 165, 166] In view of this, it is desirable to combine the information arising from different methods when applied to the same molecular system. But, to guarantee the validity of such an approach, current single-molecule techniques must be compared and cross-validated.

Here we compare the detection of DNA hybridization using two established photonic single-molecule techniques: DNA-PAINT and WGM-based optoplasmonic sensing (see schematic in Figure 5.1). We employ two sets of DNA strands, a 13-mer termed P1, a 22-mer termed T22 and their respective complementary strands (see Table 5.1). The complementary strands (termed imagers) are labeled (ImP1*D with ATTO 655 and ImT22*D with DY782) for use in DNA-PAINT, and unlabeled (ImP1* and

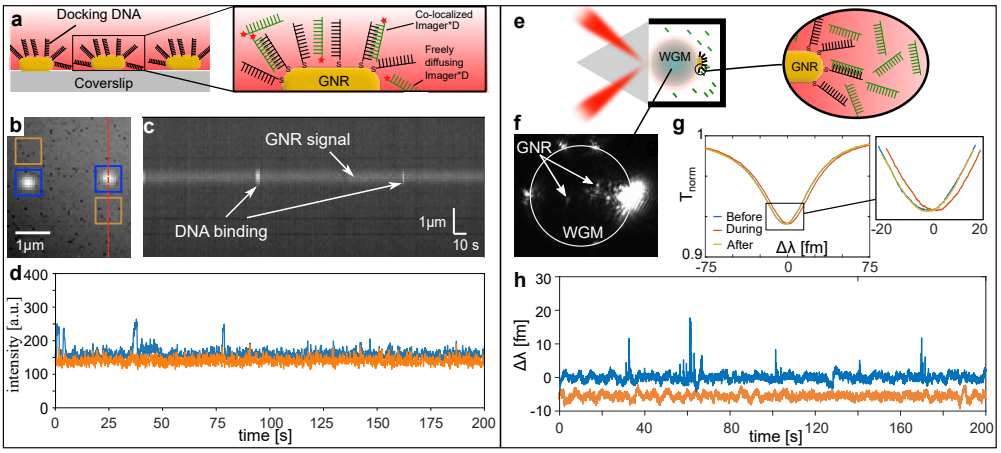

Figure 5.1: Comparison between DNA-PAINT (a-d) and WGM (e-h) methods. (a) Schematic of DNA-PAINT experiment on gold nanorods (GNRs). GNRs with LSPR $\sim$ 750 nm (yellow) are coated with DNA docking strands P1 or T22 (black) and immobilized on the surface of a coverslip (grey). The zoomed view shows a single immobilized GNR. Imager strands (green) labeled with flourophore (ATTO655/DY782, red star) are added and excited. (b) Microscope image showing the signals co-localized with the GNRs (blue box) and adjacent to the GNRs (orange box) positions. (c) A space-time plot of the red line through one GNR in (b). The GNRs provide a constant intensity over time and the hybridization of imagers are observed as short bursts of increased intensity. (d) Typical fluorescence time traces, with orange and blue lines showing the intensity signal at the locations indicated in (b). (e) Schematic of WGM sensing approach. A laser beam is focused on the surface of the prism and coupled into a glass microsphere. GNRs are then immobilized on the surface of the microsphere. The zoom-in shows docking strands P1 or T22 (black) immobilized on the GNRs surface and imager strands diffusing freely in solution. (f) Microscope image of the glass microsphere with GNRs immobilized on its surface. The scattering from the GNRs is observed as bright spots. (g) An example of wavelength shift caused by the hybridization of the imager and docking strands on the sensor. The blue, orange, and yellow curves represent the WGM mode position before, during, and after a single molecule transient event. (h) Typical detrended time trace of WGM resonance wavelength showing background signal (orange) and signals obtained for DNA hybridization (blue). All experiments were conducted at room temperature (22.5 ^{o}C).

ImT22*) for use with the optoplasmonic sensor. P1 and its imager strand ImP1* are short sequences which have been widely used in DNA-PAINT experiments. [152, 154, 167]. T22 is a 22-mer sequence which has been reported to work well in an optoplasmonic sensing platform.[133]. In both techniques, the P1 and T22 strands are attached to gold nanorods via thiol linkages and serve as the docking strands, while the imager strands are freely diffusing in solution. The oligonucleotide sequence is chosen to allow for transient hybridization events at room temperature. Within this context, a natural hypothesis is that the kinetics associated with the

dissociation of docking and imager strands is independent of the chosen platform. By carrying out the two experiments, DNA-PAINT and WGM, each for two types of DNA sets, such hypothesis can be tested.

Our measurements reveal that the dissociation rates of hybridized DNA strands are indeed approximately the same for both techniques, demonstrating the comparability of the single-molecule information extracted from each platform. In addition, this suggests that the modification of a short strand oligonucleotide with an fluorescent dye at its 5' end does not significantly affect the dissociation kinetics. On the other hand, the association rates cannot be directly estimated from our measurements. This is due to the surface heterogeneities of the gold nanorods,[134] as well as to the variability in the number of strands that are contributing to the signals in each technique. In the following we will detail how the experimental schemes and the data analysis have been carried out, before showing the main results in Fig. 5.3.

Table 5.1: Sequences of ssDNA used for the experiments.

	ssDNA	**Sequence (5'-3')**
Set I	P1	[ThiolC6] TTT TAT ACA TCT A
	ImP1*D	[Atto655] CTA GAT GTA T
	ImP1*	CTA GAT GTA T
Set II	T22	[ThiolC6] TTT TGA GAT AAA CGA GAA GGA TTG AT
	ImT22*D	[DY782] ATC AGT CCT TTT CCT TTA TCT C (3 mismatched)
	ImT22*	ATC AGT CCT TTT CCT TTA TCT C (3 mismatched)

5.2 Experiments protocol

Figure 5.1 shows the experimental schemes for both techniques employed in this work. In DNA-PAINT, the thiolated ssDNA are immobilized on to GNRs adsorbed to a glass coverslip as shown in Figure 5.1a. The hybridization of the labeled complementary DNA is observed by localization of a fluorescent label attached to the imager DNA using a camera. In the WGM-based optoplasmonic technique, the shift of the resonance wavelength λ of WGMs excited in a spherical glass resonator is

utilized to monitor the hybridization of the ssDNA. In practice, this involves tracking the changes in the WGM resonance position using a centroid method,[134, 168] from where we can obtain temporal traces for the wavelength shift $\Delta\lambda$. Similar to DNA-PAINT, a thiolated ssDNA is immobilised on to GNRs adsorbed to the glass resonator surface; see Figure 5.1e. In this case, the imager DNA strand does not contain a fluorescent label. The signals are instead obtained due to the plasmonic enhancement provided by the GNRs.[133]

For DNA-PAINT (Figure 5.1a), the experiments are carried out on a Nikon Ti-E inverted microscope with a 1.49 NA total internal reflection fluorescence (TIRF) objective (Nikon Apo TIRF 60X oil or Nikon Apo TIRF 100x oil) illuminated using a 647nm (OMicron LuxX 647- 140) or 780 nm (Toptica DL Pro, 100mW) and custom-built optics. The fluorophores are excited via TIR at a coverslip (170 μm nominal thickness) and the images are captured real-time by a camera (Andor Zyla 4.2, 10 frames/s or Andor iXON 888, 25 frames/s). The glass coverslip is glued to a chamber cut from acrylic and placed on the microscope stage. The acrylic chamber is used to pipette the various samples required for the experiments. For the WGM technique (Figure 5.1e), the experiments are carried out in a custom built prism based setup. Whispering gallery modes in spherical glass resonators (diameter $\sim$ 80 μm) fabricated by melting a single mode optical fiber (SMF 28e, Corning) are excited via frustrated total internal reflection at a prism (NSF11, Schott) surface. A microscope setup (10x Olympus) is used to help align the resonator with respect to the prism for efficient coupling. A tunable 780 nm laser source (Toptical TA Pro 780) is scanned at a rate of 50 Hz to capture the WGM spectrum. The position of the resonance peak and the full-width-at-half-maximum (FWHM) are extracted using a custom Labview program. A chamber made of Polydimethylsiloxane (PDMS) is placed around the resonator and is used for injecting samples into the sensor. All experiments were conducted at 22.5 ^{o}C.

We carry out both the DNA-PAINT and optoplasmonic sensing experiments for two sets of DNA strands (see Table 5.1). The procedures of the experiments are similar, and contain three steps. First, we immobilize gold nanorods (A12-10-CTAB-750;

Nanopartz Inc.) irreversibly on a clean glass surface (a coverslip in case of DNA-PAINT or the spherical resonator surface in case of optoplasmonic sensor) in an acidic aqueous suspension (pH ≈1.6, 0.1 nM). This step is run over for 15 min for the GNRs to freely deposit. The chamber is washed thrice to remove unbound GNRs. On average, the diameter of GNRs is 10 nm, and their length is 35 nm with a longitudinal plasmon resonance at 750 nm. In DNA-PAINT, the clean coverslip is pre-functionalized with PLL-g-PEG (Su-Sos) whose role here is to prevent unspecific binding between fluorophore and the coverslip. In the DNA-PAINT setup, the GNRs are excited via TIR at the coverslip and their photoluminescence is visualized real-time by the sCMOS/EMCCD camera. In the optoplasmonic sensing platform, the immobilization of the GNRs are monitored via the shift in WGM resonance wavelength and FWHM. Some of the attached GNRs can also be monitored via the microscope as shown in Figure 5.1f.

Next the docking strands (thiolated ssDNA) are immobilised on the GNRs via a mercaptohexyl linker at their 5' end. The procedures are the same for both techniques. The P1 docking strand (see Table 5.1 for sequences) are immobilised in citrate buffer at pH ≈ 3 with 1 M of NaCl. The T22 docking strands are immobilised at the same pH and salt concentration, but with different buffer: 0.02% wt/wt sodiumdodecylsulfate (SDS) solution. Before the addition of the docking strands into the sample chamber, they are pre-mixed with a solution of a reducing agent (10 μl of 10 mM tris(2-carboxyethyl)phosphine, TCEP) to cleave the disulfide bond and therefore enable efficient binding of the thiols to the GNRs. The docking strands are then injected into the sample chamber to a final concentration of 1 μM and left for 30 mins. Since the docking strands do not contain any fluorescent labels, the binding of the docking strands to the GNRs are not monitored in DNA-PAINT. In contrast, in the optoplasmonic sensor step-like signals are observed upon binding of the docking strands to GNRs. It has to be noted here that only a subset of all the docking strands attached to the GNRs provide step signals due to the different plasmonic enhancements at each binding site.

Finally, the transient interactions between the docking and imager strands are moni-

tored in both techniques. After loading of the docking strands, the excess DNA in the sample chamber was removed by rinsing the chamber thrice with milli-Q water. The imager strands were then injected into the sample chamber at various concentrations. A buffer of Tris-EDTA (TE buffer, pH $\sim$ 8) with 500 mM NaCl was used for the experiments with P1 and its complementary, and a solution at pH $\sim$ 7 (milli-Q water) with 10 mM NaCl was used for the T22 DNA experiments. The different conditions were chosen to optimize the number of events observed to extract the various rates (P1 and T22 have very different melting temperatures[169]). In DNA-PAINT, we then added the corresponding imager strands with dyes, i.e. ImP1*D modified with ATTO 655 (5' end) and ImT22*D with DY782 (5' end) for the docking strands P1 and T22, respectively. In each experiment, only one docking strand and the corresponding imager strand were used. The fluorescence signals from the hybridization of the DNA strands were recorded over time and co-localized with the position of the GNRs, as shown in Figure 5.1b (blue boxes). Figure 5.1c shows a space-time plot for the red line shown in Figure 5.1b. The constant intensity background indicates the GNR photoluminescence, and the burst of intensity indicates DNA hybridization between docking strands and imager strands that co-localized within GNR position. Fluorescent times traces can then be extracted using this information. An example is shown in Figure 5.1d. The blue curve shows the DNA hybridization between P1 and ImP1*D, and the orange curve displays the background signal adjacent to the GNR position. Along this time trace, most of the signals we observe are spike-like, although it is also possible to detect plateau-like signals (see Figure 5.2a) indicating prolonged interactions between imager and docking strands. In the case of the optoplasmonic sensor the imagers without fluorescent labels, ImP1* and ImT22* were used. Again, in each experiment only one set of docking and the corresponding imager strand was used and the imager concentrations was increased in steps. Upon addition of the imagers, the WGM resonance position shifts (see Figure 5.1g) and spike like transitions can be observed in a time trace of the WGM resonance position ($\Delta\lambda$). Figure 5.1h shows the spike signals due to interaction of the complementary DNA strands (blue) and the background with no spike signals before addition of the

imager (orange).

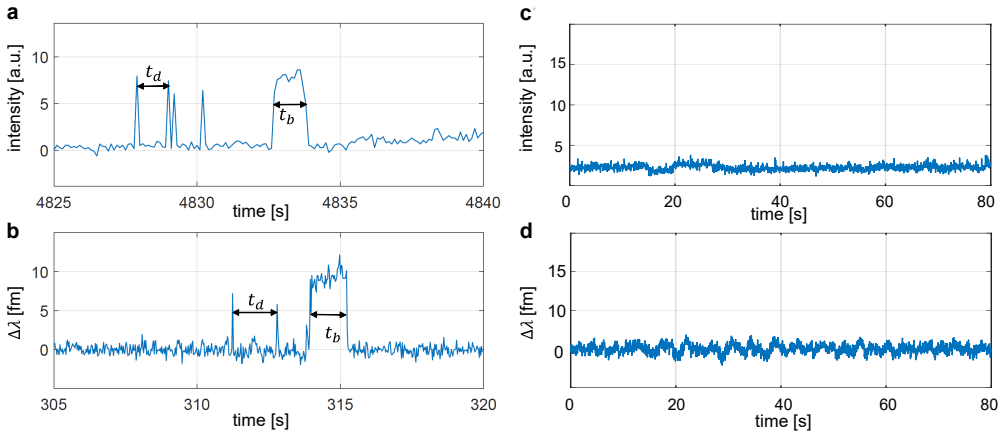

Figure 5.2: (a,b) Examples of traces generated by the interactions between P1 docking and ImP1* imager strands in (a) the DNA-PAINT experiment, and (b) the optoplasmonic sensing technique. Similar traces can be observed for the T22 strands. Here t_b denotes the time that a strand spends in a bounded state, while t_d indicates the time between detected single-molecule hybridization events. (c,d) Control measurements of unrelated DNA strands for DNA-PAINT and WGM experiments, respectively. A lack of activity was observed in both cases, thus indicating that the observed DNA hybridization is specific to the sequences.

5.3 Results and discussion

DNA hybridization has previously been reported[167, 170] to follow (pseudo) first-order kinetics. Considering a single docking strand that can be found in two states, either bounded with a single imager strand or dissociated, the probability that a binding event does not take place in an interval t_d (dissociated waiting time), also called survival probability, is $P^s(t_d) = \exp(-k_s t_d)$, where k_s is a single-molecule binding rate with units of s^{-1} (also known as association rate). However, the traces of both experiments (Figure 5.2) record the signal of binding events triggered by many imager strands, and the chance of observing the binding of one of the imagers in the chamber is further affected by the arrangement and accessibility of docking strands contributing to the signals on each sensor. The probability distribution for the waiting time to detect the binding of any one of the imagers, assuming independence of events, is then $P(t_d) = \exp(-kt_d)$, where $k = k_{on}\gamma c_i$ is a rate with units of s^{-1}. Here, k_{on} is the usual on-rate constant per unit of concentration, γ is a numerical factor accounting for the geometric arrangement of the docking strands

and their contribution to the observed signals, and c_i is the imager concentration. Since the factor γ is constant within the same experiment we expect that, for each experiment, the rate k grows linearly with c_i. Once a docking strand is bound, the probability that dissociation does not take place in an interval t_b (bound waiting time) is $P(t_b) \simeq \exp(-k_{\text{off}} t_b)$, where k_{off} is the dissociation rate constant and, in this case, equivalent to a single molecule dissociation rate with units of s^{-1}. In other words, we expect k_{off} to be concentration-independent.[167, 170] Note that the approximation holds provided that the chance of two imagers being bound at the same time is negligible, which is achieved by making the imager concentration sufficiently low.

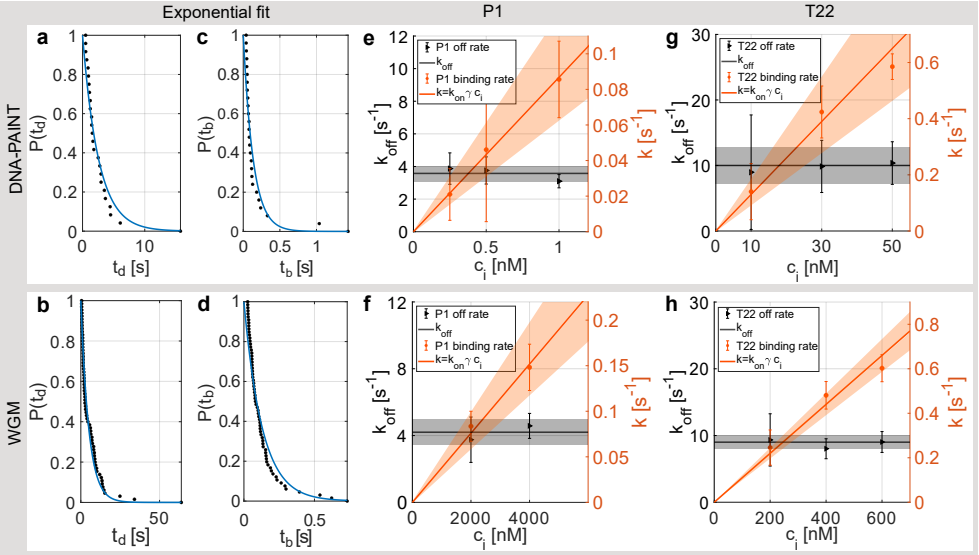

Figure 5.3: (a,b) Shown are the probabilities P that a binding event has not taken place within an interval t_d for (a) DNA-PAINT with 50nM of ImT22*D and (b) WGM experiments with 200nM of ImT22*, measured (black dots) and fit (blue line). (c,d) Similarly, the probability that a dissociation event has not taken place within an interval t_b is shown in (c) DNA-PAINT with 50nM of ImT22*D and (d) WGM experiment with 200nM of ImT22*. For P1 strands, analogous exponential profiles emerge. (e-h) The single-molecule dissociation rate k_{off} (black) and the binding rate $k = k_{\text{on}} \gamma c_i$ (orange), both with units of s^{-1}, are shown for P1 and T22 strands with (e,g) DNA-PAINT and (f,h) WGM sensing, respectively, where k_{on} is the association rate constant with units of $\text{M}^{-1}\text{s}^{-1}$, γ is a numerical factor accounting for the geometric arrangement and accessibility of the docking strands contributing to the signals, and c_i is the molar imager concentration. Our results show that the dissociation rate for the DNA-PAINT and the WGM techniques are the same within error. For binding kinetics, only the product $k_{\text{on}}\gamma$ is retrieved. The uncertainties associated with k and k_{off} are given, for each exponential fit, by $\text{SE} \times t_{n-1}$, where SE is the standard error and t_{n-1} is the t-value for $n-1$ degrees of freedom at a 95% level. The uncertainties for the linear fits have been propagated from the former uncertainties.

Using the values for the two waiting times, t_d and t_b, all measured at temperature 22.5 °C, we computed the empirical distributions $P(t_d)$ and $P(t_b)$, both for the DNA-PAINT experiment (dotted line in Figures 5.3a,c) and the WGM platform (dotted line in Figures 5.3b,d). As expected, exponential profiles emerge, from which the rates k and k_{off} are extracted for different molar imager concentrations c_i.

The single-molecule dissociation rate k_{off} can be directly obtained from the fits to $P(t_b)$ in Figure 5.3c (DNA-PAINT) and Figure 5.3d (WGM). As expected, the k_{off} values are indeed approximately constant across all trials with different imager concentrations c_i, as can be seen in Figure 5.3e-h (black lines). For P1 strands, the average dissociation rates are $k_{\text{off}}^{\text{PAINT}} = 3.6 \pm 0.4\,\text{s}^{-1}$ and $k_{\text{off}}^{\text{WGM}} = 4.2 \pm 0.8\,\text{s}^{-1}$ (estimate $\pm$ uncertainty; see caption of Fig. 5.3) for DNA-PAINT and WGM, respectively. Thus the value of k_{off} measured by both techniques is the same within error, suggesting that the fluorescent dye molecule in ImP1*D does not significantly alter the kinetics for the DNA hybridization under study. The k_{off} values for the T22 strands, $k_{\text{off}}^{\text{PAINT}} = 10 \pm 3\,\text{s}^{-1}$ and $k_{\text{off}}^{\text{WGM}} = 9 \pm 1\,\text{s}^{-1}$, lead to an analogous conclusion. Nevertheless, previous studies[170] have shown that the kinetics of biomolecular systems can be influenced by the presence of fluorophores, and so the impact of fluorophores may have to be examined in a case-by-case basis. The compatible k_{off} values also show that there is no evidence of a local temperature increase due to the near-field enhancement of the GNRs at the light intensities used in both techniques.

The relationship between k and c_i further provides the product $k_{\text{on}}\gamma$. For P1 strands, a linear fit yields $k_{\text{on}}\gamma^{\text{PAINT}} = (8.7 \pm 3.4) \times 10^7\,\text{M}^{-1}\text{s}^{-1}$ and $k_{\text{on}}\gamma^{\text{WGM}} = (3.9 \pm 0.5) \times 10^4\,\text{M}^{-1}\text{s}^{-1}$ for the DNA-PAINT and optoplasmonic experiments, respectively. Similarly, for T22 strands we find $k_{\text{on}}\gamma^{\text{PAINT}} = (1.3 \pm 0.4) \times 10^7\,\text{M}^{-1}\text{s}^{-1}$ and $k_{\text{on}}\gamma^{\text{WGM}} = (1.1 \pm 0.1) \times 10^6\,\text{M}^{-1}\text{s}^{-1}$. These fits are shown in Figures 5.3e-h (orange lines), and, for both techniques, we see clear evidence of a linear dependence between k and c_i. The value of k_{on} for each strand cannot be determined without detailed knowledge of the geometric factors. An exact calculation of γ for each technique lies beyond of the scope of the present work, but we can highlight some factors contributing to its value. First, all docking strands contribute to the signal in

DNA-PAINT, whereas only a subset of the docking strands in the WGM technique (attached to the tips of the GNRs) contribute to the signal. Additionally, the local surface properties will be different for the tips compared to the sides of the GNRs [164, 165, 166]. Kim *etal*. .[171] observed an average of 62 ± 6 thiol binding events using the WGM-based optoplasmonic sensor. Moreover, Elzey *etal*. [172] report an average size-independent packing density of $7.8 \pm 1.2\,\mathrm{nm}^{-2}$ for thiolated molecules binding to 10-100 nm GNRs. From these, we estimate that only $\sim 0.6\%$ of the docking sites per GNR contribute to the signals in the WGM-based optoplasmonic sensor. This already suggests that $k_{\mathrm{on}}\gamma$ can be smaller for the WGM sensor than for DNA-PAINT, in consistency with our measurements. Of particular importance is the fact that, in the WGM experiment, the plasmonic enhancement may be insufficient for many docking sites due to the random deposition of the GNRs on the surface of the microsphere, thus failing to detect signals that lie below the noise level. For P1 strands, this is reflected in that only when applying a micromolar concentration of imager strands can one detect a significant number of events. In contrast, for T22 strands the number of events is significant already in the range of hundreds of nM. This gives a plausible explanation of why the discrepancy between $k_{\mathrm{on}}\gamma^{\mathrm{PAINT}}$ and $k_{\mathrm{on}}\gamma^{\mathrm{WGM}}$ is only of ~ 10 for the T22 strands, but of $\sim 10^3 - 10^4$ for the P1 strands.

5.4 Conclusion

Here we have compared two optical single-molecule detection techniques, fluorescence-based single-molecule localization (DNA-PAINT) and optoplasmonic WGM sensing, that utilize the same plasmonic nanoparticles for detecting DNA hybridization events between surface immobilized docking strands and imager strands in solution. The rate constant k_{off}, which characterizes the dissociation of the DNA sequences used here, should depend only on the oligonucleotide sequence and length (buffer and temperature conditions are the same for each type of DNA across both experimental setups) while being independent of the different geometric factors of the two experiments. Indeed, we found k_{off} to be the same in both experiments, within experimental error. This establishes the equivalence of each technique for

test systems used in this work and can serve as the basis for consistently combining these techniques in future single-molecule studies. In particular, to establish the dissociation rates for other processes, one may benefit from the larger binding efficiency of DNA-PAINT, while checking the label-impact with the WGM platform.

Author Information

Corresponding Author

*ne276@exeter.ac.uk

Author Contributions

N.E. and J.R. analyzed the data and wrote the manuscript.; S.S. carried out the WGM-based experiment; N.E., T.L. and S.S. conducted the DNA-PAINT experiments; N.E.,T.L. and C.S. analyzed the raw DNA-PAINT data; H.-Y.W. trained N.E. in conducting experiments; J.A. advised on the data analysis and supervised the project; C. S. and F.V. conceived the study. All authors contributed to writing the manuscript.

Notes

The authors declare no competing financial interests.

5.5 Acknowledgement

N.E. acknowledges funding from the EPSRC Centre for Doctoral Training (CDT) in Metamaterials (XM2) (EP/L015331/1). N.E., H.-Y.W. and F.V. acknowledge support from EPSRC (EP/R031428/1). S.S., J.R., J.A. and F.V. acknowledge support from EPSRC (EP/T002875/1). J.A. acknowledges support from EPSRC (EP/R045577/1) and the Royal Society. C.S. acknowledges support from EPSRC (EP/N008235/1).

Chapter 6

Anomalous DNA hybridisation kinetics on gold nanorods revealed via a dual single-molecule imaging and optoplasmonic sensing platform

Narima Eerqing[1,2,+,*], *Hsin – Yu Wu*[1,2,+], *Subramanian Sivaraman*[1,2], *Serge Vincent*[1,2], *Frank Vollmer*[1,2]

[1]Living Systems Institute, University of Exeter, EX4 4QD, United Kingdom

[2] Department of Physics and Astronomy, University of Exeter, EX4 4QL, United Kingdom

+These authors have contributed equally. *Email: ne276@exeter.ac.uk

This chapter present original research that is currently under submission.

Abstract

Observing the hybridisation kinetics of DNA probes immobilised on plasmonic nanoparticles is key in fluorescence based super-resolution microscopy, such as in DNA-PAINT and refractive index based single-molecule detection on optoplasmonic sensors. The role of the local field in providing plasmonic signal enhancements for single-molecule detection has been studied in great detail. Nevertheless, few studies have compared the experimental results in both techniques for single-molecule studies. Here we developed the first optical setup that integrates optoplasmonic and DNA-PAINT based detection of oligonucleotides to compare these sub-platforms and provide complementary insights into single-molecule processes. We record the fluorescence and optoplasmonic sensor signals for individual, transient hybridisation events. The hybridisation events are observed in the same sample cell and over a prolonged time (i.e. towards high binding site occupancies). A decrease in the association rate over the measurement duration is reported. Our dual optoplasmonic sensing and imaging platform offers insight into the observed phenomenon, revealing that irreversible hybridisation events accumulate over detected step signals in optoplasmonic sensing. Our results point to novel physicochemical mechanisms that result in the stabilisation of DNA hybridisation on optically-excited plasmonic nanoparticles.

6.1 Background Information

The interaction between DNA strands is key to many fundamental processes in the cell. The hybridization between DNA oligonucleotides is fundamental to our most sensitive methods for DNA detection, including state-of-the-art single-molecule techniques[17, 16, 173]. Single-molecule techniques have enriched biomolecular studies by providing details about the kinetics of biological reactions and physiological processes that is not apparent in their corresponding bulk measurements. Powerful new approaches to single-molecule sensing and imaging have emerged in the last few decades. One example is fluorescence based single-molecule imag-

ing, which overcomes the diffraction limit by reconstructing images from high-precision temporal modulation and the accumulation of single-molecule detection events[174, 175, 176, 177]. Among these, photo-activated localisation microscopy (PALM) [84, 178], stochastic optical reconstruction microscopy (STORM) [48, 179], and DNA based point accumulation for imaging in nanoscale topography (DNA-PAINT) [86, 180, 181, 182] have robustly demonstrated single-molecule localisation microscopy at the nanoscale. On the other hand, noble metal nanoparticles of various morphologies have drawn attention for their use in single-molecule sensing due to their extraordinary optical properties derived from localised surface plasmon resonances (LSPRs). In a large range of applications, plasmonic nanoparticles have been employed to amplify single-molecule detection signals. Examples for this are the plasmonic enhancement of fluorescence based signals in bioimaging [183, 184, 185] and the enhancement of the label-free signals from whispering-gallery mode (WGM) sensors [186, 17, 187, 16, 188, 1, 189].

Along with the development of various single-molecule techniques, it is becoming increasingly important to compare and cross-validate their results [1]. Detecting a single-molecule process on two different optical instruments enables one to gain a deeper understanding of the biomolecular system under investigation. Recently, we reported a study in which we compare DNA hybridisation events observed on plasmonic nanorods using an optoplasmonic sensor, with the results obtained on a single-molecule imaging technique based on DNA-PAINT [16]. The optoplasmonic sensor measures single-molecule events within the enhanced near field of plasmonic gold nanorods (GNRs) that are attached to an optical WGM surface. The signals are obtained indirectly via the shift in the resonance of the WGM. On the other hand, DNA-PAINT provides signals via fluorescence localization microscopy. Although DNA-PAINT does not require plasmonic enhancement, we performed all DNA-PAINT experiments with molecular interactions on the surface of GNRs to replicate the conditions of the optoplasmonic sensor system. We found that both techniques deliver comparable results. Specifically, we found DNA dissociation kinetics (i.e. off-rates) for both schemes lay within experimental error.

In this article, we demonstrate the first use of a total internal reflection fluorescence (TIRF) objective to perform label-free optoplasmonic sensing and fluorescence imaging of single molecules in one optical platform. The TIRF objective is employed as an evanescent coupler similar to common coupling methods such as prism, grating, end-fibre and wave guide couplers to evanescently excite the WGMs on glass microspheres while enabling single-molecule imaging capability. We use this platform to study the hybridisation kinetics of DNA oligomers attached to gold nanorods

(GNRs). We chose to study the interaction between DNA oligonucleotides because recent reports show that DNA hybridisation kinetics on GNRs are seemingly affected by the experimental single-molecule technique. In 2018, Weichun *et al.*[190] studied the single-molecule fluorescence enhancement from GNRs, reporting a disappearance of DNA hybridisation events over time. This phenomenon was, however, not observed for 'docking' strands (immobilized single stranded DNA) bound to glass. Previously, Taylor *et al.*[191] conducted DNA-PAINT experiments on gold nanorods to reconstruct single GNR geometry. They also reported a similar reduction and disappearance of DNA hybridisation events for 'docking' strands attached to GNRs. Weichun *et al.*[190] attributed this effect to the cleaving of $Au-S$ bonds and thus removal of the docking DNA strands bound to the GNRs by hot electrons generated in the GNRs. Studying the decrease in DNA hybridisation event frequency on our dual single-molecule fluorescence imaging and optoplasmonic sensing platform would provide more detailed insight into the mechanisms behind the reported phenomenon. By probing single-molecule kinetics with fluorescence and optoplasmonic refractive index based methods in parallel, we obtain results which show that the anomalous disappearance of DNA hybridisation events over time on GNR arises from the probabilistic permanent binding of complementary strands and that this is not a result of hot electron cleaving of $Au-S$ bonds.

6.2 Dual sensing and imaging setup

Figure 6.1 shows the schematic of the experimental setup that we have developed for dual single-molecule imaging microscopy and optoplasmonic sensing (SIMOPS). Light from a tunable external cavity diode laser (Toptica DL pro 780) is collimated, expanded, and focused onto the back focal plane of a TIRF objective (CFI Apo TIRF 100X, 1.49 NA, Nikon). The total internal reflection (TIR) off a glass coverslip is used to evanescently couple to optical WGMs of a fused silica microsphere similar to evanescent coupling via prisms[17]. The reflected light is then collimated and collected by a lens L4, and a switchable mirror (SM) onto a photodetector (PD). Alternatively, the evanescent field originating from TIR off the glass coverslip is used to excite plasmonic GNRs and dye molecules directly near the surface of the glass coverslip. (Please refer to Supplementary Figure S1 for details of field enhancements.) In this case, a fluorescence image is obtained by replacing the lens L4 with a switchable emission filter and collecting the emitted photons on an EMCCD camera (Andor iXon 888).

Figure 6.1a shows a schematic of the DNA-PAINT measurements. Firstly, plasmonic GNRs are immobilised on the surface of a glass coverslip that is placed in the sample

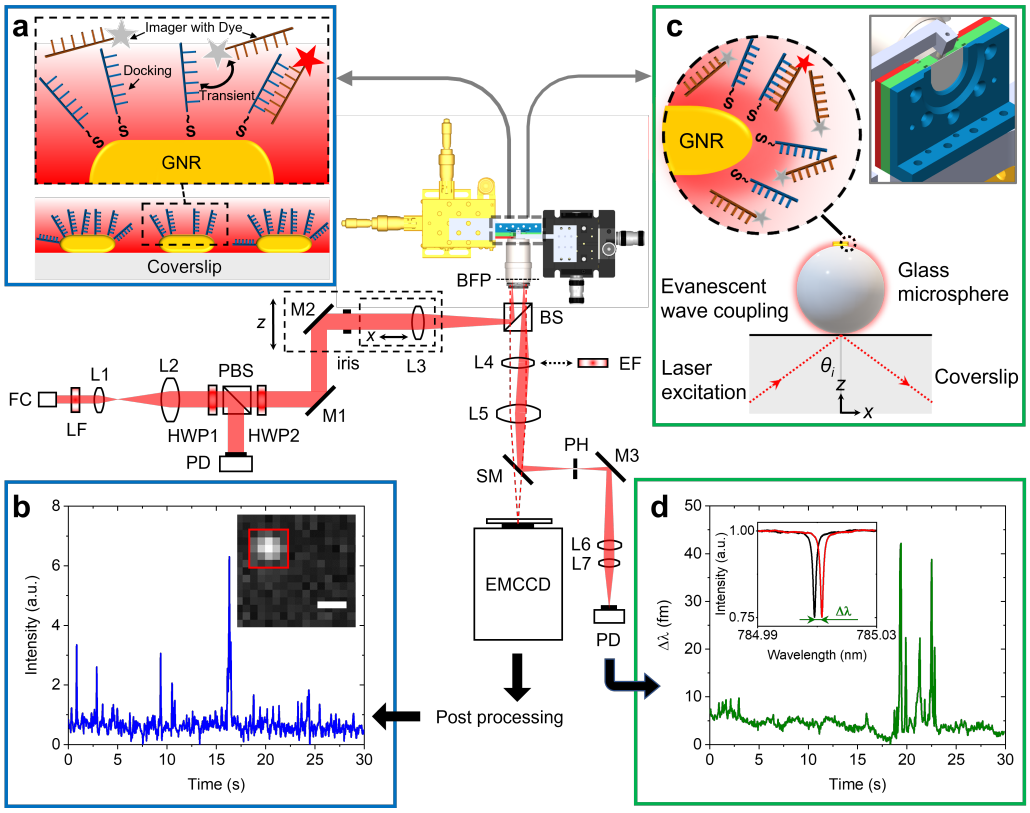

Figure 6.1: Design of the dual optoplasmonic sensing and imaging platform. Incident laser beam is focused onto the back focal plane of a TIRF objective, establishing total internal reflection on the glass coverslip surface. Generated evanescent wave is then coupled into the WGM. (a) Schematic of DNA-PAINT imaging. The zoomed-in view shows the transient interaction between freely defusing imager DNA strands and docking DNA strands immobilised on the GNRs. (b) Typical intensity time trace extracted from colocalised events in the 5× 5 pixels (with red ROI box in the inset) around the GNR. The scale bar = 500 nm. (c) Schematic describing the optoplasmonic sensing principle. The zoomed-in view shows imager strands interact with docking strands, wherein the imager denoted by a red star is the molecule that contributes to the signal. The inset depicts the chamber and microsphere positioning. (d) Typical WGM resonance wavelength trace obtained by tracking the resonance peak position (with Lorentzian lineshape shown in the inset). FC: fiber-coupled collimator; LF: laser-line filter; L: lens; HWP: half-wave plate; PBS: polarizing beam splitter; M: Mirror; BS: non-polarizing beam splitter; BFP: back focal plane; EF: emission filter; SM: switchable mirror; PD: photodetector.

chamber. The GNR attachment can be monitored in real-time via the photoluminescence of the GNRs as shown in Figure 6.1b inset (highlighted by the red box). Secondly, DNA docking strands are then anchored onto the GNRs via mercaptohexyl linkers. The sample chamber is then rinsed to remove excess, unbound DNA strands. Finally, complementary DNA strands with a fluorescent label (DY782) are added to the sample chamber (See Materials and Methods for more details). The transient hybridisation of freely-diffusing imager strands and fixed docking strands then pro-

duces an increased intensity at the GNR location. The intensity integrated within a region-of-interest (ROI) of 5 × 5 pixels around the GNR position then provides the intensity time traces as shown in Figure 6.1b. The captured ROIs are stacked and processed in Fiji (ImageJ) via a single-molecule localisation microscopy package named ThunderSTORM[192].

Figure 6.1c shows the schematic of the experiments performed using the optoplasmonic technique. In this case, light is coupled to WGMs in an 80 µm glass microsphere[186] placed near the coverslip surface. GNRs are then attached to the microsphere surface. Subsequently, docking DNA strands are immobilised on the GNRs with a protocol similar to that for the DNA-PAINT. Once the fluorophore-labeled imager strands are added to the sample chamber (Detailed protocol can be found in the Materials and Methods section), hybridisation of the imager strands with the docked DNA strands is observed in the form of a shift in WGM resonance frequency (See inset of Figure 6.1d). These frequency shifts are recorded over time to obtain the single-molecule time traces as shown in Figure 6.1d (See Materials and Methods for further context).

6.3 Results

Signal Types and Dissociation Kinetics from Optoplasmonic and DNA-PAINT Measurements

DNA hybridisation is characterised using both optoplasmonic sensing and DNA-PAINT. Two sets of DNA docking strands (P1/T22) and the corresponding imager strands (ImP1*D/ImT22*D) were utilised in both experiments, their sequences are detailed in Table 6.1. Figure 6.2 displays the typical signal type from a data trace. It can be seen that most signals along these time traces are spike-like with a short dwell time regardless of the chosen measurement technique. Prolonged plateau-like signals were, however, also observed as in the central traces (T2 time interval) of Figure 6.2a, b. Positive step-like signals with no corresponding falling-edge were observed in the case of the optoplasmonic sensor (T3, Figure 6.2a). These signals most likely correspond to the permanent occupation of a docking strand by an imager strand. On the contrary, no such step signals were observed in the DNA-PAINT experiments. In this case, longer plateau-like signals (T3, Figure 6.2b) were observed instead. The spike-like signals and transient plateau signals in both techniques (i.e. Signals in Figure 6.2a, b's T1,T2) correspond to reversible / transient interactions between the imager and docking strands. The step signal is only observed for the optoplasmonic sensing method, correlating to the permanent (explicitly, within the

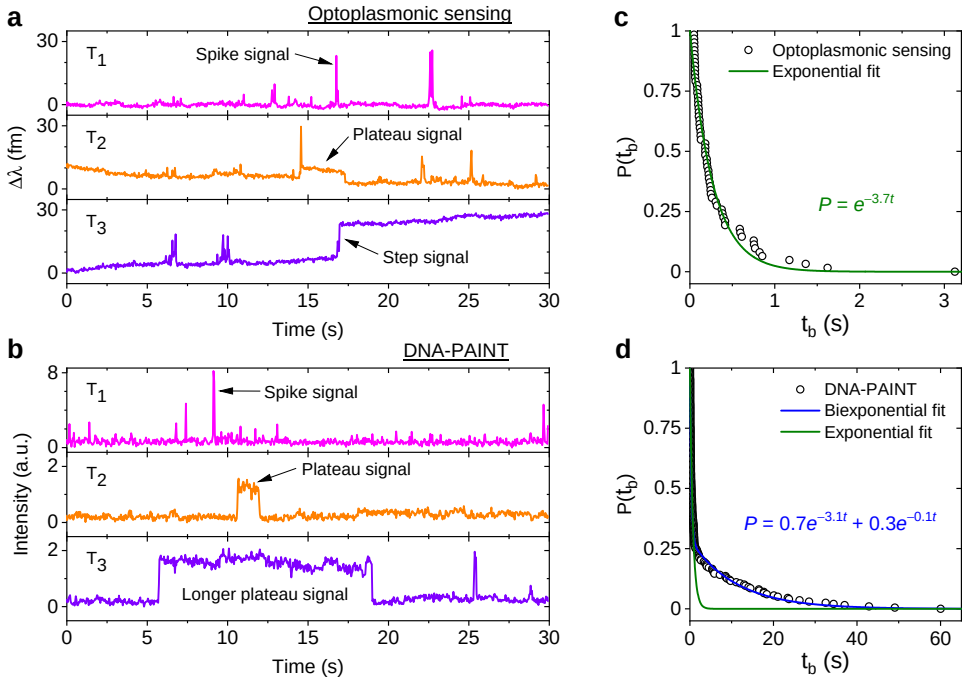

Figure 6.2: Three types of DNA hybridisation signals. Signals obtained from (a) optoplasmonic sensor and (b) single-molecule imaging platform at different time intervals (T1,T2,T3). (c) Measured t_b from the P1 optoplasmonic data and its single exponential fit. The probabilities $P(t_b)$ represent a dissociation event has not taken place within an interval t_b .(d) $P(t_b)$ for the same P1 DNA sets measured by DNA-PAINT and their single (green) and bi-exponential (blue) fits.

timescale of the experiment) hybridisation of the complementary strand[17]. On the other hand, DNA-PAINT only provides plateau-like signals with a longer duration (T3, Figure 6.2b). We hypothesise that these long-duration, plateau-like signals also correspond to permanent hybridisation events. The falling edge is thus likely due to photobleaching of the dye after a permanent hybridisation event rather than from dissociation of the DNA strands.

We further analysed the signals to extract the dwell time of events t_b in case of spike-like and plateau-like signals, and the arrival time between consecutive events t_a. Figure 6.2c, d plots the survivor function for the signal dwell time t_b measured with both techniques. It can be seen that the data from the optoplasmonic sensor (Figure 6.2c) closely matches a single exponential fit, corresponding to a single Poisson process. The dwell rate estimated from a single exponential fit is $k_{\text{off}}^{\text{OP}} = 3.7 \pm 0.1\ \text{s}^{-1}$. However, in the case of the DNA-PAINT measurement (Figure 6.2c), the distribution of dwell times largely deviates from a single exponential. A bi-exponential model provides a better fit, where two rates $k_{\text{off},1}^{\text{PAINT}} = 3.1 \pm 0.1\ \text{s}^{-1}$ and $k_{\text{off},2}^{\text{PAINT}} = 0.10 \pm 0.06\ \text{s}^{-1}$ are obtained. The rates $k_{\text{off}}^{\text{OP}}$ and $k_{\text{off},1}^{\text{PAINT}}$ have similar values

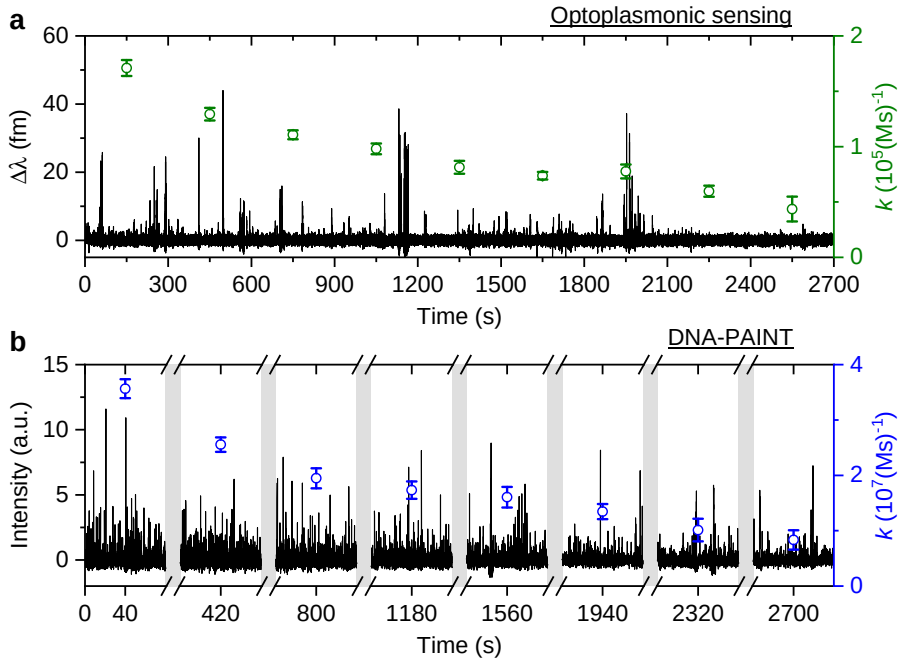

Figure 6.3: T22 DNA association rates change measured over time. Experiments are carried out with optoplasmonic sensing and DNA-PAINT approaches with 10mM NaCl buffer. (a) Detrended optoplasmonic sensing trace for 1 µM ImT22*D and association rate (green circles) calculated every 300 s. (b) DNA-PAINT fluorescence time trace with 20 nM ImT22*D, with association rates (blue circles) measured every 5 minutes within time intervals of 80 s. The uncertainties of the association rates are extracted from exponential fits

which correspond to the binding dwell time of the DNA strands. The rate $k_{\text{off},2}^{\text{PAINT}}$, however, likely corresponds to the average photobleaching time of the dye molecule under experimental conditions.

Measuring Association Rate Change Over Time

The signal patterns and dwell time analysis above indicate that the spike-like signals arise from transient DNA hybridisation. The step-like signals for the optoplasmonic sensor and the long plateau-like signals in DNA-PAINT likely arise from hybridisation / blocking of docking DNA. Furthermore, the analysis of dwell times indicates that longer plateau-like signals in DNA-PAINT correspond to a permanent blocking of a DNA docking strand by an imager strand and subsequent photobleaching of the dye attached to the imager.

To study the anomalous behaviour of DNA hybridisation kinetics on GNRs as was previously reported[191, 190], we performed long timescale measurements ($\sim$ 45 mins) of DNA hybridisation. To ensure the observation was not sequence dependent, we utilised the second set of DNA strands: T22 and the corresponding imager (See Table 6.1). The experimental protocol for DNA functionalisation and imaging is

the same as in the previous trial. Figure 6.3 (black traces) shows the long time traces obtained from both techniques. The concentration of the imager strands for optoplasmonic sensing and DNA-PAINT measurements are 1 µM and 20 nM, respectively. Different concentrations are used for optoplasmonic and DNA-PAINT measurements due to the different distributions of detectable docking sites[16]. In the case of DNA-PAINT (Figure 6.3b), 5 min of idle time in the measurement is delineated by break lines.

The plots in Figure 6.3 show the anomalous behaviour of a decrease in the number of events over time for both techniques. To identify the decreasing rate of events k (association rates corresponding to arrival times t_a), we estimated the event rate k over multiple consecutive short intervals. The interval duration was 300 s for measurements using the optoplasmonic sensor and 80 s for measurements using DNA-PAINT.These measurement intervals are a practical compromise between obtaining good time resolution and good exponential fits for determining the average association rates in the 300s/80s measurement intervals. The association rates are obtained in these intervals by fitting single decaying exponentials to the time between consecutive arrivals t_a. The rates k are plotted on the time traces in Figure 6.3a (green circles with fit errors) and Figure 6.3b (blue circles with fit errors). We can clearly see that the association rates decrease consistently over time. The observed reduction in association rate for both platforms clearly suggests that, over time, the number of docking strands available for observing transient hybridization events is decreasing. According to previous literature[190, 182], this phenomenon is not observed when DNA-PAINT experiments are performed on biomolecules bound to glass / polystyrene substrates[97, 182].

We then study the relationship between change in the association rate with respect to the occurrence of detected step signals. Optoplasmonic sensing experiments were performed for both T22 and P1 DNA sets. In particular, 1 µM of ImT22*D and ImP1*D imager strands are used to observe the transient interaction. Figure 6.4 shows the typical time trace for wavelength change in the context of T22 and P1 DNA sets. In both time periods we observe two step signals, wherein we analysed the association rates before and after the step signals. The time intervals of detected step signals are marked in the grey region in Figure 6.4 and a zoomed-in view of the step signals (red trace) is shown in the inset images. The association rates for each interval is then plotted (green circles for T22 and blue for P1 sets). Obvious association rate drops after each step are shown in both T22 and P1 experiments. Especially for P1 experiments depicted in Figure 6.4b, one can clearly see that after two step signals, the association rate has decreased from $(1.0 \pm 0.1) \times 10^5 (\mathrm{M \cdot s})^{-1}$

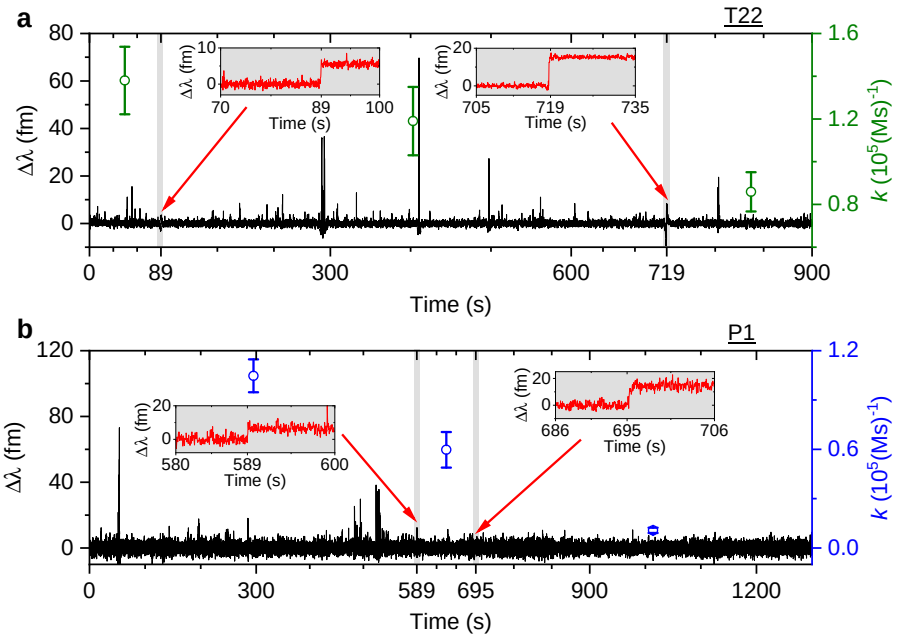

Figure 6.4: Example of detrended wavelength shift traces (black). An optoplasmonic sensing technique is applied to measure 1 µM of (a) ImT22*D and (b) ImP1*D imager strands. The grey shaded area displays the time period when a step signal is detected, a zoomed-in view of the step signals is shown in the inset images (red traces). The association rate is calculated for each section before and after the step signals (green circles for T22 and blue circles for P1 DNA sets).

to $(1.1 \pm 0.2) \times 10^4 (\mathrm{M \cdot s})^{-1}$. This observation indicates that the drop in anomalous DNA hybridisation rate is correlated to the step signals. As discussed above, a positive step signal refers to a binding event. There is no corresponding falling edge likely due to the imager strands irreversibly hybridised to the docking strands. This would then prohibit the docking strand from further interactions and hence result in a decreased association rate.

Imager Concentration Dependence for Prolonged Measurements

We next studied the concentration dependence of the arrival and dwell times by increasing the concentration of the imager strand, in 6 steps, for both techniques. The measurements at each concentration step were performed over 30 min. The dissociation rate k_{off} and the association rate k for the DNA strand P1 and its complementary imager are plotted in Figure 6.5a and Figure 6.5b for the optoplasmonic sensor and DNA-PAINT, respectively. The dissociation rates $k_{\mathrm{off}}^{\mathrm{OP}}$ for the optopalsmonic sensor and $k_{\mathrm{off}}^{\mathrm{PAINT}}$ for DNA-PAINT are estimated from a single- and bi-exponential fit to the survivor distribution of dwell times $t_{\mathrm{b}}^{\mathrm{OP}}$ and $t_{\mathrm{b}}^{\mathrm{PAINT}}$, respectively. The association rates k for both techniques are obtained from a single exponential fit to the survivor distribution of time between events t_{a}.

The plots show that the off-rates k_{off} provided by both techniques are relatively constant for all imager concentrations. The average off-rate estimated from the optoplasmonic measurements is $k_{\text{off}}^{\text{OP}} = 3.9 \pm 0.3\ \text{s}^{-1}$. For the DNA-PAINT measurements, the average off-rates estimates are $k_{\text{off},1}^{\text{PAINT}} = 3.3 \pm 0.7\ \text{s}^{-1}$ and $k_{\text{off},2}^{\text{PAINT}} = 0.2 \pm 0.1\ \text{s}^{-1}$. Here, the values of $k_{\text{off}}^{\text{OP}}$ and $k_{\text{off},1}^{\text{PAINT}}$ are within error and in line with previous work [16]. These rates thus correspond to the actual hybridisation dwell times of the P1 and imager strands. The rate $k_{\text{off},2}^{\text{PAINT}}$ likely corresponds to the average photobleaching time of the dye (DY782) of $5 \pm 0.5\,\text{s}$ under the experimental conditions.

On the other hand, the association rates k increase with higher imager concentrations. The increase in k for both techniques is not linear with imager concentration as would be expected for single-molecule interactions. The estimated k gradually saturates with increasing imager concentrations and even drops significantly, as is seen at 1000 nM for the optoplasmonic sensor and 60 nM for DNA-PAINT. This deviation from linearity may arise from an increased probability of docking strands being permanently occupied for higher imager concentrations. The drop of events rate k is occurring at different concentration, which is due to the different effective sensitivity among DNA-PAINT and optoplasmonic sensing. In the case of optoplasmonic sensing, the docking strands that provide signals are the ones located on the hotspots. The hotspots are distributed on the tip area of Au nanorods and are around 22% of the total surface area of an Au nanorod. Therefore, only up to 22% of the docking strands contribute signals in the optoplasmonic sensing setup. On the contrary, all the docking strands on the surface of Au nanorod contribute to DNA-PAINT signals. In addition to that, two different approaches show different signal-to-noise ratio, both of which provide the plausible picture for the discrepancies observed. More details of the observed discrepancy can be found in [16].

Control Measurements and Investigation of Potential Causes

The signals observed in both DNA-PAINT and optoplasmonic sensing imply an increasing number of unavailable docking strands over time. Based on the step signals, a natural hypothesis would be that permanent hybridisation block the docking strands within the time scale of the experiment. Alternatively, the docking strands could be cleaved due to hot electrons generated from the plasmonic nanorods. Control experiments are performed to discern the causes of the reduction in association rates over time.

In 2018, Sabrina *et al.*[193] demonstrated that a high-power pulsed laser could cleave $Au-S$ bonds on the surface of the GNRs, wherein the cleaved surface can be refunctionalised with different docking strands. There is, however, no evidence

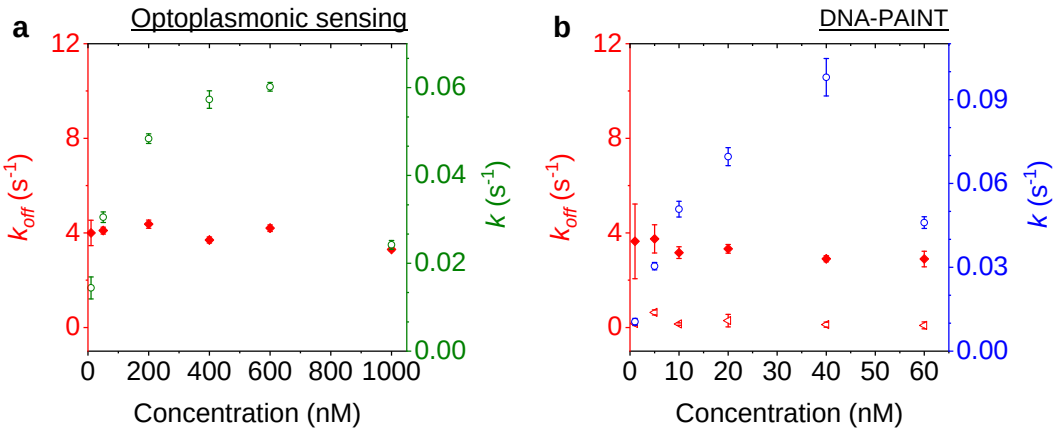

Figure 6.5: Kinetics characterised for a P1 DNA set. The experimental data is acquired with (a) the optoplasmonic sensor and (b) DNA-PAINT. Association rates are plotted for optoplasmonic data (green circles) and DNA-PAINT data (blue circles). Dissociation rates are extracted from fitting of single exponentials for optoplasmonic sensing (red dots in a) and biexponentials for DNA-PAINT (red dots and triangles in b). Both approaches are measured for 6 different imager strand concentrations and each concentration is measured over 30 min.

for the low intensities (32 W/cm^2) in our experiment causing the cleaving of $Au-S$ bonds. Nonetheless, to prove that the $Au-S$ bonds were intact, we performed control measurement using samples where the association rate already dropped to near zero. We washed the samples (i.e. coverslips immobilised with gold nanorods, functionalised with docking DNA and left to interact with imager strands for >6 hours) thrice with Milli-Q water to remove excess DNA. We then performed the protocols for immobilizing new thiolated docking DNA (See Materials and Methods) for 1 hour to fully saturate any available binding sites on the GNR (assuming laser cleaving of previously attached docking DNA). In the optoplasmonic sensing method, we do not observe any docking DNA binding steps in this process, indicating no available sites on the GNR surface (See Supplementary Figure S2a). Finally, we added 2 µM of imager DNA in the case of optoplasmonic sensing and 40 nM of imager strands in the case of DNA-PAINT measurements. As seen from the time traces obtained (See Supplementary Figure S2b, c), we observe no restoration of association rate from both platforms, indicating that new docking strands could not be immobilised. We hence conclude that there is no laser-induced cleaving of the initially functionalised docking DNA in our experiments. The Au-S bonds formation and dissociation is known to be an equilibrium process, however, we did not observe single-molecule signals associated with ligand exchange, indicating that any ligand exchange takes much longer than our measurement time of 45 min.

This additional control suggests that the observed anomalous hybridisation behaviour

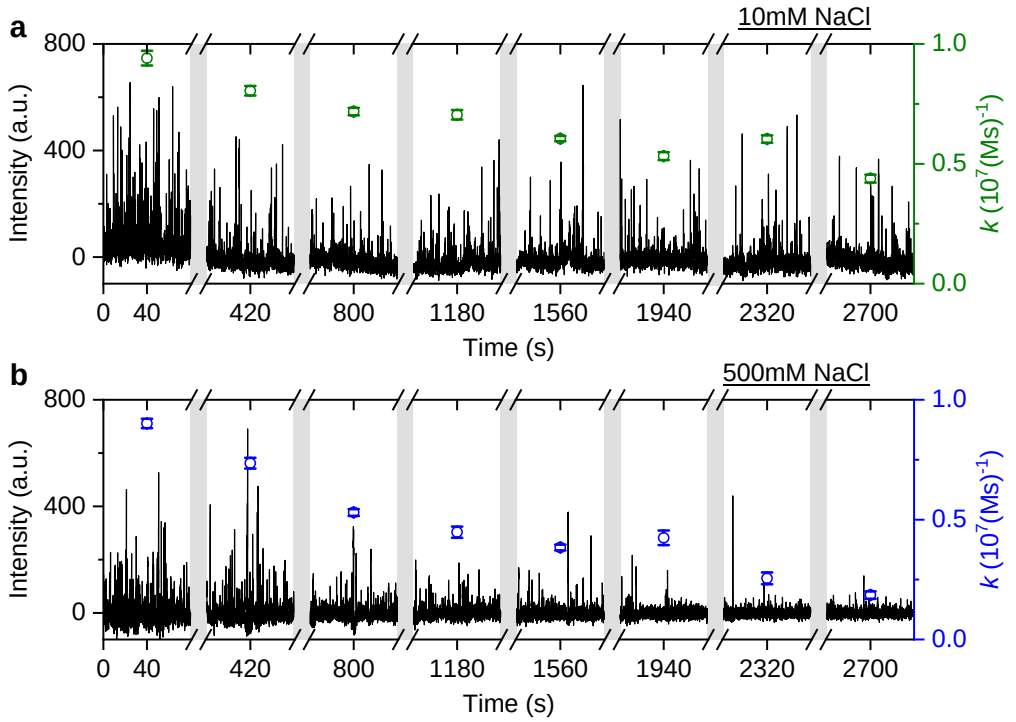

Figure 6.6: DNA-PAINT measurements with 40 nM ImP1*D. The experiment is conducted with (a) 10 mM NaCl HEPES buffer and (b) 500 mM NaCl HEPES buffer. The association rates are plotted accordingly, with green circles for 10 mM NaCl HEPES buffer and blue circles for 500 mM NaCl HEPES buffer.

cannot be explained by hot electron cleaving. Given the steps signals demonstrated in the optoplasmonic sensing experiments, we can conclude that the anomalous DNA hybridisation originated from the permanent hybridisation of imager strands. To further investigate the mechanism of this anomalous hybridisation, two sets of experiments are then carried out. The first set of experiments aims to explore the influence of different electrolyte concentrations, and the second utilises external heating to inspect whether the anomalously hybridised DNA melts at a higher temperature.

It is well known that adding electrolytes in a solution can affect the DNA melting temperature[194]. As we concluded the observed anomalous behaviour resulted from permanent hybridisation, it is expected that this will also depend on electrolyte concentration. To this end, we monitored the association rate change for different ionic strengths in the buffer solution. In particular, a solution with 40 nM ImP1*D imagers is used to conduct DNA-PAINT measurements under 10 mM and 500 mM NaCl concentrations in the buffer. Both experiments are carried out for over 45 min and the intensity time trace is plotted in Figure 6.6 (black trace). The association rate is calculated and plotted as green circles for 10 mM NaCl HEPES

buffer and blue circles for 500 mM NaCl HEPES buffer. To properly compare the rates decreasing under different NaCl concentrations, we selected GNRs that have similar starting association rates corresponding to the 10 mM and 500 mM NaCl concentrations. As shown in Figure 6.6, the association rate for the first 80 s is calculated to be $(9.4 \pm 0.3) \times 10^6 (\mathrm{M \cdot s})^{-1}$ for the 10 mM NaCl HEPES buffer and $(9.0 \pm 0.2) \times 10^6 (\mathrm{M \cdot s})^{-1}$ for the 500 mM NaCl HEPES buffer, respectively. In both time traces we observe a similar decrease in association rates. In the case of the 500 mM NaCl HEPES buffer, however, the association rate decreases much faster. After 45 min the remaining association rate for the 10 mM NaCl HEPES buffer is $(4.4 \pm 0.2) \times 10^6 (\mathrm{M \cdot s})^{-1}$, while for the 500 mM NaCl condition a much lower rate of $(1.8 \pm 0.2) \times 10^6 (\mathrm{M \cdot s})^{-1}$ is found. The observed phenomenon further matches the permanent hybridisation hypothesis. Higher ionic strength can be induced in the solution with increased NaCl concentration, which lowers the charge barrier and provides better accessibility for the docking strands. The permanent hybridisation process is thus accelerated due to increased hybridisation efficiency.

All experiments described above are conducted at $\sim$ 295 K room temperature. Given that plasmonic nanorods confine light to a nanoscale region, one would expect a higher temperature on the GNR surface than the surrounding host medium. The higher temperature on the GNR surface could potentially cause an equilibrium perturbation in DNA hybridisation. To estimate the temperature change caused by plasmonic heating, we calculated the temperature increase with a laser intensity of 80 $\mathrm{W/cm^2}$ - the maximum intensity delivered to the glass coverslip. According to simulations (Detailed in Supplementary Figure S3), the maximum GNR surface temperature is only increased by 0.1 K at the GNR absorption peak wavelength of 755 nm. Considering that a GNR is placed onto the surface of the glass coverslip under 785-nm TIRF excitation which exhibits a near-field enhancement factor of 5 (Supplementary Figure S1), the estimated temperature gradient near the GNR surface is not higher than 0.5 K with a laser intensity of 32 $\mathrm{W/cm^2}$. This temperature increase is too small to cause a significant change in the hybridisation equilibrium. In experiment, no restored rate is observed when increasing the laser illumination power from 32 $\mathrm{W/cm^2}$ to 80 $\mathrm{W/cm^2}$.

To examine the effect of temperature increase on the melting of anomalous DNA hybridization, we increased the temperature of the buffer solution externally (See Supplementary Figure S4). In this scenario, DNA-PAINT experiments are conducted under different temperature conditions. We again choose P1 DNA samples where the association rate already decreased to near zero, wherein the sample is acquired using the same protocol described above. The procedure is as below. First, the chamber is

filled with HEPES buffer heated to a temperature of $\sim$ 333 K for 30 min, to enable potential melting of double-stranded DNA. Then, the heated solution is removed and sample chamber is rinsed thrice to remove possibly unzipped imager strands. Finally, a HEPES buffer with 10mM NaCl and containing 40 nM of imager is added to the sample chamber to perform DNA-PAINT experiments.

Supplementary Figure S4a shows the DNA-PAINT signals obtained when measurements are performed in a buffer with 40 nM imager concentration heated to $\sim$ 333 K. At this higher temperature, the association rates of single-strand DNA are higher[173, 195]. Nonetheless, we do not observe many events showing that the association rates are not restored at this temperature. To exclude the possibility that the higher dissociation rate at 333 K is faster than our time-resolution for DNA-PAINT, we performed measurements in a room temperature buffer containing 40nM imager. As shown by the time traces in Supplementary Figure S4b, we observe no restoration of association rates. Similar experiments at a higher temperature of $\sim$ 353 K also show no restoration of association rates (Supplementary Figure S4c, d). These findings suggest that the anomalous hybridization of DNA attached to gold nanoparticles are irreversible and highly stable (up to $\sim$ 353 K).

6.4 Discussion

Here, we have established a hybrid platform (SIMOPS) capable of performing both fluorescence based single-molecule localization imaging (DNA-PAINT) and refractive index based optoplasmonic sensing. We have utilized this platform to study the anomalous hybridisation kinetics of short single-stranded DNA (ssDNA) oligomers attached to the surface of gold nanoparticles. The SIMOPS platform provides us with time traces of different signal types corresponding to the hybridization kinetics of ssDNA. Both DNA-PAINT and optoplasmonic sensing methods provide spike-like (duration of a few hundred milliseconds) and short plateau signals (duration of a few seconds) that are corresponding to the transient hybridisation of the ssDNA. The optoplasmonic sensor also provides positive step-like signals with no corresponding falling edge indicating permanent hybridization of the ssDNA. A single kinetic off-rate of $k_{\text{off}}^{\text{OP}} = 3.7 \pm 0.1$ s^{-1} is reported from the optoplasmonic sensing approach. DNA-PAINT on the other hand provides long plateau-like signals with both positive and negative steps separated by tens of seconds. We have shown that these signals likely correspond to the permanent hybridisation of the ssDNA and subsequent bleaching of the imagers. DNA-PAINT hence provides two kinetic off-rates with values ($k_{\text{off},1}^{\text{PAINT}} = 3.3 \pm 0.7$ s) and ($k_{\text{off},2}^{\text{PAINT}} = 0.2 \pm 0.1$ s). The magnitudes of $k_{\text{off}}^{\text{OP}}$ and $k_{\text{off},1}^{\text{PAINT}}$ are consistent with predictions for DNA melting temperature specific to the

oligonucleotides and buffer conditions[173] and with measurements performed using similar DNA sequences at room temperature without local plasmonic heating[88]. The magnitude of $k_{\mathrm{off},2}^{\mathrm{PAINT}}$ associated with photobleaching of the DY782 at the laser intensity of $\sim 32\mathrm{W}/\mathrm{cm}^2$ is comparable to that reported in the literature [196, 197]. Measurements of DNA hybridisation kinetics over a long time ($\sim$ 45 mins) show that the association rate gradually decreases with time as measured by both DNA-PAINT and the optoplasmonic techniques. We show that the decrease in association rate is correlated to the step-like signals observed via the optoplasmonic sensing, indicating a permanent occupation of 'docking' DNA strands attached to the GNR surface. We found that the association rate increased non-linearly with increasing imager concentration over prolonged time, which even decreased at very high imager concentrations. Our data demonstrates the decrease in association rate behaviour can be accelerated by increasing the ionic strength. These observation further bolstering the hypothesis of permanent hybridization of the 'docking' and 'imager' strands on the surface of the GNRs.

In control measurements we attach more 'docking' DNA to GNRs where the association rates dropped to near-zero, show that no new 'docking' could be attached to the GNRs. This observation is inconsistent with previous reports of hot electron-mediated cleavage of $Au-S$ bonds of the docking strands [193]. Additionally, we observe no falling (negative) step-like signals in the optoplasmonic sensor data also indicating that there is no hot-electron cleaving of the $Au-S$ bonds. Instead, our data and control measurements suggest a permanent hybridization of the 'docking' and 'imager' strands.

Further, control measurements with increasing the temperature of the buffer show that the anomalous DNA hybridization is stable up to at least $\sim$ 353 K. One possible explanation for anomalous permanent hybridisation of DNA strands to complementary strands on plasmonic gold nanoparticles is DNA inter-strand cross-linking. [198] The DNA inter-strand cross-links could be caused by the oxidative chemical environment found at/near the plasmonic hotspots of the gold nanoparticles, i.e. the sites of DNA hybridisation at which single-molecule signals are generated. More specifically, singlet oxygen and radical oxygen species could be locally generated by the light-metal interaction [199]. Various other photochemical processes could result in DNA mutations leading to anomalous permanent hybridisation events. Further researches with different DNA sequences are needed to fully understand the mechanism.

No such anomalous hybridisation signals, with prolonged dwell times that lie well outside of the expected dwell time distributions for these oligonucleotides, have

been reported before[200]. Our observations contradict the prediction of well-established theoretical models that consider the thermodynamics of base-pairing interactions of DNA nucleotides[201, 202, 203]. The anomalous hybridisation events reported here have not been detected before because established single-molecule techniques, such as those that use fluorescently-labelled oligomers, have been unable to track permanent hybridisation events over prolonged times due to photobleaching. The surface plasmon resonance (SPR) based sensors do not show single-molecule sensitivity. They are only capable of observing wavelength shift by bulk loading, while not able to detect transient DNA hybridization events. It would be difficult to observe the anomalous hybridization events without a single-molecule technique. The proposed SIMOPS single-molecule platform is capable of discerning transient from permanent interactions of short oligonucleotides (i.e. localised on the plasmonic nanoparticles) over measurement times of up to several hours. Our dual DNA-PAINT and optoplasmonic sensing platform will enable further detailed investigations of DNA mutations in real-time and at the single-molecule level. This technique paves the way to real-time observation of same single-molecule events with two techniques to obtain more information on single-molecule processes such as anomalous DNA hybridization. The SIMOPS could be further used for single-molecule experiments that reveal the occurrence of specific mutations. Such studies can differentiate the types of mutation and their respective kinetics with the use of proteins that selectively bind to specific mutations on a DNA strand.

Our observations have implications for the use of localised plasmon resonance-based DNA sensors which affect the DNA interaction kinetics. Consequently, permanent DNA hybridisation results from prolonged light exposure at moderate light intensities. In single-molecule studies, as was shown here, such permanent hybridisation effects have to be carefully taken into account when interpreting single-molecule measurements. The study of the origin of anomalous DNA hybridisation signals can provide novel insights into the chemistry and photochemistry of DNA on plasmonic nanoparticle surfaces. Such studies can uncover yet-undetected pathways for introducing DNA mutations by interaction with light. Our studies also have implications for light-based in vivo therapies that use plasmonic nanoparticles, e.g. damage to tumour cells in the context of cancer treatments. In addition, recent studies have shown that DNA can work as a conductive material and transfer hot carriers generated along the plasmonic nanoparticles, our platform is, therefore, ideal to study DNA hot electron charge transfer reaction and potential cause of DNA interstrand crosslinking at a single-molecule level[204, 198, 205, 206].

6.5 Materials and methods

Materials

GNRs with an average diameter of 10 nm and length of 35 nm (i.e. longitudinal plasmon resonance at $\lambda \approx 750$ nm) were purchased from Nanopartz Inc.(A12-10-CTAB-750). All DNA oligos were purchased from Eurofins Genomics and their sequences are listed in Table 1. Glass coverslips with a refractive index of n $\approx$ 1.52, with an aspect ratio of 22 mm $\times$ 22 mm and a thickness of 170 $\pm$ 5 µm, were purchased from Thorlabs (Precision Glass Cover Slips, CG15CH). High-Q glass microspheres (n$\approx$ 1.45) were fabricated with a 30 W CO_2 continuous wave laser ($\lambda \approx 10.6$ µm) purchased from Synrad 48-2, Novanta Inc., WA, USA. PLL-g-PEG was purchased from SuSOS Surface Technology, Switzerland. Tris(carboxyethyl)phosphine hydrochloride (TCEP) was purchased from Sigma-Aldrich (Catalog Number 646547). 4-(2-hydroxyethyl)-1-piperazineethanesulfonic acid (HEPES) was purchased from Sigma Aldrich, and a 20 mM HEPES buffer with pH$\approx$7 was prepared for use as the interaction buffer. All chemicals for the buffers were purchased from Sigma Aldrich.

Table 6.1: Sequences of ssDNA used for the experiments.

	ssDNA	**Sequence (5'-3')**
Set I	P1	[ThiolC6] TTT TAT ACA TCT A
	ImP1*D	[DY782] CTA GAT GTA T
Set II	T22	[ThiolC6] TTT TGA GAT AAA CGA GAA GGA TTG AT
	ImT22*D	[DY782] ATC AGT CCT TTT CCT TTA TCT C (3 mismatched)

SIMOPS Setup Optics

Figure 1 provides the schematic of the SIMOPS setup. In order to couple light into WGMs with an objective lens, a fiber-coupled tunable laser diode with nominal wavelength of 780 nm (DL pro, Toptica) was collimated with a fiber collimator and then expanded by a beam expander (L1 and L2), resulting in a collimated beam diameter of 17.3 mm. A half-wave plate (HWP1) and a polarizing beam splitter (PBS; Tp:Ts $>$ 3000:1) were used to control the intensity of the p-polarised transmitted beam. An additional half-wave plate (HWP2) was placed behind the PBS to alter the polarisation state of the transmitted beam while maintaining the intensity. The polarised beam was then focused by a lens (L3) with a focal length of 200 mm onto the back focal plane (BFP) of an oil-immersion TIRF objective (CFI Apo TIRF 100X, 1.49 NA, Nikon) through a non-polarising beam splitter (BS). The accurate

positioning of the focused spot onto the BFP in the radial direction (x) was achieved with a z-axis motorised translation stage, leading to a collimated beam emerging from the objective at an incident angle (θ_i) proportional to the radial displacement of the focused spot from the optical axis of the objective. The incident collimated beam in the glass coverslip is totally reflected while producing an evanescent field at the glass-water interface (See Supplementary Figure S1). A custom-built coverslip chamber (See inset of Figure 6.1) was designed to hold two 22-mm coverslips with a 5-mm gap between them. Such water spacing is wide enough for injecting medium and placing the glass microsphere near the surface of the coverslip. The reflected spot at the BFP was projected onto a plane conjugate to BFP of the TIRF objective through a Bertrand lens (L4) and a tube lens (L5) with focal lengths of 150 mm and 200 mm, respectively. A pinhole was placed at the conjugate plane to remove unwanted stray light and increase the signal-to-noise ratio. The spatially filtered beam that contains optoplasmonic signals was subsequently collimated and focused onto an amplified photodiode (PD) by relay lenses (L6 and L7). For fluorescence detection, both switchable mirror (SM) and L4 were replaced by an emission filter to allow quick alteration between optoplasmonic sensing and TIRF imaging. Fluorescence images were recorded by a back-illuminated EMCCD camera (iXon Ultra 888, Andor). The laser intensity hitting the coverslip was $\approx$32 W/cm^2.

Experimental protocols

In this work, we used two sets of DNA oligos (See Table 1 for sequences): (i) a 10-mer docking strand termed P1 and corresponding imager termed ImP1*D, and (ii) a 22-mer docking strand termed T22 and corresponding imager strand ImT22*D. The experimental procedure for both DNA-PAINT and optoplasmonic sensing are similar and consist of 3 main steps. First, gold nanorods were deposited onto a glass surface (either a coverslip in the case of DNA-PAINT, or microsphere resonator surface in the case of the optoplasmonic sensor) in an acidic aqueous suspension (pH $\approx$ 1.6, 1 pM GNRs) for 15 min. The sample chamber was then washed thrice to remove unbound GNRs. For DNA-PAINT, a clean coverslip was prefunctionalised with PLL-g-PEG (Su-Sos) to prevent nonspecific binding between the fluorophore and the coverslip. During the deposition of GNRs, clear binding step signals were observed via the optoplasmonic sensing approach (See Supplementary Information Figure S5b). As for the DNA-PAINT approach, the location of GNRs could be visualised by the EMCCD camera owing to their photoluminescence. Second, the docking strands were immobilized onto the GNRs through a mercaptohexyl linker at their 5' end. The P1 docking strands were immobilised in a citrate buffer at pH

≈ 3 with 1 mM NaCl. The T22 docking strands were immobilised in 0.02% wt/wt sodiumdodecylsulfate (SDS) solution at pH ≈ 3. Before adding the docking strands into the sample chamber, they were pre-mixed with a solution containing a reducing agent (10 µL of 10 mM TCEP) to cleave the disulfide bonds and therefore enable efficient binding of the thiols to the GNRs. The docking strands were then injected into the sample chamber to reach a final concentration of 1 µM and left to incubate for 30 min. Since the docking strands do not contain any fluorescent labels, the binding of the docking strands to the GNRs were not monitored via DNA-PAINT. In contrast, in the optoplasmonic sensor, step-like signals were observed upon binding of the docking strands to GNRs (See Supplementary Information Figure S6a). It is important to note here that only a subset of all docking strands attached to the GNRs provided step signals due to the variability in plasmonic enhancements at each binding site.[16] Finally, the transient interactions between the docking and imager strands were monitored using both techniques. The chamber was washed three times to remove excess docking strands, and corresponding labelled imager strands were added to the sample chamber in an aqueous solution of 20 mM HEPES buffer at pH ≈ 7, with two different NaCl concentrations of 10 mM and 500 mM, respectively. All experiments were conducted at room temperature of around 295.7 K.

Single-Molecule Localisation Imaging via DNA-PAINT

Fluorescence imaging was carried out on the dual sensing and imaging platform, with an effective pixel size of 130 nm. For DNA-PAINT measurements, 2000 frames per image were recorded at a frame rate of 25 Hz. The EMCCD readout rate was set to 30 MHz at 16-bit resolution and a pre-amplifier gain of 2. The electron multiplier gain was set to 750. Utilising the single-molecule localisation microscopy add-in (ThunderSTORM[192]) in Fiji (ImageJ), one can obtain the intensity time traces for single-molecule localisation on the GNRs. The image filtering was performed via Wavelet filter (B-Spline), where B-Spline order was set to 3 and scale to 2. The approximate localisation of molecules has been carried out via local maximum method, with 8-connected neighbourhoods and a peak intensity threshold set to the standard deviation of the 1st wavelet level. The sub-pixel localisation was achieved from point spread function estimation via integrated Gaussian fitting. The fitting radius was set to 3 pixels and the initial sigma set to 1.6 pixels.

Optoplasmonic Sensing of DNA Hybridisation

The mechanism of WGM based optoplasmonic sensing is as follows. Optical WGMs are excited in a glass microsphere resonator by coupling the evanescent wave

emerging from the surface of the glass coverslip. The external cavity laser is then scanned over a small bandwidth around the WGM resonance to record the resonance spectra as shown in the inset of Figure 6.1d. Plasmonic nanorods are then attached to the surface of the WGM resonator using the protocols described above and their plasmon resonance is excited by the WGM. When molecules approach the near field of the GNRs, shifts in the resonance of the WGM are produced due to a local change in refractive index (the molecule is essentially polarised by the electric field which in turn causes a shift in wavelength $\Delta\lambda$) as shown by the red trace in the inset of Figure 6.1d. By tracking the shift in resonance wavelength ($\Delta\lambda$) and the linewidth (Δ FWHM, $\Delta\kappa$), we can monitor real-time single-molecule interactions at/near the hotspots of GNRs. To extract $\Delta\lambda$ and $\Delta\kappa$ from the resonance spectra, a centroid fitting algorithm is applied. Custom MATLAB code was employed to detect peaks, remove background trends (i.e. detrending), and estimate event rates. A threshold of 3σ is applied for signal detection. [17]

Acknowledgments

N.E. acknowledges funding from EPSRC Centre for Doctoral Training (CDT) in Metamaterials (XM2) (EP/L015331/1). N.E., H.-Y.W., S.S. and F.V. acknowledge funding from EPSRC EP/T002875/1.

author contribution

N.E conceived the idea, performed the experiments, and analysed data. H.-Y.W. conceived the original idea of TIRF-based excitation of the WGMs, designed and developed the optical setup, performed the numerical simulations, and contributed to figure plotting. N.E. and S.S. wrote the manuscript. S.S. guided the experiments and wrote the MATLAB scripts for analysis of optoplasmonic sensor data. S.V. trained N.E. in conducting optoplasmonic sensing experiments and helped with manuscript writing. F.V. supervised the project. All authors commented on the manuscript.

Supporting Information Available:

The Supporting Information is available free of charge at:
Principle of TIRF-Based Excitation of the WGMs; Control Measurements by Re-functionalising the Docking Strands; Simulation of Plasmonic Heating; Control Measurements by External Heating; Background Measurements of DNA-PAINT and Optoplasmonic Sensing Systems; Visualising Real-Time DNA Interactions via Optoplasmonic Sensing; Example of Single-Molecule Localisation

Data availability

The data that support the findings of this study are available from the corresponding author upon reasonable request.

conflict of Interest

Authors declare no conflict of interests.

Chapter 7

Conclusions and outlook

Single-molecule techniques are remarkable approaches to studying the nanoworld and fundamental bio-processes. While only using one specific technique to observe molecular biology activity is limited, multiple techniques should be employed to fully understand the single molecule behaviour.

We first show the comparison between the DNA-PAINT fluorescence super-resolution technique and optoplamsonic sensing, and we report a comparable result in terms of off rate, which builds up the equivalence between the two approaches.

We further developed a setup (SIMOPS) that combines both functions, our SIMOPS results reveal the cause of anomalous DNA hybridization. Unexpectedly, and contrary to previous hypotheses, we find that permanent DNA hybridization events are the cause for the decrease in DNA interaction kinetics. We find that stochastic permanent hybridization events accumulate over time. We believe that our SIMOPS results are of great importance because they reveal, and point to, novel physicochemical mechanisms that result in the stabilisation of DNA hybridisation on optically excited plasmonic nanoparticles.

In this thesis, the recent advances in single-molecule detection are listed. The technology in single-molecule biophysics has exceeded the limits of groundbreaking technologies in structural biology and physiology. The trajectory towards a method that can present precise information about a single molecule but still retain the function of the biological process being studied is clear. Future challenges come from both engineering and human creativity. For example, these emerging technologies

can do a lot of things, but the key may be to focus on really transforming these into meaningful research.

Appendix A

Supplementary information for chapter 6

A.1 Principle of TIRF-Based Excitation of the WGMs

We proposed a new approach to excite whispering-gallery modes (WGMs) using a commercially available total internal reflection fluorescence (TIRF) objective, as shown in Figure A.1a. It is important to understand the near-field distribution and field enhancement at the interface between the superstrate medium (water) and glass substrate when a beam of light is launched from glass to water. Figure A.1b shows the simulated and analytical reflectance spectra for p- and s-polarised illuminations (λ = 785 nm) as a function of the angle of incidence (ϑi). Total internal reflection (TIR) occurs when ϑi is equal to or greater than the critical angle (ϑc), which is 61.4° for both p-polarised and s-polarised beams. The corresponding enhancement distributions of the near-field intensity in the surface normal (z) direction, in response to p- and s-polarised incidences, are shown as a function of ϑi in Figure A.1c and d, respectively. As ϑi approaches ϑc, the evanescent field is generated at the water-glass interface with a penetration depth rapidly decreasing with increasing ϑi, wherein the maximum field enhancement is about 5.14 times for p-polarised illumination. For the p-polarised incidence, the continuity of the displacement field across boundaries requires that the normal electric field (Ez) be higher in the lower index material,

such that the field enhancement in the water medium immediately adjacent to the interface is greater than that produced in the s-polarised case. Since the refractive index of a glass microsphere is higher than that of water, causing the local effective refractive index to be slightly higher than the background refractive index (n=1.33), the coupling angle at which WGMs are evanescently excited is usually slightly larger than the calculated ϑc.

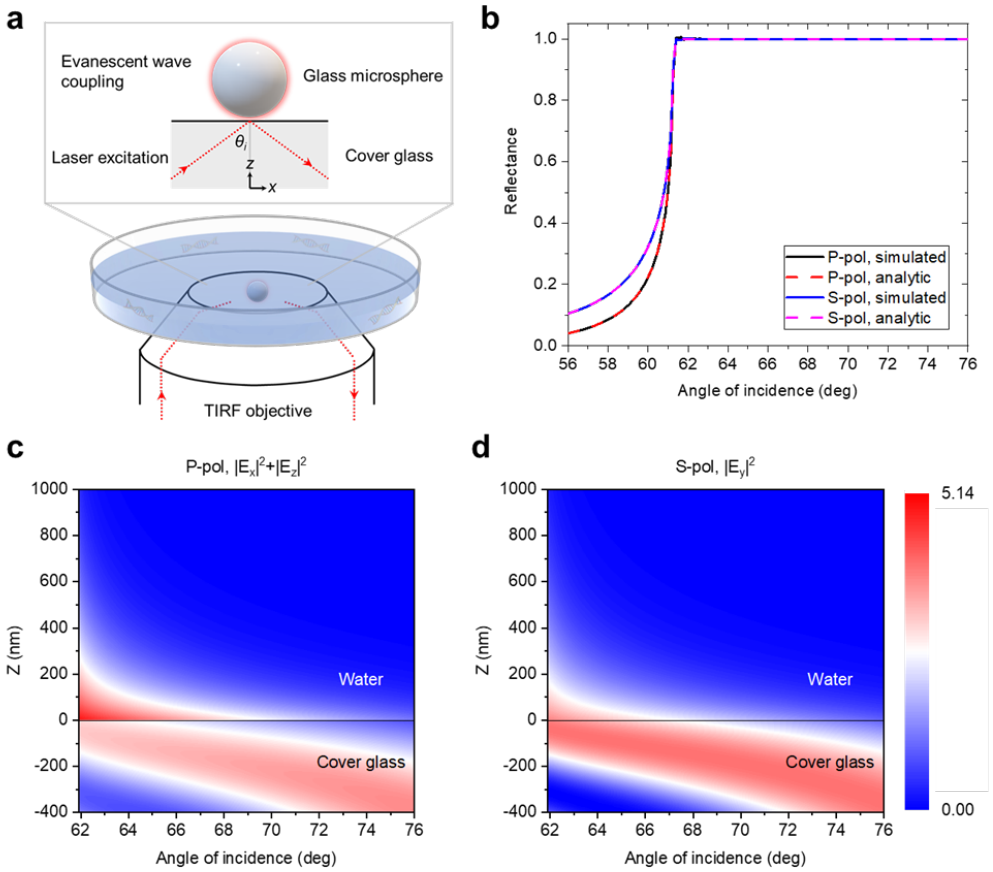

Figure A.1: Principle of TIRF-based excitation of the WGMs. (a) Schematic of the objective-based excitation of whispering-gallery modes (WGMs). (b) Simulated and analytical reflectance spectra for a p- and s-polarised plane wave incident on the water-glass interface from the glass side. (c) and (d) are the corresponding enhancement distributions of the near-field intensity in the surface normal direction for p- and s-polarised illuminations. The color bar on the right side is scaled by the normalisation of the local electric field intensity ($|E|^2$) to the incident electric field intensity ($|Einc|^2$).

.

A.2 Control Measurements by Refunctionalising the Docking Strands

To verify whether the observed anomalous behavior was a result of hot electron cleaving of Au-S bonds, we conducted control experiments through the following procedure:

1) We fabricated the samples (microsphere/coverslip) and immobilised GNRs on the glass surface. GNRs were functionalised with docking DNA and left to interact with imager strands for more than 6 hours.

2) We removed the solution in the chamber cell and rinsed with milliQ water three times, then added the docking DNA with pH≈3 citrate buffer to the chamber. Docking strands were left in the chamber for over 2 hours to fully saturate the surface.

3) We rinsed the chamber three times and added pH≈7 HEPES buffer with 10 mM NaCl to conduct DNA-PAINT measurements. This experiment was carried out using both optoplasmonic sensing and DNA-PAINT techniques.

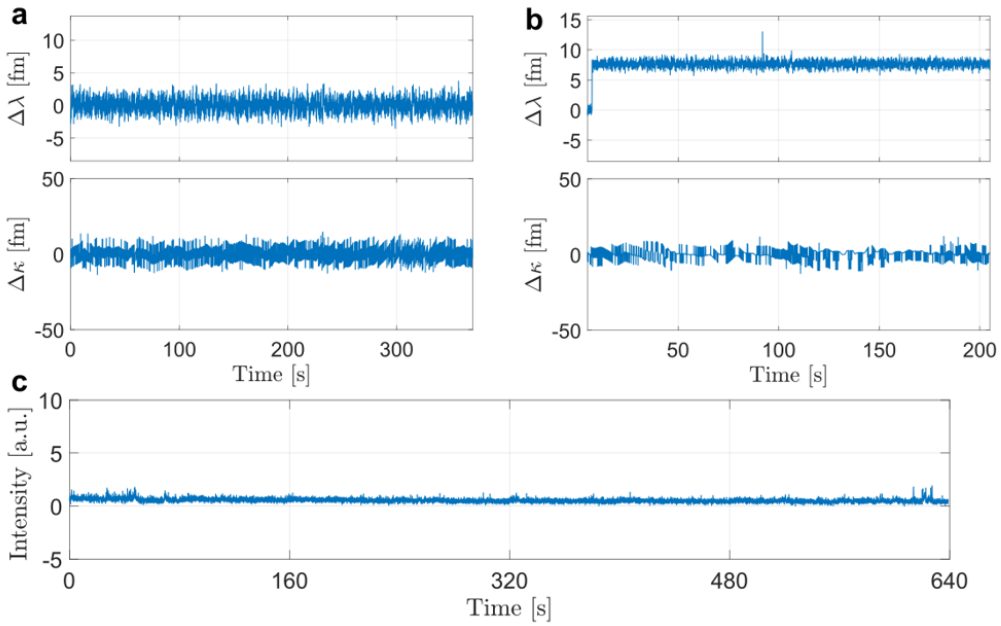

Figure A.2: Control measurements for refunctionalisation of T22 docking strands. (a) Refunctionalisation trace for a T22 docking strand monitored via the optoplasmonic sensor. (b) DNA hybridisation trace after T22 refunctionalisation, with the presence of 2 µM ImT22* monitored via the optoplasmonic sensor. (c) DNA-PAINT intensity trace on top of the GNR, lacking rate restoration.

.

As reported previously [17], step signals appear on $\Delta\lambda$ traces in the process of docking DNA binding on bare GNRs. We do not, however, observe any step signal within this refunctionalisation process. Figure A.2a shows an example trace where the $\Delta\lambda$(t) response is flat, indicating that the surface is not vacant and instead fully saturated by docking strands. No refunctionalising takes place here on the GNR surfaces. This finding is contrary to Sabrina et al. hot electron cleaving experimental results[193]. During imager strand interactions, we were only able to observe a binding step signal and 1 spike signal afterwards, with no signals for the remaining 30 min. This suggests that the event rate was not restored. The same protocol is applied to the DNA-PAINT experiments and as expected, no restored rate was found.

A.3 Simulation of Plasmonic Heating

COMSOL Multiphysics is used to calculate the absorption and scattering cross sections of a GNR in water and the results coincide with the vendor's datasheet. Absorption and scattering cross sections are defined as $C_{abs} = \frac{W_{abs}}{(I_{inc}A)}$ and $C_{sca} = \frac{W_{sca}}{(I_{inc}A)}$, where I_{inc} is the intensity of the incident field (79.58 W/cm^2), A is the cross-sectional area of the nanorod, and W_{abs} and W_{sca} are respectively the net energy dissipated by the absorbing GNR and scattered across an imaginary spherical surface centered on the GNR. Owing to its symmetry, only one quarter of the GNR is modeled. Photothermal heating (T) is solved via the heat transfer model $\nabla \cdot$ (-K∇T)=Q, where K is the thermal conductivity, ∇T is the spatial temperature gradient, and Q is the heat source that accounts for power dissipation density due to the light absorption by the GNR. The simulation results show that the maximum temperature change of 0.1K occurs at the absorption peak wavelength of 755 nm under the condition of plane wave incidence in a water host medium. Considering that in reality the GNR is placed onto the surface of the coverslip where TIRF excitation offers the maximum near-field enhancement of a factor of 5 at λ = 785 nm (as shown in Figure A.1), the estimated temperature gradient near the surface of the GNR won't be higher than 0.5K.

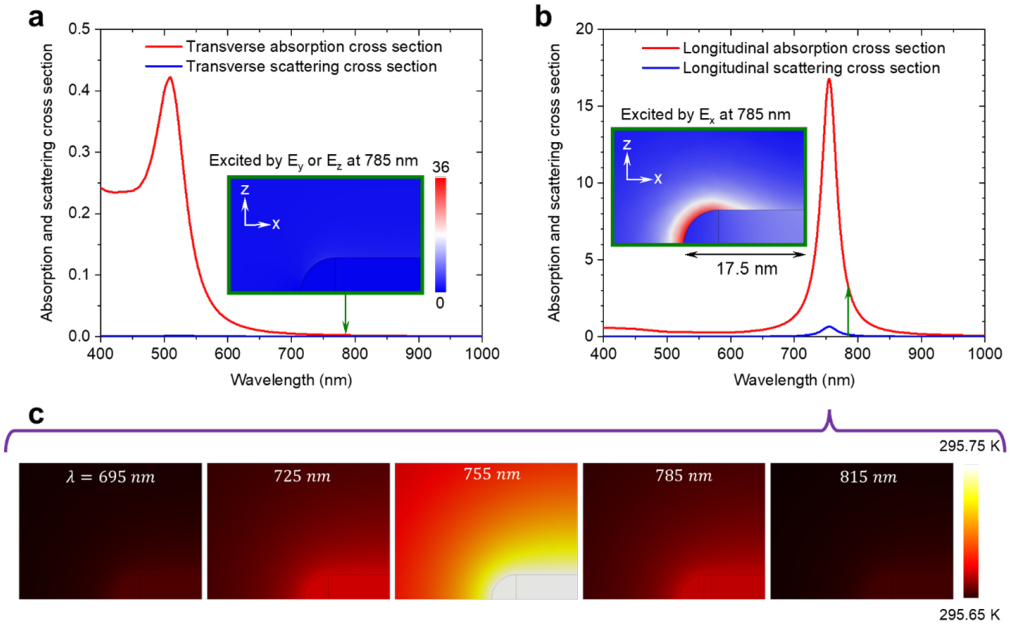

Figure A.3: Cross sections and photothermal effects of a gold nanorod in water. Absorption and scattering cross sections of a gold nanorod with a diameter of 10 nm and a length of 35 nm for an incident plane wave propagating along the positive z-direction. The electric field is aligned with (a) the minor and (b) major axes of the nanorod. Insets show the corresponding enhancement distributions of the near-field intensity at the laser excitation wavelength (λ=785 nm). Owing to its symmetry, only one quarter of the nanorod is modeled. The color bar is scaled by normalisation of the local electric field intensity ($|E|2$) to the incident electric field intensity ($|Einc|2$). (c) Wavelength-dependent temperature distribution maps associated with the dissipative losses of absorption in the nanorod (b). The maximum temperature difference of 0.1 K occurs at the absorption peak wavelength of 755 nm.

.

A.4 Control Measurements by External Heating

The heating experiments are carried out as follows: A hotplate is used to heat a beaker that is filled with milliQ water. 20mM HEPES buffer with NaCl solution is mixed with and without 40nM imager strands IMP1* in different Eppendorfs separately, all of them are immersed in the beaker. A thermometer is inserted into the beaker to characterise the temperature. We use the coverslip sample acquired using the protocol described in Supplementary 2. Before doing the experiments, HEPES buffer with 10mM NaCl is used to rinse the chamber 10 times, each time last for 3minutes. This process is to make sure the temperature of the chamber is constant and to avoid heat loss. Thereby the DNAs on the surface of GNRs are heated to the target temperature (60°C and 80°C). We then conducted two sets of DNA-PAINT

experiments, one is carried out under high temperature (60°C and 80°C), the other is using plain buffer to heat to target temperature (60°C and 80°C), and then cooled down to room temperature to conduct DNA-PAINT measurements:

1) DNA-PAINT at high temperatures are conducted by adding the 40nM imagers into the chamber, and measured for 60 and 80°C respectively, the results are shown in Figure A.4a, c.

2) Cooled to room temperature DNA-PAINT experiments are carried out using the sample described in 2), instead of doing experiments at a high temperature. We heated the chamber using plain buffer, cooled until room temperature and then conduct DNA-PAINT experiments, results shown in Figure A.4b, d.

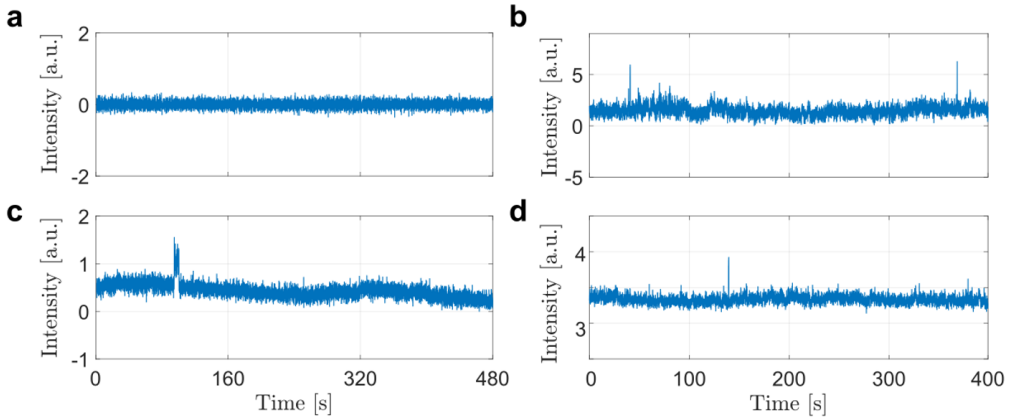

Figure A.4: Control measurement with external heating. The intensity time trace shows the DNA-PAINT experiment with 40 nM ImP1*D in (a) 60 °C HEPES buffer, then (c) 80°C HEPES buffer. (b) Heated to 60 °C then cooled to 22.5 °C, and (d), Heated to 80 °C then cooled to 22.5°C.

.

A.5 Background Measurements of DNA-PAINT and Optoplasmonic Sensing Systems

The background noise for the optoplasmonic sensing platform is measured after the assembly of the microsphere and GNRs. The average noise is around 2 fm (See Figure A.5a). Since the optoplasmonic sensing platform is sensitive to pressure and temperature changes, there would normally be a background trend. We remove this contribution via in-house MATLAB software[186]. The assembly of

the optoplasmonic sensor requires coupling between resonant GNRs and the WGM microsphere. GNRs could trigger an irreversible absorption reaction in the $pH \approx 1.6$ acidic solution, and this process can be real-time monitored by tracking $\Delta\,\lambda$ and Δ FWHM traces. Figure A.5b shows typical step signals acquired from the GNR binding process. We observe step signals in both $\Delta\,\lambda$ and Δ FWHM traces. Figure A.5c shows the background noise level of the DNA-PAINT technique. When the GNRs are bound to the coverslip surface (with the binding protocol as described above), photoluminescence signals can be seen from the camera. The intensity of a 5×5 ROI corresponding to the GNR location can then be tracked, with Figure A.5d showing a typical intensity time trace for that GNR.

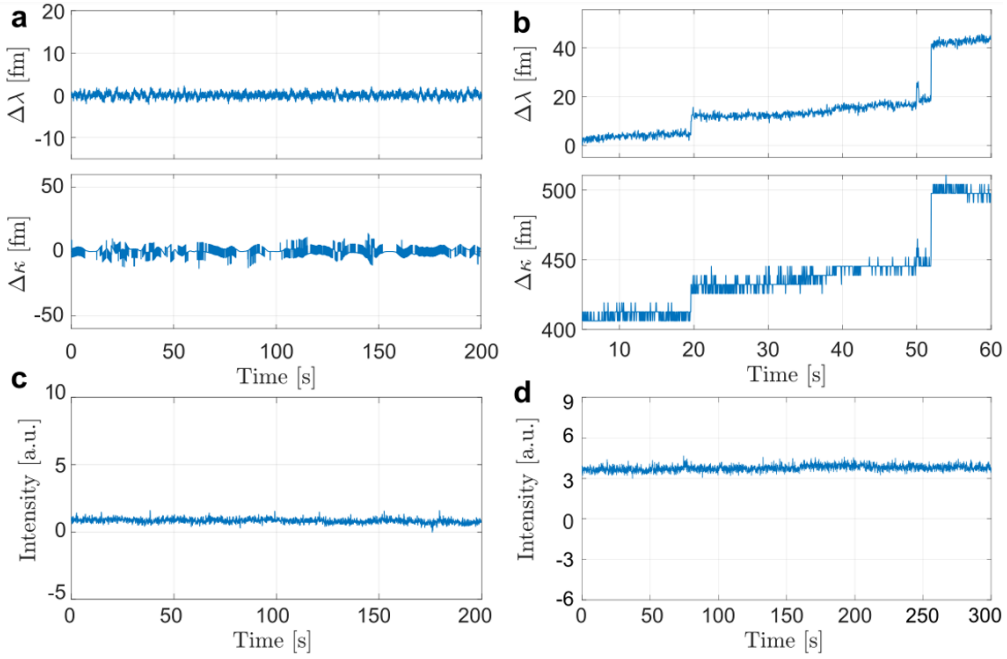

Figure A.5: (a) Detrended background noise for optoplasmonic sensing. (b) Real-time binding of GNRs. (c) Background noise for DNA-PAINT in a 5×5 ROI. (d) Intensity trace for a GNR positioned within the 5×5 ROI.

.

A.6 Visualising Real-Time DNA Interactions via Optoplasmonic Sensing

In the binding of docking DNA procedure, steps signals can be detected in the $\Delta\lambda$ trace. The positive shift is a result of the change in polarisability/refractive index

when immobilising docking stands to the GNR surface. There is, however, no corresponding change in the case of the ΔFWHM trace. Different from the observation of the GNR binding signals, where a large change in both Δλ and ΔFWHM traces exists, single-molecule experiments only exhibit signals pre-dominantly in the Δλ trace (i.e. ΔFWHM remains unchanged).

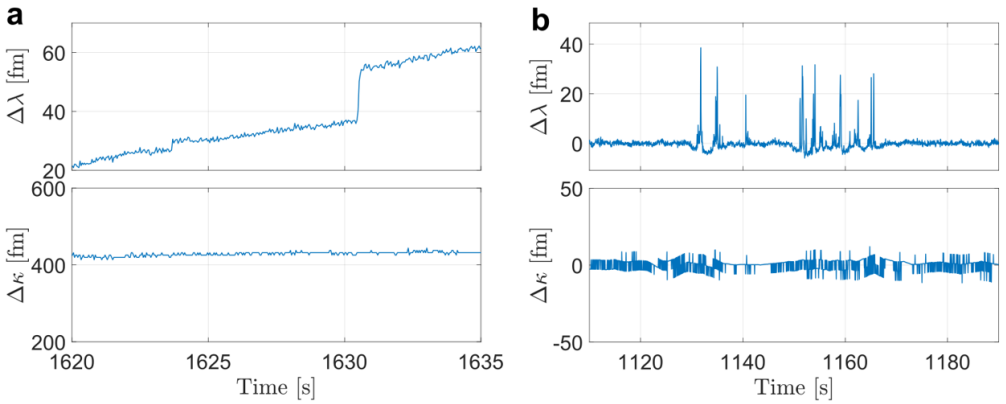

Figure A.6: Typical optoplasmonic sensing trace for (a) docking DNA binding to a GNR and (b) transient DNA interactions between docking and imager strands.

.

Figure A.6b shows an example of a transient DNA interactions trace, where no ΔFWHM is observed while only spike-like signals emerge.

A.7 Example of Single-Molecule Localisation

Figure A.7a shows a single frame of a DNA-PAINT image at the GNR position, where a single-molecule localisation microscopy algorithm named ThunderSTORM [192] is applied to estimate the sub-pixel location of the single molecule. Figure A.7b is an intensity time trace acquired from a 5×5 ROI (yellow box in Figure A.7a), and the signal marked by the red star corresponds to the crosshair mark in Figure A.7a. By stacking these locations one can eventually reconstruct super-resolution images of the GNR geometry.

A.8 Spike events extraction and analysis

The spike events are extracted from both intensity (DNA-PAINT) and wavelength shift (optoplasmonic sensing) traces with similar protocol. In the case of optoplam-

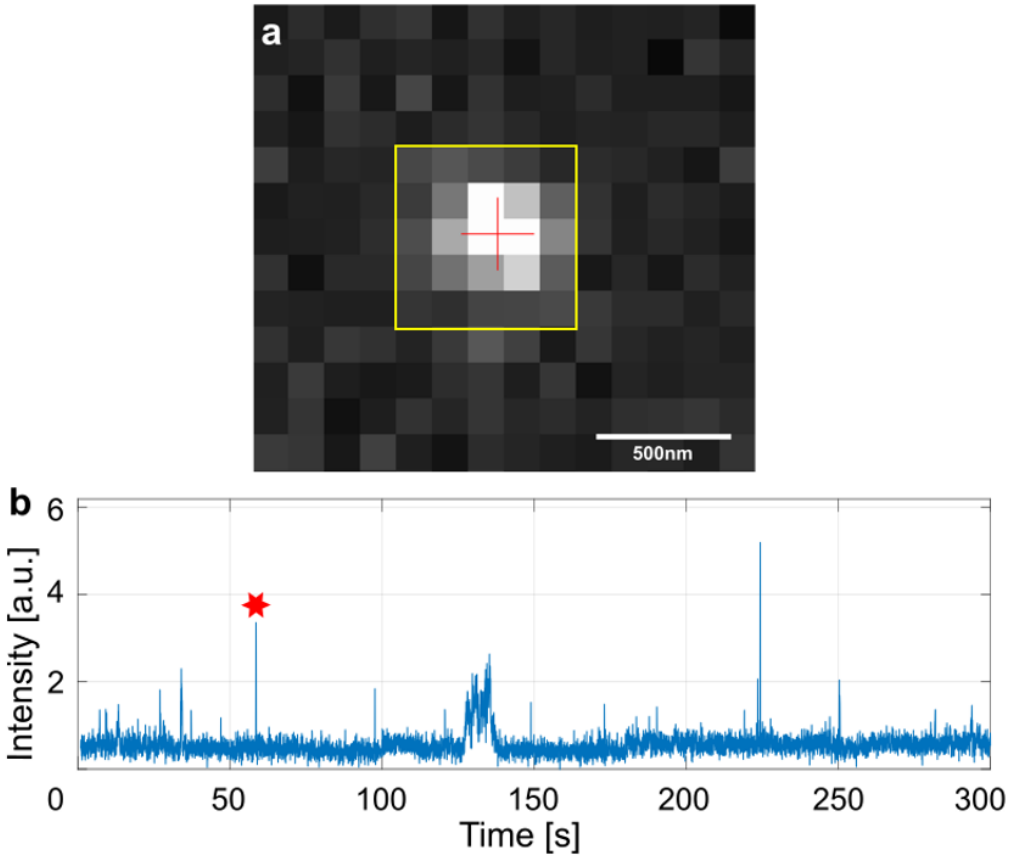

Figure A.7: Individual frame of a DNA-PAINT image on top of a single GNR, where (a) shows the localisation of the transient interaction corresponding to (b) the red starred time point in the trace.

.

onic sensing, there is normally a non-constant background signal, originating from a long-term drift caused by comparably slow changes of environmental attributes like pressure and temperature. While for DNA-PAINT the background signals are generally flat. Figure A.8a shows an example of optoplasmonic sensing data trace with a background. The first step is to remove the background trending using custom MATLAB code[186]. Figure A.8b shows the detrended trace. The standard deviation σ is ¬taken over the background intervals of this trace, where we then use a threshold of 4σ to extract the spike events. Figure A.8c shows the spike events detected after applying a threshold filter.

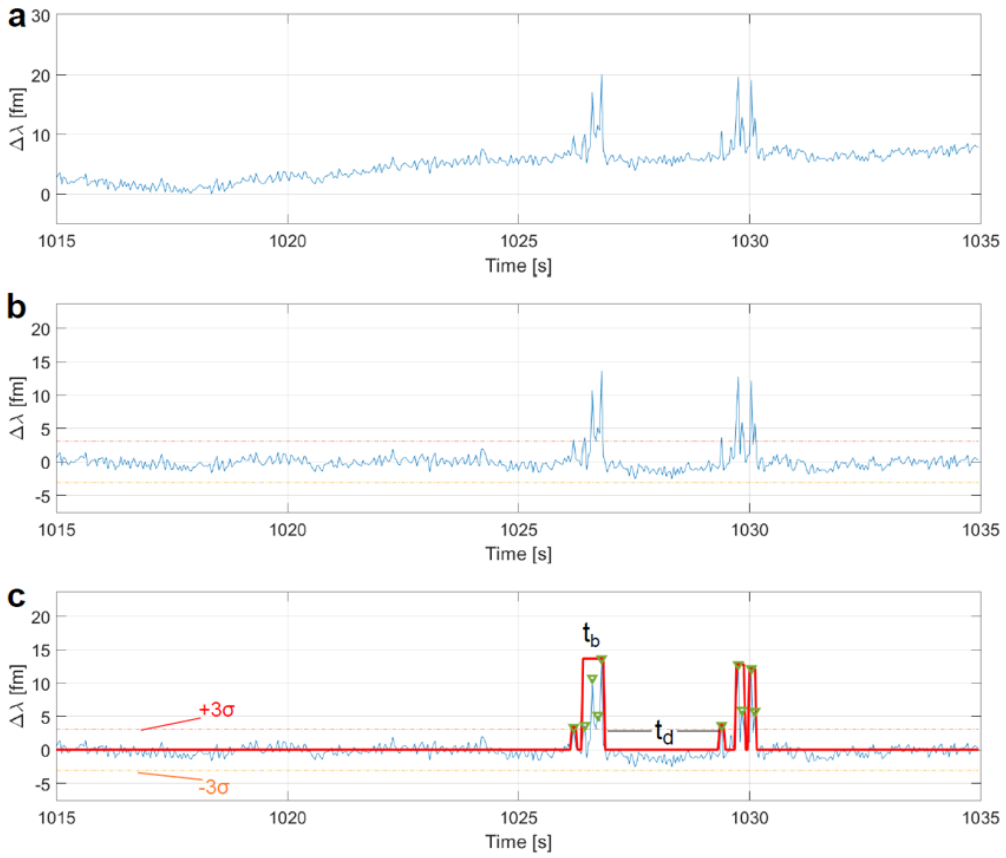

Figure A.8: Illustration of the spike extraction process. (a) Original background data trace. (b) Background-free data trace acquired with custom detrending algorithms. (c) The spike events detected after applying a threshold filter.

.

A.9 Detailed process for DNA-PAINT and optoplasmonic sensing

A.10 More data showing the different NaCl concentration effect.

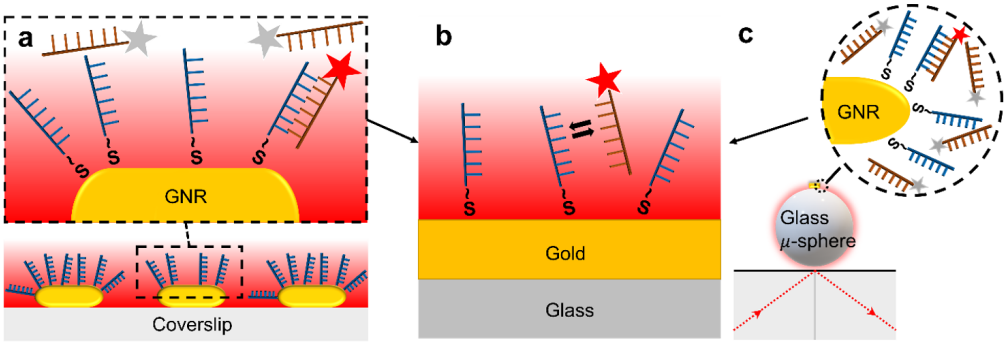

Figure A.9: Detailed schematic process for (a) DNA-PAINT and (c) optoplasmonic sensing (b) shows that in both experiments the reaction along the surface is the same, where docking strands are immobilised on the gold surface, and the imagers are transiently interacting with the docking strands. The imagers denoted by the red star provide signals.

.

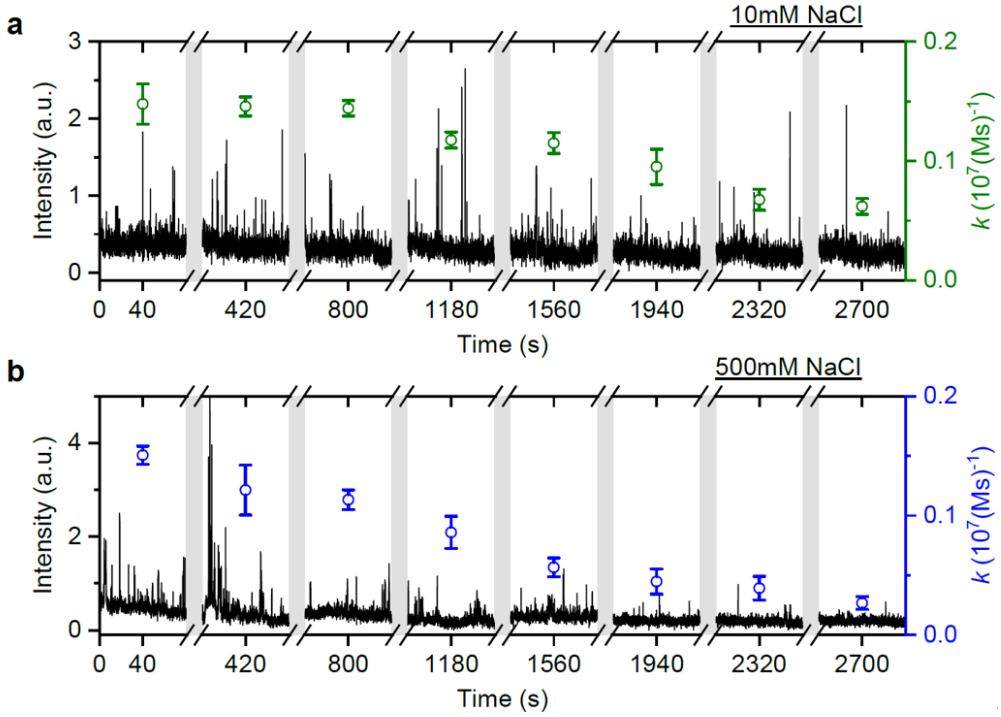

Figure A.10: The DNA-PAINT measurements with 20nM ImT22*D. The experiments are conducted with (a) 10mM NaCl HEPES buffer and (b) 500mM NaCl HEPES buffer. The event rates are plotted accordingly.

.

Bibliography

[1] Warwick Bowen, Frank Vollmer, and Reuven Gordon. *Single Molecule Sensing Beyond Fluorescence*. Springer, 2022.

[2] Helen Miller, Zhaokun Zhou, Jack Shepherd, Adam JM Wollman, and Mark C Leake. Single-molecule techniques in biophysics: a review of the progress in methods and applications. *Reports on Progress in Physics*, 81(2):024601, 2017.

[3] Keir C Neuman and Attila Nagy. Single-molecule force spectroscopy: optical tweezers, magnetic tweezers and atomic force microscopy. *Nature methods*, 5(6):491–505, 2008.

[4] Jian Liang and Julio M Fernández. Kinetic measurements on single-molecule disulfide bond cleavage. *Journal of the American Chemical Society*, 133(10):3528–3534, 2011.

[5] RM Georgevic. The solar radiation pressure force and torques model. *Journal of the Astronautical Sciences*, 20:257–274, 1973.

[6] Jacqueline LS Milne, Mario J Borgnia, Alberto Bartesaghi, Erin EH Tran, Lesley A Earl, David M Schauder, Jeffrey Lengyel, Jason Pierson, Ardan Patwardhan, and Sriram Subramaniam. Cryo-electron microscopy–a primer for the non-microscopist. *The FEBS journal*, 280(1):28–45, 2013.

[7] Denis Garoli, Hirohito Yamazaki, Nicolo Maccaferri, and Meni Wanunu. Plasmonic nanopores for single-molecule detection and manipulation: toward sequencing applications. *Nano letters*, 19(11):7553–7562, 2019.

[8] Alexander Riss, Alejandro Pérez Paz, Sebastian Wickenburg, Hsin-Zon Tsai, Dimas G De Oteyza, Aaron J Bradley, Miguel M Ugeda, Patrick Gorman, Han Sae Jung, Michael F Crommie, et al. Imaging single-molecule reaction intermediates stabilized by surface dissipation and entropy. *Nature chemistry*, 8(7):678–683, 2016.

[9] Brian J Beliveau, Alistair N Boettiger, Maier S Avendaño, Ralf Jungmann, Ruth B McCole, Eric F Joyce, Caroline Kim-Kiselak, Frédéric Bantignies, Chamith Y Fonseka, Jelena Erceg, et al. Single-molecule super-resolution imaging of chromosomes and in situ haplotype visualization using oligopaint fish probes. *Nature communications*, 6(1):1–13, 2015.

[10] Edward M Purcell. Life at low reynolds number. *American journal of physics*, 45(1):3–11, 1977.

[11] Harald Volkmann. Ernst abbe and his work. *Applied optics*, 5(11):1720–1731, 1966.

[12] Ernst HK Stelzer. Beyond the diffraction limit? *Nature*, 417(6891):806–807, 2002.

[13] Evgenii E Narimanov and Vladimir M Shalaev. Beyond diffraction. *Nature*, 447(7142):266–267, 2007.

[14] W Patrick Ambrose, Peter M Goodwin, Richard A Keller, and John C Martin. Alterations of single molecule fluorescence lifetimes in near-field optical microscopy. *Science*, 265(5170):364–367, 1994.

[15] Julia R Widom, Soma Dhakal, Laurie A Heinicke, and Nils G Walter. Single-molecule tools for enzymology, structural biology, systems biology and nanotechnology: an update. *Archives of toxicology*, 88(11):1965–1985, 2014.

[16] Narima Eerqing, Sivaraman Subramanian, Jesús Rubio, Tobias Lutz, Hsin-Yu Wu, Janet Anders, Christian Soeller, and Frank Vollmer. Comparing transient oligonucleotide hybridization kinetics using dna-paint and optoplasmonic

single-molecule sensing on gold nanorods. *ACS Photonics*, 8(10):2882–2888, 2021.

[17] Martin D Baaske, Matthew R Foreman, and Frank Vollmer. Single-molecule nucleic acid interactions monitored on a label-free microcavity biosensor platform. *Nature nanotechnology*, 9(11):933–939, 2014.

[18] Cecil E Hall. Method for the observation of macromolecules with the electron microscope illustrated with micrographs of dna. *The Journal of biophysical and biochemical cytology*, 2(5):625, 1956.

[19] Erin EH Tran, Mario J Borgnia, Oleg Kuybeda, David M Schauder, Alberto Bartesaghi, Gabriel A Frank, Guillermo Sapiro, Jacqueline LS Milne, and Sriram Subramaniam. Structural mechanism of trimeric hiv-1 envelope glycoprotein activation. *PLoS pathogens*, 8(7):e1002797, 2012.

[20] Audray Harris, Mario J Borgnia, Dan Shi, Alberto Bartesaghi, Haifeng He, Robert Pejchal, Yun Kang, Rafael Depetris, Andre J Marozsan, Rogier W Sanders, et al. Trimeric hiv-1 glycoprotein gp140 immunogens and native hiv-1 envelope glycoproteins display the same closed and open quaternary molecular architectures. *Proceedings of the National Academy of Sciences*, 108(28):11440–11445, 2011.

[21] Robert M Glaeser and Kenneth A Taylor. Radiation damage relative to transmission electron microscopy of biological specimens at low temperature: a review. *Journal of microscopy*, 112(1):127–138, 1978.

[22] Mike L Jenkins and Mark A Kirk. *Characterisation of radiation damage by transmission electron microscopy*. CRC Press, 2000.

[23] Robert O Kelley, Ronald AF Dekker, and John G Bluemink. Ligand-mediated osmium binding: its application in coating biological specimens for scanning electron microscopy. *Journal of ultrastructure research*, 45(3-4):254–258, 1973.

[24] Xiao-Chen Bai, Greg McMullan, and Sjors HW Scheres. How cryo-em is revolutionizing structural biology. *Trends in biochemical sciences*, 40(1):49–57, 2015.

[25] Jacques Dubochet. Cryo-em—the first thirty years. *Journal of microscopy*, 245(3):221–224, 2012.

[26] Robert M Glaeser. How good can cryo-em become? *Nature methods*, 13(1):28–32, 2016.

[27] Sjors HW Scheres. Processing of structurally heterogeneous cryo-em data in relion. *Methods in enzymology*, 579:125–157, 2016.

[28] Frank Oling, Jana Sopkova-de Oliveira Santos, Natalia Govorukhina, Christine Mazères-Dubut, Wilma Bergsma-Schutter, Gert Oostergetel, Wilko Keegstra, Olivier Lambert, Anita Lewit-Bentley, and Alain Brisson. Structure of membrane-bound annexin a5 trimers: a hybrid cryo-em-x-ray crystallography study. *Journal of molecular biology*, 304(4):561–573, 2000.

[29] James A Geraets, Karunakar R Pothula, and Gunnar F Schröder. Integrating cryo-em and nmr data. *Current opinion in structural biology*, 61:173–181, 2020.

[30] Robert M Glaeser. How good can single-particle cryo-em become? what remains before it approaches its physical limits? *Annual review of biophysics*, 48:45–61, 2019.

[31] Jodi A Hadden, Juan R Perilla, Christopher John Schlicksup, Balasubramanian Venkatakrishnan, Adam Zlotnick, and Klaus Schulten. All-atom molecular dynamics of the hbv capsid reveals insights into biological function and cryo-em resolution limits. *Elife*, 7:e32478, 2018.

[32] Peyman Milanfar. *Super-resolution imaging*. CRC press, 2017.

[33] Subhasis Chaudhuri. *Super-resolution imaging*, volume 632. Springer Science & Business Media, 2001.

[34] Sara A Jones, Sang-Hee Shim, Jiang He, and Xiaowei Zhuang. Fast, three-dimensional super-resolution imaging of live cells. *Nature methods*, 8(6):499–505, 2011.

[35] WE Moerner and David P Fromm. Methods of single-molecule fluorescence spectroscopy and microscopy. *Review of Scientific instruments*, 74(8):3597–3619, 2003.

[36] Ph Tamarat, A Maali, B Lounis, and M Orrit. Ten years of single-molecule spectroscopy. *The Journal of Physical Chemistry A*, 104(1):1–16, 2000.

[37] Thomas Basché, WE Moerner, M Orrit, and UP (eds Wild. *Single-molecule optical detection, imaging and spectroscopy*. John Wiley & Sons, 2008.

[38] Eric Betzig, A Lewis, A Harootunian, M Isaacson, and E Kratschmer. Near field scanning optical microscopy (nsom): development and biophysical applications. *Biophysical journal*, 49(1):269–279, 1986.

[39] Zhe Liu, Luke D Lavis, and Eric Betzig. Imaging live-cell dynamics and structure at the single-molecule level. *Molecular cell*, 58(4):644–659, 2015.

[40] JK Trautman, JJ Macklin, LE Brus, and E Betzig. Near-field spectroscopy of single molecules at room temperature. *Nature*, 369(6475):40–42, 1994.

[41] Stefan W Hell and Jan Wichmann. Breaking the diffraction resolution limit by stimulated emission: stimulated-emission-depletion fluorescence microscopy. *Optics letters*, 19(11):780–782, 1994.

[42] Eric Betzig. Proposed method for molecular optical imaging. *Optics letters*, 20(3):237–239, 1995.

[43] Leonhard Möckl, Don C Lamb, and Christoph Bräuchle. Super-resolved fluorescence microscopy: nobel prize in chemistry 2014 for eric betzig, stefan hell, and william e. moerner. *Angewandte Chemie International Edition*, 53(51):13972–13977, 2014.

[44] Thomas A Klar and Stefan W Hell. Subdiffraction resolution in far-field fluorescence microscopy. *Optics letters*, 24(14):954–956, 1999.

[45] Volker Westphal and Stefan W Hell. Nanoscale resolution in the focal plane of an optical microscope. *Physical review letters*, 94(14):143903, 2005.

[46] Birka Hein, Katrin I Willig, and Stefan W Hell. Stimulated emission depletion (sted) nanoscopy of a fluorescent protein-labeled organelle inside a living cell. *Proceedings of the National Academy of Sciences*, 105(38):14271–14276, 2008.

[47] Eric Betzig, George H Patterson, Rachid Sougrat, O Wolf Lindwasser, Scott Olenych, Juan S Bonifacino, Michael W Davidson, Jennifer Lippincott-Schwartz, and Harald F Hess. Imaging intracellular fluorescent proteins at nanometer resolution. *science*, 313(5793):1642–1645, 2006.

[48] Michael J Rust, Mark Bates, and Xiaowei Zhuang. Sub-diffraction-limit imaging by stochastic optical reconstruction microscopy (storm). *Nature methods*, 3(10):793–796, 2006.

[49] Ralf Jungmann, Maier S Avendaño, Johannes B Woehrstein, Mingjie Dai, William M Shih, and Peng Yin. Multiplexed 3d cellular super-resolution imaging with dna-paint and exchange-paint. *Nature methods*, 11(3):313–318, 2014.

[50] Mark Bates, Bo Huang, Graham T Dempsey, and Xiaowei Zhuang. Multicolor super-resolution imaging with photo-switchable fluorescent probes. *Science*, 317(5845):1749–1753, 2007.

[51] Jiang Jiang, Ken Bosnick, Mathieu Maillard, and Louis Brus. Single molecule raman spectroscopy at the junctions of large ag nanocrystals, 2003.

[52] Aftab Ahmed and Reuven Gordon. Single molecule directivity enhanced raman scattering using nanoantennas. *Nano letters*, 12(5):2625–2630, 2012.

[53] Katrin Kneipp, Harald Kneipp, and Henrik G Bohr. Single-molecule sers spectroscopy. In *Surface-Enhanced Raman Scattering*, pages 261–277. Springer, 2006.

[54] Bruno Pettinger. Tip-enhanced raman spectroscopy (ters). In *Surface-Enhanced Raman Scattering*, pages 217–240. Springer, 2006.

[55] Shuming Nie and Steven R Emory. Probing single molecules and single nanoparticles by surface-enhanced raman scattering. *science*, 275(5303):1102–1106, 1997.

[56] Regina Treffer, René Böhme, Tanja Deckert-Gaudig, Katherine Lau, Stephan Tiede, Xiumei Lin, and Volker Deckert. Advances in ters (tip-enhanced raman scattering) for biochemical applications. *Biochemical Society Transactions*, 40(4):609–614, 2012.

[57] NPW Pieczonka, G Moula, and RF Aroca. Serrs for single-molecule detection of dye-labeled phospholipids in langmuir- blodgett monolayers. *Langmuir*, 25(19):11261–11264, 2009.

[58] Felix Benz, Christos Tserkezis, Lars O Herrmann, Bart De Nijs, Alan Sanders, Daniel O Sigle, Laurynas Pukenas, Stephen D Evans, Javier Aizpurua, and Jeremy J Baumberg. Nanooptics of molecular-shunted plasmonic nanojunctions. *Nano letters*, 15(1):669–674, 2015.

[59] Kosti Tapio, Amr Mostafa, Yuya Kanehira, Antonio Suma, Anushree Dutta, and Ilko Bald. A versatile dna origami-based plasmonic nanoantenna for label-free single-molecule surface-enhanced raman spectroscopy. *ACS nano*, 15(4):7065–7077, 2021.

[60] Dongxing Wang, Wenqi Zhu, Michael D Best, Jon P Camden, and Kenneth B Crozier. Directional raman scattering from single molecules in the feed gaps of optical antennas. *Nano letters*, 13(5):2194–2198, 2013.

[61] Zheng Liu, Song-Yuan Ding, Zhao-Bin Chen, Xiang Wang, Jing-Hua Tian, Jason R Anema, Xiao-Shun Zhou, De-Yin Wu, Bing-Wei Mao, Xin Xu, et al. Revealing the molecular structure of single-molecule junctions in different conductance states by fishing-mode tip-enhanced raman spectroscopy. *Nature communications*, 2(1):1–6, 2011.

[62] Li-Jia Xu, Zhi-Chao Lei, Jiuxing Li, Cheng Zong, Chaoyong James Yang, and Bin Ren. Label-free surface-enhanced raman spectroscopy detection of dna with single-base sensitivity. *Journal of the American Chemical Society*, 137(15):5149–5154, 2015.

[63] Lamyaa M Almehmadi, Stephanie M Curley, Natalya A Tokranova, Scott A Tenenbaum, and Igor K Lednev. Surface enhanced raman spectroscopy for single molecule protein detection. *Scientific reports*, 9(1):1–9, 2019.

[64] Eckhard Mandelkow and Andreas Hoenger. Structures of kinesin and kinesin–microtubule interactions. *Current opinion in cell biology*, 11(1):34–44, 1999.

[65] Carla Tucker and Lawrence SB Goldstein. Probing the kinesin-microtubule interaction. *Journal of Biological Chemistry*, 272(14):9481–9488, 1997.

[66] Daniel A Koster, Aurélien Crut, Stewart Shuman, Mary-Ann Bjornsti, and Nynke H Dekker. Cellular strategies for regulating dna supercoiling: a single-molecule perspective. *Cell*, 142(4):519–530, 2010.

[67] Shannon J McKie, Keir C Neuman, and Anthony Maxwell. Dna topoisomerases: Advances in understanding of cellular roles and multi-protein complexes via structure-function analysis. *Bioessays*, 43(4):2000286, 2021.

[68] Jeffrey R Moffitt, Yann R Chemla, Steven B Smith, and Carlos Bustamante. Recent advances in optical tweezers. *Annu. Rev. Biochem.*, 77:205–228, 2008.

[69] Philip Jones, Onofrio Maragó, and Giovanni Volpe. *Optical tweezers*. Cambridge University Press Cambridge, UK:, 2015.

[70] Iwijn De Vlaminck and Cees Dekker. Recent advances in magnetic tweezers. *Annu. Rev. Biophys*, 41(1):453–472, 2012.

[71] F Oesterhelt, M Rief, and HE Gaub. Single molecule force spectroscopy by afm indicates helical structure of poly (ethylene-glycol) in water. *New Journal of Physics*, 1(1):6, 1999.

[72] M Ludwig, M Rief, L Schmidt, H Li, F Oesterhelt, M Gautel, and HE Gaub. Afm, a tool for single-molecule experiments. *Applied Physics A*, 68(2):173–176, 1999.

[73] Domna G Kotsifaki and Síle Nic Chormaic. Plasmonic optical tweezers based on nanostructures: fundamentals, advances and prospects. *Nanophotonics*, 8(7):1227–1245, 2019.

[74] Amit D Mehta, Ronald S Rock, Matthias Rief, James A Spudich, Mark S Mooseker, and Richard E Cheney. Myosin-v is a processive actin-based motor. *Nature*, 400(6744):590–593, 1999.

[75] Steven M Block, Lawrence S B Goldstein, and Bruce J Schnapp. Bead movement by single kinesin molecules studied with optical tweezers. *Nature*, 348(6299):348–352, 1990.

[76] Karel Svoboda and Steven M Block. Force and velocity measured for single kinesin molecules. *Cell*, 77(5):773–784, 1994.

[77] William J Greenleaf, Michael T Woodside, Elio A Abbondanzieri, and Steven M Block. Passive all-optical force clamp for high-resolution laser trapping. *Physical review letters*, 95(20):208102, 2005.

[78] Jeffrey R Moffitt, Yann R Chemla, David Izhaky, and Carlos Bustamante. Differential detection of dual traps improves the spatial resolution of optical tweezers. *Proceedings of the National Academy of Sciences*, 103(24):9006–9011, 2006.

[79] J Christof M Gebhardt, Thomas Bornschlögl, and Matthias Rief. Full distance-resolved folding energy landscape of one single protein molecule. *Proceedings of the National Academy of Sciences*, 107(5):2013–2018, 2010.

[80] Marco Ribezzi-Crivellari, Josep Maria Huguet, and Felix Ritort. Counter-propagating dual-trap optical tweezers based on linear momentum conservation. *Review of Scientific Instruments*, 84(4):043104, 2013.

[81] Yuanjie Pang and Reuven Gordon. Optical trapping of a single protein. *Nano letters*, 12(1):402–406, 2012.

[82] Ahmed A Al Balushi and Reuven Gordon. Label-free free-solution single-molecule protein–small molecule interaction observed by double-nanohole plasmonic trapping. *ACS photonics*, 1(5):389–393, 2014.

[83] Tatsuya Shoji, Junki Saitoh, Noboru Kitamura, Fumika Nagasawa, Kei Murakoshi, Hiroaki Yamauchi, Syoji Ito, Hiroshi Miyasaka, Hajime Ishihara, and Yasuyuki Tsuboi. Permanent fixing or reversible trapping and release of dna micropatterns on a gold nanostructure using continuous-wave or femtosecond-pulsed near-infrared laser light. *Journal of the American Chemical Society*, 135(17):6643–6648, 2013.

[84] Dylan M Owen, Carles Rentero, Jérémie Rossy, Astrid Magenau, David Williamson, Macarena Rodriguez, and Katharina Gaus. Palm imaging and cluster analysis of protein heterogeneity at the cell surface. *Journal of biophotonics*, 3(7):446–454, 2010.

[85] Michael J. Rust, Mark Bates, and Xiaowei Zhuang. Sub-diffraction-limit imaging by stochastic optical reconstruction microscopy (STORM). *Nature Methods*, 3(10):793–795, oct 2006.

[86] Joerg Schnitzbauer, Maximilian T Strauss, Thomas Schlichthaerle, Florian Schueder, and Ralf Jungmann. Super-resolution microscopy with dna-paint. *Nature protocols*, 12(6):1198–1228, 2017.

[87] Gregory Giannone, Eric Hosy, Jean-Baptiste Sibarita, Daniel Choquet, and Laurent Cognet. High-content super-resolution imaging of live cell by upaint. In *Nanoimaging*, pages 95–110. Springer, 2013.

[88] Ralf Jungmann, Christian Steinhauer, Max Scheible, Anton Kuzyk, Philip Tinnefeld, and Friedrich C Simmel. Single-molecule kinetics and super-resolution microscopy by fluorescence imaging of transient binding on dna origami. *Nano letters*, 10(11):4756–4761, 2010.

[89] Alexey Sharonov and Robin M Hochstrasser. Wide-field subdiffraction imaging by accumulated binding of diffusing probes. *Proceedings of the National Academy of Sciences*, 103(50):18911–18916, 2006.

[90] Daniel J Nieves, Katharina Gaus, and Matthew AB Baker. Dna-based super-resolution microscopy: Dna-paint. *Genes*, 9(12):621, 2018.

[91] Ralf Jungmann, Max Scheible, and Friedrich C Simmel. Nanoscale imaging in dna nanotechnology. *Wiley Interdisciplinary Reviews: Nanomedicine and Nanobiotechnology*, 4(1):66–81, 2012.

[92] Chenxiang Lin, Ralf Jungmann, Andrew M Leifer, Chao Li, Daniel Levner, George M Church, William M Shih, and Peng Yin. Submicrometre geometrically encoded fluorescent barcodes self-assembled from dna. *Nature chemistry*, 4(10):832–839, 2012.

[93] Raman van Wee, Mike Filius, and Chirlmin Joo. Completing the canvas: advances and challenges for dna-paint super-resolution imaging. *Trends in Biochemical Sciences*, 46(11):918–930, 2021.

[94] Tai Kiuchi, Makio Higuchi, Akihiro Takamura, Masahiro Maruoka, and Naoki Watanabe. Multitarget super-resolution microscopy with high-density labeling by exchangeable probes. *Nature methods*, 12(8):743–746, 2015.

[95] Nina S Deussner-Helfmann, Alexander Auer, Maximilian T Strauss, Paul Donlin-Asp, Sebastian Malkusch, Marina S Dietz, Hans-Dieter Barth, Erin

Schuman, Ralf Jungmann, and Mike Heilemann. Correlating dna-paint and single-molecule fret for multiplexed super-resolution imaging. In *Single Molecule Spectroscopy and Superresolution Imaging XIII*, volume 11246, pages 44–50. SPIE, 2020.

[96] Orsolya K Wade, Johannes B Woehrstein, Philipp C Nickels, Sebastian Strauss, Florian Stehr, Johannes Stein, Florian Schueder, Maximilian T Strauss, Mahipal Ganji, Joerg Schnitzbauer, et al. 124-color super-resolution imaging by engineering dna-paint blinking kinetics. *Nano letters*, 19(4):2641–2646, 2019.

[97] Tobias Lutz, Alexander H Clowsley, Ruisheng Lin, Stefano Pagliara, Lorenzo Di Michele, and Christian Soeller. Versatile multiplexed super-resolution imaging of nanostructures by quencher-exchange-paint. *Nano Research*, 11(12):6141–6154, 2018.

[98] Ralf Jungmann, Maier S Avendaño, Mingjie Dai, Johannes B Woehrstein, Sarit S Agasti, Zachary Feiger, Avital Rodal, and Peng Yin. Quantitative super-resolution imaging with qpaint. *Nature methods*, 13(5):439–442, 2016.

[99] Pablo A Gómez-García, Erik T Garbacik, Jason J Otterstrom, Maria F Garcia-Parajo, and Melike Lakadamyali. Excitation-multiplexed multicolor superresolution imaging with fm-storm and fm-dna-paint. *Proceedings of the National Academy of Sciences*, 115(51):12991–12996, 2018.

[100] Ann L McEvoy, Derek Greenfield, Mark Bates, and Jan Liphardt. Q&a: Single-molecule localization microscopy for biological imaging. *BMC biology*, 8(1):1–9, 2010.

[101] Shih-Ya Chen, Rainer Heintzmann, and Christoph Cremer. Sample drift estimation method based on speckle patterns formed by backscattered laser light. *Biomedical Optics Express*, 10(12):6462–6475, 2019.

[102] Joshua M Brockman, Hanquan Su, Aaron T Blanchard, Yuxin Duan, Travis Meyer, M Edward Quach, Roxanne Glazier, Alisina Bazrafshan, Rachel L

Bender, Anna V Kellner, et al. Live-cell super-resolved paint imaging of piconewton cellular traction forces. *Nature methods*, 17(10):1018–1024, 2020.

[103] Makio Tokunaga, Naoko Imamoto, and Kumiko Sakata-Sogawa. Highly inclined thin illumination enables clear single-molecule imaging in cells. *Nature methods*, 5(2):159–161, 2008.

[104] Wesley R Legant, Lin Shao, Jonathan B Grimm, Timothy A Brown, Daniel E Milkie, Brian B Avants, Luke D Lavis, and Eric Betzig. High-density three-dimensional localization microscopy across large volumes. *Nature methods*, 13(4):359–365, 2016.

[105] Priyabrata Pattnaik. Surface plasmon resonance. *Applied biochemistry and biotechnology*, 126(2):79–92, 2005.

[106] Marek Piliarik, Hana Vaisocherová, and Jiří Homola. Surface plasmon resonance biosensing. *Biosensors and Biodetection*, pages 65–88, 2009.

[107] JAd De Feijter, d J Benjamins, and FA Veer. Ellipsometry as a tool to study the adsorption behavior of synthetic and biopolymers at the air–water interface. *Biopolymers: Original Research on Biomolecules*, 17(7):1759–1772, 1978.

[108] Hana Šípová and Jiří Homola. Surface plasmon resonance sensing of nucleic acids: A review. *Analytica chimica acta*, 773:9–23, 2013.

[109] Hoang Hiep Nguyen, Jeho Park, Sebyung Kang, and Moonil Kim. Surface plasmon resonance: a versatile technique for biosensor applications. *Sensors*, 15(5):10481–10510, 2015.

[110] Adam B Taylor and Peter Zijlstra. Single-molecule plasmon sensing: current status and future prospects. *ACS sensors*, 2(8):1103–1122, 2017.

[111] Adam D McFarland and Richard P Van Duyne. Single silver nanoparticles as real-time optical sensors with zeptomole sensitivity. *Nano letters*, 3(8):1057–1062, 2003.

[112] G Raschke, S Kowarik, T Franzl, C Sönnichsen, TA Klar, J Feldmann, A Nichtl, and K Kürzinger. Biomolecular recognition based on single gold nanoparticle light scattering. *Nano letters*, 3(7):935–938, 2003.

[113] G Raschke, S Brogl, AS Susha, AL Rogach, TA Klar, J Feldmann, B Fieres, N Petkov, T Bein, A Nichtl, et al. Gold nanoshells improve single nanoparticle molecular sensors. *Nano letters*, 4(10):1853–1857, 2004.

[114] Leif J Sherry, Rongchao Jin, Chad A Mirkin, George C Schatz, and Richard P Van Duyne. Localized surface plasmon resonance spectroscopy of single silver triangular nanoprisms. *Nano letters*, 6(9):2060–2065, 2006.

[115] Cristina L Baciu, Jan Becker, Andreas Janshoff, and Carsten Sonnichsen. Protein–membrane interaction probed by single plasmonic nanoparticles. *Nano Letters*, 8(6):1724–1728, 2008.

[116] William J Galush, Sarah A Shelby, Martin J Mulvihill, Andrea Tao, Peidong Yang, and Jay T Groves. A nanocube plasmonic sensor for molecular binding on membrane surfaces. *Nano letters*, 9(5):2077–2082, 2009.

[117] Greg J Nusz, Adam C Curry, Stella M Marinakos, Adam Wax, and Ashutosh Chilkoti. Rational selection of gold nanorod geometry for label-free plasmonic biosensors. *ACS nano*, 3(4):795–806, 2009.

[118] Jan Becker, Andreas Trügler, Arpad Jakab, Ulrich Hohenester, and Carsten Sonnichsen. The optimal aspect ratio of gold nanorods for plasmonic biosensing. *Plasmonics*, 5(2):161–167, 2010.

[119] Greg J Nusz, Stella M Marinakos, Adam C Curry, Andreas Dahlin, Fredrik Höök, Adam Wax, and Ashutosh Chilkoti. Label-free plasmonic detection of biomolecular binding by a single gold nanorod. *Analytical chemistry*, 80(4):984–989, 2008.

[120] Christina Rosman, Janak Prasad, Andreas Neiser, Andreas Henkel, Jonathan Edgar, and Carsten Sonnichse. Multiplexed plasmon sensor for rapid label-free analyte detection. *Nano letters*, 13(7):3243–3247, 2013.

[121] Marco Capitanio and Francesco S Pavone. Interrogating biology with force: single molecule high-resolution measurements with optical tweezers. *Biophysical journal*, 105(6):1293–1303, 2013.

[122] J Justin Gooding and Katharina Gaus. Single-molecule sensors: challenges and opportunities for quantitative analysis. *Angewandte Chemie International Edition*, 55(38):11354–11366, 2016.

[123] Molly M Miller and Anne A Lazarides. Sensitivity of metal nanoparticle surface plasmon resonance to the dielectric environment. *The Journal of Physical Chemistry B*, 109(46):21556–21565, 2005.

[124] Tomasz J Antosiewicz, S Peter Apell, Virginia Claudio, and Mikael Käll. A simple model for the resonance shift of localized plasmons due to dielectric particle adhesion. *Optics Express*, 20(1):524–533, 2012.

[125] Jianji Yang, Harald Giessen, and Philippe Lalanne. Simple analytical expression for the peak-frequency shifts of plasmonic resonances for sensing. *Nano letters*, 15(5):3439–3444, 2015.

[126] Guowei Lu, Lei Hou, Tianyue Zhang, Wenqiang Li, Jie Liu, Pascal Perriat, and Qihuang Gong. Anisotropic plasmonic sensing of individual or coupled gold nanorods. *The Journal of Physical Chemistry C*, 115(46):22877–22885, 2011.

[127] TJ Davis, DE Gómez, and KC Vernon. Interaction of molecules with localized surface plasmons in metallic nanoparticles. *Physical Review B*, 81(4):045432, 2010.

[128] Tomasz J Antosiewicz and Mikael Kall. A multiscale approach to modeling plasmonic nanorod biosensors. *The Journal of Physical Chemistry C*, 120(37):20692–20701, 2016.

[129] Peter Zijlstra, Pedro MR Paulo, and Michel Orrit. Optical detection of single non-absorbing molecules using the surface plasmon resonance of a gold nanorod. *Nature nanotechnology*, 7(6):379–382, 2012.

[130] Kathryn M Mayer, Feng Hao, Seunghyun Lee, Peter Nordlander, and Jason H Hafner. A single molecule immunoassay by localized surface plasmon resonance. *Nanotechnology*, 21(25):255503, 2010.

[131] Paul E Sheehan and Lloyd J Whitman. Detection limits for nanoscale biosensors. *Nano letters*, 5(4):803–807, 2005.

[132] Anastasiya Puchkova, Carolin Vietz, Enrico Pibiri, Bettina Wunsch, Maria Sanz Paz, Guillermo P Acuna, and Philip Tinnefeld. Dna origami nanoantennas with over 5000-fold fluorescence enhancement and single-molecule detection at 25 μm. *Nano letters*, 15(12):8354–8359, 2015.

[133] Martin D. Baaske, Matthew R. Foreman, and Frank Vollmer. Single-molecule nucleic acid interactions monitored on a label-free microcavity biosensor platform. *Nature Nanotechnology*, 9(11):933–939, nov 2014.

[134] Martin D Baaske and Frank Vollmer. Optical observation of single atomic ions interacting with plasmonic nanorods in aqueous solution. *Nature Photonics*, 10(11):733–739, 2016.

[135] Eugene Kim, Martin D Baaske, Isabel Schuldes, Peter S Wilsch, and Frank Vollmer. Label-free optical detection of single enzyme-reactant reactions and associated conformational changes. *Science advances*, 3(3):e1603044, 2017.

[136] Mikhail L Gorodetsky, Anatoly A Savchenkov, and Vladimir S Ilchenko. Ultimate q of optical microsphere resonators. *Optics letters*, 21(7):453–455, 1996.

[137] VB Braginsky, ML Gorodetsky, and VS Ilchenko. Quality-factor and nonlinear properties of optical whispering-gallery modes. *Physics letters A*, 137(7-8):393–397, 1989.

[138] DW Vernooy, Vladimir S Ilchenko, H Mabuchi, EW Streed, and HJ Kimble. High-q measurements of fused-silica microspheres in the near infrared. *Optics letters*, 23(4):247–249, 1998.

[139] Xuefeng Jiang, Abraham J Qavi, Steven H Huang, and Lan Yang. Whispering-gallery sensors. *Matter*, 3(2):371–392, 2020.

[140] Jiangang Zhu, Sahin Kaya Ozdemir, Yun-Feng Xiao, Lin Li, Lina He, Da-Ren Chen, and Lan Yang. On-chip single nanoparticle detection and sizing by mode splitting in an ultrahigh-q microresonator. *Nature photonics*, 4(1):46–49, 2010.

[141] Fea Vollmer, Daniela Braun, Albert Libchaber, Masoud Khoshsima, Iwao Teraoka, and Susan Arnold. Protein detection by optical shift of a resonant microcavity. *Applied physics letters*, 80(21):4057–4059, 2002.

[142] Matthew R Foreman, Jon D Swaim, and Frank Vollmer. Whispering gallery mode sensors: erratum. *Advances in Optics and Photonics*, 7(3):632–634, 2015.

[143] Frank Vollmer and Stephen Arnold. Whispering-gallery-mode biosensing: label-free detection down to single molecules. *Nature methods*, 5(7):591–596, 2008.

[144] Frank Vollmer, Stephen Arnold, and David Keng. Single virus detection from the reactive shift of a whispering-gallery mode. *Proceedings of the National Academy of Sciences*, 105(52):20701–20704, 2008.

[145] Tchern Lenn and Mark C Leake. Experimental approaches for addressing fundamental biological questions in living, functioning cells with single molecule precision. *Open biology*, 2(6):120090, 2012.

[146] Helen Miller, Zhaokun Zhou, Jack Shepherd, Adam J M Wollman, and Mark C Leake. Single-molecule techniques in biophysics: a review of the progress in methods and applications. *Reports on Progress in Physics*, 81(2):24601, 2017.

[147] Bin Yu, Danni Chen, Junle Qu, and Hanben Niu. Fast Fourier domain localization algorithm of a single molecule with nanometer precision. *Optics letters*, 36(22):4317–4319, 2011.

[148] Stefan K Kufer, Mathias Strackharn, Stefan W Stahl, Hermann Gumpp, Elias M Puchner, and Hermann E Gaub. Optically monitoring the mechanical assembly of single molecules. *Nature nanotechnology*, 4(1):45–49, 2009.

[149] Peter Hinterdorfer and Yves F Dufrêne. Detection and localization of single molecular recognition events using atomic force microscopy. *Nature methods*, 3(5):347–355, 2006.

[150] Eric Betzig, George H Patterson, Rachid Sougrat, O Wolf Lindwasser, Scott Olenych, Juan S Bonifacino, Michael W Davidson, Jennifer Lippincott-Schwartz, and Harald F Hess. Imaging intracellular fluorescent proteins at nanometer resolution. *Science*, 313(5793):1642–1645, 2006.

[151] Samuel T Hess, Thanu P K Girirajan, and Michael D Mason. Ultra-high resolution imaging by fluorescence photoactivation localization microscopy. *Biophysical journal*, 91(11):4258–4272, 2006.

[152] Ralf Jungmann, Maier S Avendaño, Johannes B Woehrstein, Mingjie Dai, William M Shih, and Peng Yin. Multiplexed 3D cellular super-resolution imaging with DNA-PAINT and Exchange-PAINT. *Nature methods*, 11(3):313–318, 2014.

[153] Joerg Schnitzbauer, Maximilian T Strauss, Thomas Schlichthaerle, Florian Schueder, and Ralf Jungmann. Super-resolution microscopy with DNA-PAINT. *Nature protocols*, 12(6):1198, 2017.

[154] Ruisheng Lin, Alexander H Clowsley, Tobias Lutz, David Baddeley, and Christian Soeller. 3D super-resolution microscopy performance and quantitative analysis assessment using DNA-PAINT and DNA origami test samples. *Methods*, 174:56–71, 2020.

[155] Borja Sepúlveda, Paula C Angelomé, Laura M Lechuga, and Luis M Liz-Marzán. LSPR-based nanobiosensors. *nano today*, 4(3):244–251, 2009.

[156] Weichun Zhang, Martín Caldarola, Xuxing Lu, Biswajit Pradhan, and Michel Orrit. Single-molecule fluorescence enhancement of a near-infrared dye by gold nanorods using DNA transient binding. *Physical Chemistry Chemical Physics*, 20(31):20468–20475, 2018.

[157] Michelle Duval Malinsky, K Lance Kelly, George C Schatz, and Richard P Van Duyne. Chain length dependence and sensing capabilities of the localized surface plasmon resonance of silver nanoparticles chemically modified with alkanethiol self-assembled monolayers. *Journal of the American Chemical Society*, 123(7):1471–1482, 2001.

[158] Amanda J Haes, Shengli Zou, George C Schatz, and Richard P Van Duyne. A nanoscale optical biosensor: the long range distance dependence of the localized surface plasmon resonance of noble metal nanoparticles. *The Journal of Physical Chemistry B*, 108(1):109–116, 2004.

[159] Greg J Nusz, Adam C Curry, Stella M Marinakos, Adam Wax, and Ashutosh Chilkoti. Rational selection of gold nanorod geometry for label-free plasmonic biosensors. *ACS nano*, 3(4):795–806, 2009.

[160] Serge Vincent, Sivaraman Subramanian, and Frank Vollmer. Optoplasmonic characterisation of reversible disulfide interactions at single thiol sites in the attomolar regime. *Nature Communications*, 11(1):2043, dec 2020.

[161] Marina S. Dietz, S. Sophia Wehrheim, Marie Lena I.E. Harwardt, Hartmut H. Niemann, and Mike Heilemann. Competitive Binding Study Revealing the

Influence of Fluorophore Labels on Biomolecular Interactions. *Nano Letters*, 19(11):8245–8249, 2019.

[162] Eric M. Peterson, Eric J. Reece, Wenyuan Li, and Joel M. Harris. Super-Resolution Imaging of Competitive Unlabeled DNA Hybridization Reveals the Influence of Fluorescent Labels on Duplex Formation and Dissociation Kinetics. *The Journal of Physical Chemistry B*, 123(50):10746–10756, dec 2019.

[163] Zackary A. Zimmers, Nicholas M. Adams, William E. Gabella, and Frederick R. Haselton. Fluorophore-quencher interactions effect on hybridization characteristics of complementary oligonucleotides. *Analytical Methods*, 11(22):2862–2867, 2019.

[164] Katherine A Willets. Supercharging superlocalization microscopy: how electrochemical charging of plasmonic nanostructures uncovers hidden heterogeneity. *ACS nano*, 13(6):6145–6150, 2019.

[165] Chad P Byers, Benjamin S Hoener, Wei-Shun Chang, Mustafa Yorulmaz, Stephan Link, and Christy F Landes. Single-particle spectroscopy reveals heterogeneity in electrochemical tuning of the localized surface plasmon. *The Journal of Physical Chemistry B*, 118(49):14047–14055, 2014.

[166] Sandeep Kaushal, Sitansu Sekhar Nanda, Dong Kee Yi, and Heongkyu Ju. Effects of Aspect Ratio Heterogeneity of an Assembly of Gold Nanorod on Localized Surface Plasmon Resonance. *The Journal of Physical Chemistry Letters*, 11(15):5972–5979, 2020.

[167] Ralf Jungmann, Christian Steinhauer, Max Scheible, Anton Kuzyk, Philip Tinnefeld, and Friedrich C Simmel. Single-molecule kinetics and super-resolution microscopy by fluorescence imaging of transient binding on DNA origami. *Nano letters*, 10(11):4756–4761, 2010.

[168] Andreas B. Dahlin, Jonas O. Tegenfeldt, and Fredrik Höök. Improving the Instrumental Resolution of Sensors Based on Localized Surface Plasmon Resonance. *Analytical Chemistry*, 78(13):4416–4423, jul 2006.

[169] Kenneth J Breslauer, Ronald Frank, Helmut Blöcker, and Luis A Marky. Predicting dna duplex stability from the base sequence. *Proceedings of the National Academy of Sciences*, 83(11):3746–3750, 1986.

[170] Rebecca Andrews. DNA hybridisation kinetics using single-molecule fluorescence imaging. *Essays in Biochemistry*, 65(1):27–36, apr 2021.

[171] E. Kim, M. D. Baaske, and F. Vollmer. In situ observation of single-molecule surface reactions from low to high affinities. *Adv Mater*, 28(45):9941–9948, 2016.

[172] S. Elzey, D. H. Tsai, S. A. Rabb, L. L. Yu, M. R. Winchester, and V. A. Hackley. Quantification of ligand packing density on gold nanoparticles using icp-oes. *Anal Bioanal Chem*, 403(1):145–9, 2012.

[173] Jinny X Zhang, John Z Fang, Wei Duan, Lucia R Wu, Angela W Zhang, Neil Dalchau, Boyan Yordanov, Rasmus Petersen, Andrew Phillips, and David Yu Zhang. Predicting dna hybridization kinetics from sequence. *Nature chemistry*, 10(1):91–98, 2018.

[174] Honglin Li and Joshua C Vaughan. Switchable fluorophores for single-molecule localization microscopy. *Chemical reviews*, 118(18):9412–9454, 2018.

[175] Ismail M Khater, Ivan Robert Nabi, and Ghassan Hamarneh. A review of super-resolution single-molecule localization microscopy cluster analysis and quantification methods. *Patterns*, 1(3):100038, 2020.

[176] Fadi M Jradi and Luke D Lavis. Chemistry of photosensitive fluorophores for single-molecule localization microscopy. *ACS Chemical Biology*, 14(6):1077–1090, 2019.

[177] Robin Diekmann, Maurice Kahnwald, Andreas Schoenit, Joran Deschamps, Ulf Matti, and Jonas Ries. Optimizing imaging speed and excitation intensity for single-molecule localization microscopy. *Nature methods*, 17(9):909–912, 2020.

[178] M Bouzin, M Marini, A Zeynali, M Borzenkov, L Sironi, L D'Alfonso, F Mingozzi, F Granucci, P Pallavicini, G Chirico, et al. Photo-activated raster scanning thermal imaging at sub-diffraction resolution. *Nature communications*, 10(1):1–9, 2019.

[179] Jianquan Xu, Hongqiang Ma, and Yang Liu. Stochastic optical reconstruction microscopy (storm). *Current protocols in cytometry*, 81(1):12–46, 2017.

[180] Sebastian Strauss and Ralf Jungmann. Up to 100-fold speed-up and multiplexing in optimized dna-paint. *Nature methods*, 17(8):789–791, 2020.

[181] Mike Filius, Tao Ju Cui, Adithya N Ananth, Margreet W Docter, Jorrit W Hegge, John van der Oost, and Chirlmin Joo. High-speed super-resolution imaging using protein-assisted dna-paint. *Nano letters*, 20(4):2264–2270, 2020.

[182] Ruisheng Lin, Alexander H Clowsley, Tobias Lutz, David Baddeley, and Christian Soeller. 3d super-resolution microscopy performance and quantitative analysis assessment using dna-paint and dna origami test samples. *Methods*, 174:56–71, 2020.

[183] Rizia Bardhan, Nathaniel K Grady, Joseph R Cole, Amit Joshi, and Naomi J Halas. Fluorescence enhancement by au nanostructures: nanoshells and nanorods. *ACS nano*, 3(3):744–752, 2009.

[184] Pedro MR Paulo, David Botequim, Agnieszka Jóskowiak, Sofia Martins, Duarte MF Prazeres, Peter Zijlstra, and Sílvia MB Costa. Enhanced fluorescence of a dye on dna-assembled gold nanodimers discriminated by lifetime correlation spectroscopy. *The Journal of Physical Chemistry C*, 122(20):10971–10980, 2018.

[185] Haifeng Yuan, Saumyakanti Khatua, Peter Zijlstra, Mustafa Yorulmaz, and Michel Orrit. Thousand-fold enhancement of single-molecule fluorescence near a single gold nanorod. *Angewandte Chemie*, 125(4):1255–1259, 2013.

[186] Sivaraman Subramanian, Kulathunga Mudalige Kalani Perera, Srikanth Pedireddy, and Frank Vollmer. Optoplasmonic whispering gallery mode sensors for single molecule characterization: A practical guide. In *Single Molecule Sensing Beyond Fluorescence*, pages 37–96. Springer, 2022.

[187] Sivaraman Subramanian, Hannah BL Jones, Simona Frustaci, Samuel Winter, Marc W van der Kamp, Vickery L Arcus, Christopher R Pudney, and Frank Vollmer. Sensing enzyme activation heat capacity at the single-molecule level using gold-nanorod-based optical whispering gallery modes. *ACS Applied Nano Materials*, 4(5):4576–4583, 2021.

[188] Frank Vollmer and Deshui Yu. *Optical Whispering Gallery Modes for Biosensing*. Springer, 2020.

[189] Xiao-Chong Yu, Shui-Jing Tang, Wenjing Liu, Yinglun Xu, Qihuang Gong, You-Ling Chen, and Yun-Feng Xiao. Single-molecule optofluidic microsensor with interface whispering gallery modes. *Proceedings of the National Academy of Sciences*, 119(6):e2108678119, 2022.

[190] Weichun Zhang, Martín Caldarola, Xuxing Lu, Biswajit Pradhan, and Michel Orrit. Single-molecule fluorescence enhancement of a near-infrared dye by gold nanorods using dna transient binding. *Physical Chemistry Chemical Physics*, 20(31):20468–20475, 2018.

[191] Adam Taylor, René Verhoef, Michael Beuwer, Yuyang Wang, and Peter Zijlstra. All-optical imaging of gold nanoparticle geometry using super-resolution microscopy. *The Journal of Physical Chemistry C*, 122(4):2336–2342, 2018.

[192] Martin Ovesnỳ, Pavel Křížek, Josef Borkovec, Zdeněk Švindrych, and Guy M Hagen. Thunderstorm: a comprehensive imagej plug-in for palm and storm

data analysis and super-resolution imaging. *Bioinformatics*, 30(16):2389–2390, 2014.

[193] Sabrina Simoncelli, Yi Li, Emiliano Cortés, and Stefan A Maier. Nanoscale control of molecular self-assembly induced by plasmonic hot-electron dynamics. *ACS nano*, 12(3):2184–2192, 2018.

[194] Dieter W Gruenwedel and Chi-Hsia Hsu. Salt effects on the denaturation of dna. *Biopolymers: Original Research on Biomolecules*, 7(4):557–570, 1969.

[195] Neil A Straus and Tom I Bonner. Temperature dependence of rna-dna hybridization kinetics. *Biochimica et Biophysica Acta (BBA)-Nucleic Acids and Protein Synthesis*, 277(1):87–95, 1972.

[196] Daniel Wüstner, Tanja Christensen, Lukasz M Solanko, and Daniel Sage. Photobleaching kinetics and time-integrated emission of fluorescent probes in cellular membranes. *Molecules*, 19(8):11096–11130, 2014.

[197] Taka A Tsunoyama, Yusuke Watanabe, Junri Goto, Kazuma Naito, Rinshi S Kasai, Kenichi GN Suzuki, Takahiro K Fujiwara, and Akihiro Kusumi. Super-long single-molecule tracking reveals dynamic-anchorage-induced integrin function. *Nature chemical biology*, 14(5):497–506, 2018.

[198] Aaron L Rozelle, Young Cheun, Caroline K Vilas, Myong-Chul Koag, and Seongmin Lee. Dna interstrand cross-links induced by the major oxidative adenine lesion 7, 8-dihydro-8-oxoadenine. *Nature communications*, 12(1):1–16, 2021.

[199] Elisa Carrasco, Juan Carlos Stockert, Ángeles Juarranz, and Alfonso Blázquez-Castro. Plasmonic hot-electron reactive oxygen species generation: fundamentals for redox biology. *Frontiers in Chemistry*, page 1160, 2020.

[200] Eric M Peterson, Michael W Manhart, and Joel M Harris. Single-molecule fluorescence imaging of interfacial dna hybridization kinetics at selective capture surfaces. *Analytical chemistry*, 88(2):1345–1354, 2016.

[201] Eric M Peterson and Joel M Harris. Identification of individual immobilized dna molecules by their hybridization kinetics using single-molecule fluorescence imaging. *Analytical chemistry*, 90(8):5007–5014, 2018.

[202] Alexander W Peterson, Lauren K Wolf, and Rosina M Georgiadis. Hybridization of mismatched or partially matched dna at surfaces. *Journal of the American Chemical Society*, 124(49):14601–14607, 2002.

[203] Shicai Xu, Jian Zhan, Baoyuan Man, Shouzhen Jiang, Weiwei Yue, Shoubao Gao, Chengang Guo, Hanping Liu, Zhenhua Li, Jihua Wang, et al. Real-time reliable determination of binding kinetics of dna hybridization using a multi-channel graphene biosensor. *Nature communications*, 8(1):1–10, 2017.

[204] Sergio Kogikoski Jr, Anushree Dutta, and Ilko Bald. Spatial separation of plasmonic hot-electron generation and a hydrodehalogenation reaction center using a dna wire. *ACS nano*, 15(12):20562–20573, 2021.

[205] Jia Liu, Zhuan-Yun Cai, Wei-Xin Sun, Jia-Zheng Wang, Xiao-Ru Shen, Chao Zhan, Rajkumar Devasenathipathy, Jian-Zhang Zhou, De-Yin Wu, Bing-Wei Mao, et al. Plasmonic hot electron-mediated hydrodehalogenation kinetics on nanostructured ag electrodes. *Journal of the American Chemical Society*, 142(41):17489–17498, 2020.

[206] Daniel R Semlow, Victoria A MacKrell, and Johannes C Walter. The hmces dna-protein cross-link functions as an intermediate in dna interstrand cross-link repair. *Nature Structural & Molecular Biology*, 29(5):451–462, 2022.